

© 2020

Yavuz Orhan Yaman

ALL RIGHTS RESERVED

**INTRA-CLUSTER CHANNEL MODELING AND
CROSS-LAYER BEAMFORMING EFFICIENCY FOR
MM-WAVE COMMUNICATIONS**

by

YAVUZ ORHAN YAMAN

A dissertation submitted to the

School of Graduate Studies

Rutgers, The State University of New Jersey

In partial fulfillment of the requirements

For the degree of

Doctor of Philosophy

Graduate Program in Electrical and Computer Engineering

Written under the direction of

Predrag Spasojevic

And approved by

New Brunswick, New Jersey

JANUARY, 2020

ABSTRACT OF THE DISSERTATION

Intra-Cluster Channel Modeling and Cross-Layer Beamforming Efficiency for Mm-Wave Communications

By YAVUZ ORHAN YAMAN

Dissertation Director:

Predrag Spasojevic

In millimeter-wave (mmWave) channels, to overcome the high path loss, beamforming is required. Since beamforming is technically a spatial filtering operation, the spatial representation of the channel is essential. Specifically, for accurate beam alignment and minimizing the outages, inter-beam interferences, etc., cluster-level spatial modeling is necessary. Further, to balance and optimize the hardware complexity at the receiver front-end and the received power, a detailed analysis for the beamforming efficiency at PHY layer is required. In the first part of this study, we first create a ray-tracing based intra-cluster channel model (RT-ICM) for stationary mmWave communications and then using RT-ICM, in the second part, we inquire the optimum beamwidth values that maximizes the received power in the case of both perfect and imperfect alignments. Using the theoretical array antenna gain models for uniform linear array (ULA) and uniform planar array (UPA), we estimate the required number of antennas for the optimum beamwidth; thereby analyzing the cost at the receiver structure and study the trade-off curves for the reasonable optimum hardware complexity. We also show how to realize an adaptive beamwidth structure by means of phase-only beam broadening approach and then implement it into an hybrid beamforming system. In the simulations, we first show that the proposed intra-cluster model, RT-ICM is in a perfect agreement with the full-scan software results and the measurements held in the literature. For the beamwidth analysis, we demonstrate that the optimum beamwidth is a function of standard deviation of the channel power spectrum and the amount of misalignment. For a perfect alignment, we also show that the optimum beamwidth is zero, but to reach

95% of the maximum power for an indoor mmWave cluster, a practical beamwidth of $7^\circ - 10^\circ$ is enough, which can be created with 18 – 20 antenna elements for ULA. It is concluded that the antenna gain dominates the received power in the UPA case and intra-cluster power angular spectrum of the channel becomes less critical. Finally, in the third part, we propose two fast beam searching protocols that work at MAC layer to complete the beamforming efficiency analysis at mmWave communications.

Acknowledgements

I would like to express my sincere gratitude to my advisor Prof. Predrag Spasojevic for his invaluable guidance and support throughout my Ph.D. education. I thank Prof. Sophocles Orfanidis for many helpful discussions and his contributions to my work. Finally, I would like to state my exclusive thanks to Dr. Jerome J. Kukor, Dean and Alex Bachmann, Senior Administrator and the administrator staff at the School of Graduate Studies and Urmi Otiv, the Director of Global-International Student and Scholar Services and her team, as well as Prof. Narayan Mandayam, Department Chair for their inexpressible help on regulatory and sincere, motivated approach that allowed me to continue and complete my doctoral program.

Dedication

To my family.

Table of Contents

Abstract	ii
Acknowledgements	iv
Dedication	v
List of Tables	xiii
List of Figures	xiv
1. Introduction	1
I Channel Modeling	6
2. Ray Tracing Intra-Cluster Channel Model (RT-ICM)	7
2.1. Overview of mmWave Spatial Channel Models	7
2.2. Cluster Definition of the Model	10
2.3. Basic Geometric Model (BGM)	11
2.3.1. Environment Setup	11
2.3.2. Calculating Path Lengths and Angles	11
2.3.3. Timing Parameters and Time-Angle Relation	12
2.3.4. Support Region	13
Reflection Geometry	14
Visible Region	15
2.3.5. Formulation Validation for Other Scenarios	17
2.4. Intra-Cluster Channel Model Setup using Basic Geometric Model	18
2.4.1. System Setup	18

2.4.2.	Directive Diffuse Scattering Model	19
2.4.3.	Power Calculation of the Rays	21
	Free Space Loss	21
	Reflection Loss	22
	Scattering Loss	22
2.4.4.	Phase Calculation of the Rays	23
	Phase Offset due to Path Distances	23
	Phase Offset due to Reflection	23
2.4.5.	Binned Intra-Cluster Channel Model	24
2.5.	Extension to MIMO	26
2.5.1.	Angular Channel Impulse Response	26
2.5.2.	LoS Ray Parameters	27
2.5.3.	MIMO Beamformed Channel Angle Response	27
2.6.	Conclusion	29
3.	Implementation and Validation of RT-ICM	30
3.1.	Incoherent and Coherent Power Calculations	30
3.2.	Full Scan EM Software	31
3.3.	Implementation	32
3.3.1.	Indoor 60 GHz - Classroom Environment [16]	33
	Receiver is at the Center	34
	Receiver is on the Corner	34
3.3.2.	RT-ICM Setup	35
3.3.3.	Wireless Insite® Setup	35
3.4.	Simulation Results	36
3.4.1.	Comparison with Measurement Results	37
	Receiver is at the Center	37
	Receiver is on the Corner	38
3.4.2.	Comparison with Wireless Insite®	39

Receiver is at the Center	39
Receiver is on the Corner	40
3.4.3. Comparison with IEEE 802.11ad/ay	41
3.5. Conclusion	43
4. Extension of RT-ICM - Blockage Support	46
4.1. Introduction	47
4.2. Background	49
4.2.1. Ray Tracing Intra-Cluster Model (RT-ICM)	49
4.2.2. Blockage Model	49
4.3. Blockage Model Support to RT-ICM	51
4.4. Case Study: An IEEE 802.11ad based Indoor Conference Room	55
4.4.1. Setup	55
4.4.2. Numerical Results	56
4.5. Conclusion and Discussion	57
 II Beamwidth Optimization	 60
5. Analytical Framework of Optimum Beamwidth Selection	61
5.1. System and Channel Model	62
5.2. Antenna Structure and Gain	64
5.2.1. Beam Pattern Model	65
5.2.2. Antenna Gain vs. Beamwidth	66
5.3. Angular Distribution of Total Power and Extracted Power	66
5.3.1. Extracted Power for IEEE 802.11ad Cluster Model	67
5.3.2. Extracted Power for RT-ICM	67
Gaussian Approximation	68
5.4. Problem Formulation	68
5.4.1. IEEE 802.11ad	68
Maximization of P_R	69

5.4.2.	RT-ICM	72
5.4.3.	Asymptotic Analysis of Perfect Alignment	72
	Maximum Received Power	73
	Optimum Practical Beamwidth	73
5.4.4.	Triangular Beam Model	76
5.5.	Performance Evaluation	77
5.6.	Summary	82
6.	Optimum Beamwidth Analysis for Uniform Planar Arrays (UPAs)	85
6.1.	System and Channel Model	85
6.2.	Antenna Structure and Gain	85
6.2.1.	Beam Pattern Model	86
6.2.2.	Directivity of RUPA	87
6.2.3.	Selection of Angular Parameters	88
	Constraint 1	88
	Constraint 2	89
	Constraint 3	89
6.3.	Problem Formulation	90
6.3.1.	Extracted Power from Channel	90
6.3.2.	Received Power Problem Formulation	91
	Maximum Received Power	91
	Optimum Practical Beamwidth	92
6.4.	Performance Evaluation	92
7.	Varying the Beamwidth of Hybrid Beamforming	97
7.1.	Motivation	98
7.2.	Challenges for Beamwidth Flexibility	99
7.3.	Beam Broadening	101
7.3.1.	Signal Model	101
7.3.2.	Beam Broadening at Broadside	102

7.3.3. Steering the Broadened Beam	104
7.4. Beamwidth and Power Loss Analysis	106
7.4.1. Beamwidth	106
7.4.2. Power Loss	107
7.4.3. Broadening Bounds	107
7.5. Implementation to Hybrid BF Systems	108
7.5.1. Challenge with Channel Estimation	109
7.5.2. Updated Algorithm	109
7.6. Simulation Results	110
7.7. Conclusion	113

III Efficient Beamforming Algorithms 115

8. Binary Search and Linear Search	116
8.1. Motivation	116
8.2. Current Beamforming Protocols	117
8.2.1. Beamforming in the IEEE 802.11ad	117
8.2.2. Beamforming in the IEEE 802.15.3c	118
8.3. Proposed Algorithms	119
8.3.1. Binary Searching	120
8.3.2. Linear Searching	123
8.3.3. Step Analysis	125
IEEE 802.11ad	125
IEEE 802.15.3c	126
8.4. Simulation Results	127
8.4.1. Beamforming Setup Time	128
8.4.2. BER Performance	128
8.4.3. Power Saving Performance	129

9. Enhanced Binary Search for NLOS Environments	132
9.1. Motivation	132
9.2. System Model	133
9.2.1. Single-Side Approach	135
9.2.2. Energy Density Map of Antenna Beams	136
9.3. Proposed Enhanced-BSB	137
9.3.1. BSB Algorithm	137
9.3.2. Proposed Method EBSB	139
9.4. Step Analysis	141
9.5. Simulation Results	142
9.5.1. Success Probability	142
9.5.2. Beamforming Setup Time	145
9.5.3. Power Loss Analysis	146
9.6. Conclusion	147
10. Conclusion	148
Appendix A. Derivations for RT-ICM	149
A.1. BGM Parameters	149
A.1.1. Derivation of ϕ_s and l_{dif}	149
A.1.2. Derivation of Support Region Limitations	149
Geometry Limitation	149
Transmitter Beamwidth Limitation	149
A.1.3. Formulation Validation of BGM	150
Path Length Calculation Check	150
Reflector Length Calculation Check	150
Transmit Beamwidth Calculation Check	150
A.2. Validation of the Directive Model for All Cases	150
Appendix B. Derivations for Beamwidth Analysis	152

B.1. Maximization of P_R in case of Misalignment	152
B.1.1. First Derivative	152
B.1.2. Second Derivative	152
B.2. Maximization of P_R for Perfect Alignment	153
B.2.1. Maximum Received Power Derivation	153
B.2.2. Optimum Beamwidth Approximation	153
References	154

List of Tables

2.1. Geometrical Notations	12
2.2. Resultant Support Range for α	16
3.1. Input Parameters of the Model (d , h_t , h_r , l_{neg} , l_{pos} [meters], σ_h [mm]) P_T [dBm], G_T , G_R [dB], P: polarization, V:vertical, H: horizontal) . . .	36
4.1. Input Parameters of the Simulation (d , h_t , h_r [meters], σ_h [mm]) P_T [dBm], G_T , G_R [dB], P: polarization, V:vertical, H: horizontal)	56
5.1. Asymptotic Analysis of P_{max} and Performance Comparison of 802.11ad and RT-ICM	75
6.1. Some candidate selections of the parameters	89
7.1. Simulation Parameters	110
8.1. Step Analyses of BF Algorithms	126
8.2. Simulation Parameters	128
9.1. Step Analyses of BF Algorithms	143
9.2. Simulation Parameters	143

List of Figures

2.1. Cluster definition of the model	10
2.2. Basic geometrical model of the cluster	13
2.3. Relation between offset AoA and diffuse ray delay	14
2.4. Diagram of offset AoA limitations	15
2.5. Transmitter beamwidth limitation	16
2.6. Diagrams for the cases diffuse ray reflects from out of the normals frame for positive (with α_p) and negative (with α_n) reflections	17
2.7. Updated cluster model diagram with the addition of diffuse scattering pattern	20
2.8. Example illustration of the binning procedure.	25
2.9. Flowchart diagram of the C-CIR generation.	26
2.10. Illustration of the non-overlapping first-order clusters in a MIMO com- munication scenario within a typical living room environment	28
3.1. Measurement environment and the distance parameters when receiver is in the room center.	33
3.2. Measurement environment and the distance parameters when receiver in the room corner.	34
3.3. Environment and measurement scenario created in Wireless Insite. . . .	35
3.4. Theoretical Power Angle Profile of the channel when receiver is in the center of the room.	37
3.5. Binned Power Angle Profile of the channel when receiver is in the center of the room.	38
3.6. Theoretical Power Angle Profile of the channel when receiver is in the corner of the room.	39

3.7. Binned Power Angle Profile of the channel when receiver is in the corner of the room.	40
3.8. Visual representation of the channel paths that exceed -70 dB power threshold when receiver is at the center.	41
3.9. Channel AoA comparison of the software and RT-ICM when receiver is at the center.	42
3.10. Power Comparison when receiver is at the center.	43
3.11. Channel AoA comparison of the software and RT-ICM when receiver is at the corner.	44
3.12. Power Comparison when receiver is at the corner.	44
3.13. PAP comparison with IEEE 802.11ad/ay for the blackboard reflection when the receiver is at the center	45
4.1. Azimuth plane geometry of the assumed scenario used to model the attenuation due to blockages.	50
4.2. Comparison of the theoretical and simulated attenuation for various geometry sizes with $\zeta = -20$ dB.	52
4.3. Schematic contrasting the effect an environmental object at two different locations. The location (and the subsequent impact) of the object divides the space under consideration into two regions. The region where reflection (along with blockage) to the receiver occurs is termed as Region A whereas the one where only blockage occurs is termed as Region B.	53
4.4. Blockage model update of BGM given in RT-ICM when the object is in region A.	54
4.5. An IEEE 802.11ad based indoor office scenario with a transmitter and receiver pair. The CC boundaries are shown to indicate how the attenuation due to blockage is calculated (Section 4.2.2).	55

4.6. Received power contribution by means of reflection due to the blocking object as a function of the location of the object with respect to the reflector surface.	57
4.7. The PAP as a result of attenuation and reflection contribution due to the blocking object.	58
4.8. Total received power as a function of the location of the object (distance d_h) with respect to the reflector surface i.e. wall 1 in Fig. 4.5.	59
5.1. Visualization of the optimum beamwidth problem at the receiver	62
5.2. Antenna pattern models considered in the chapter.	65
5.3. Received power in case of misalignment for $\sigma = 5$ and $P_{tot} = 1.2\mu W$. . .	70
5.4. Optimum beamwidth in case of misalignment.	71
5.5. Accuracy of second derivative test method in case of misalignment and $\delta - \sigma$ relation effect on $\Delta\phi_{opt}$	77
5.6. Variation on the maximum achievable received power with respect to δ for different σ and ϕ_0	78
5.7. Practical beamwidth analysis performance of RT-ICM for $v = 9.23$ (or $\sigma = 6.52$).	79
5.8. Beamwidth Error in IEEE 802.11ad model due to fixed $\sigma = 5^\circ$ in the perfect alignment case.	80
5.9. Models performance comparison in terms of required antenna elements for perfect alignment	81
5.10. Beamwidth Error in IEEE 802.11ad model due to fixed $\sigma = 5^\circ$ in the perfect alignment case.	82
5.11. Models performance comparison in terms of required antenna elements for perfect alignment	84
6.1. Visualization of the optimum beamwidth problem at the receiver	86
6.2. $(N \times M)$ -element rectangular UPA diagram with the scan angles and beamwidths illustration.	87
6.3. Directivities of the selected parameter sets and the effect of the constraints.	90

6.4. Percentage of received power versus beamwidth when $\sigma = 5$	93
6.5. Total received power versus beamwidth.	94
6.6. Total received power versus number of elements.	95
6.7. ULA and UPA comparison for the same case study.	96
7.1. Symmetric array design for the simplified model.	101
7.2. Resultant subarray and total radiation pattern for $N=128$, $M=8$	103
7.3. Split effect of keeping the weights flipped on steering for $N=128$, $M=8$	104
7.4. Broadened and steered beam (to $\phi_0 = 80^\circ$) for $N=128$, $M=8$	106
7.5. Narrowest and broadened beams for $N=128$, $M=2, 4, 8$ at $\phi_0 = 92^\circ$	111
7.6. Estimated optimum and broadened beam for $N=256$, $M=8$ at $\phi_0 = 47^\circ$	112
7.7. Spectral efficiency comparison while drift occurs after channel estimation.	113
8.1. An example of BSB algorithm for $N=16$	122
8.2. A worst case example of LSB algorithm for $N=16$	123
8.3. A best case example of LSB algorithm for $N=16$	124
8.4. BF setup time performances of proposed methods	129
8.5. Error performances of proposed methods for $N=\{12, 36, 60\}$	130
8.6. Power consumption of BF algorithms during transmit sector training	131
9.1. Received power for each pair for $N = 120$	135
9.2. Energy density map of STA1 transmit sectors in LOS case for (a) $N = 61$, (b) $N = 127$	137
9.3. Energy density map of STA1 transmit sectors in NLOS case for (a) $N =$ 61, (b) $N = 127$	138
9.4. An example of EBSB algorithm for $N_1 = 24$	142
9.5. Success probability of the methods in LOS situations.	144
9.6. Success probability of the methods in NLOS situations.	145
9.7. BF setup performance of methods.	146
9.8. Power loss analysis due to the misalignment of the beams.	147

Chapter 1

Introduction

Millimeter-wave (mm-Wave) communication is continuing to emerge with several advantages over the current wireless bands such as higher throughput, lower latency, reduced interference, and increasing network coordination ability. Many indoor and outdoor measurements aim at modeling the mmWave channel characteristics [1,16–18,21,33–36]. Beamforming is typically introduced to compensate for the higher path loss at higher mmWave frequencies [2,4]. However, spatial filtering of the channel requires detailed knowledge of the angle spectrum of the channel. Fortunately, clusters are spatially well-separated in mmWave channels, which allows creating a beam for each cluster [11]. Furthermore, as the first order reflections and the direct path cover as high as 99.5% of the received power [24], received clusters in mmWave can usually be considered for the first-order reflections only. On the other hand, well-known channel propagation mechanisms affect mmWave channels differently. For example, while diffraction contributes to the received power for microwave channels, its contribution is negligible in mmWave channels [34]. Also, scattering is limited in lower frequencies, whereas, in mmWave channels, even a typical wall can scatter the incoming signal significantly due to the tiny variations on its surface. Hence, a mmWave channel model should take the diffuse scattering into account in order to properly replicate the channel characteristics [9,18,42]. Measurement results show that in some NLOS cases wider beamwidth antennas result in higher received SNR [35,38] which leads to the fact that array design that would create optimum beamwidth is directly related to the spatial representation of the received cluster. Then, although the clusters can be easily identified, an accurate intra-cluster angular model has vital importance. Hence, knowledge of the detailed cluster angular spectrum is essential for at least two important applications including

accurate beam alignment along with an optimum beamwidth and to minimization of inter-beam interference.

Measurements confirm that the mmWave channels are site-specific [19,34] and that the channel characteristics depend highly on the environment [22]. Hence, creating generic statistical models for typical environments as in the case of microwave bands is difficult [6]. For this reason, researchers tend to propose statistical channel models for specific environments [19–21, 24, 34].

To give generalized models, a hybrid geometry-based stochastic channel model (GSCM) [15] that combines stochastic and deterministic approaches was recently introduced [21, 36] and adopted by the mmWave wireless standards such as 3GPP [6], IEEE 802.11ad [10], IEEE 802.11ay [11], MiWEBA [7] and COST2100 [8]. Although the hybrid method is more accurate than the statistical approach, while generating faster and more generalized results than the deterministic approach, nevertheless it does not provide sufficient intra-cluster angular modeling accuracy necessary for beamforming and inter-cluster interference optimizations. Specifically, in 3GPP Channel Model [6, 36], the intra-cluster angular modeling is solely based on measurements and the number of paths within the cluster and their powers are fixed for certain type of environments. On the other hand, 60 GHz indoor standards 802.11ad [10], 802.11ay [11] and 802.15.3c [12] adopt statistical intra-cluster model rooted from the S-V model [13, 14] and angular behavior of the rays within the cluster are simply modeled as a random variable. While Quasi-Deterministic (Q-D) Channel Model [23, 37] takes mmWave scattering into account, its effect on the spatial domain in the cluster level is not addressed. As a result, to the authors' knowledge, a detailed intra-cluster mmWave channel model that studies the power distribution in angle domain has not been introduced yet.

On the other hand, significant contribution is published for the receiver processing aspect of beamforming, including optimum transmitter and receiver design [4] with array antennas and beamforming protocols [2]. However, maximizing the beamforming efficiency can be challenging due to the misalignments, weak tracking ability, blockages, outage loss, etc. which requires channel knowledge in the angular domain. Specifically, beams with non-optimized beamwidths may increase inter-beam interference and

wasted energy, i.e. outage rate, or even cause a link failure easily when combined with beam misalignment. As a result, while the requirement of the accuracy on the beam alignment to the cluster angle of arrival (AoA) is unquestionable, selecting an appropriate beamwidth is also essential in the mmWave system networks.

Several measurements are already conducted in mmWave communications and prove that beamwidth has a critical effect on the channel parameters. In [52–54], antenna directivity (indirectly beamwidth) dependency to the delay and angle spread of the link is investigated at 28, 38 and 60 GHz. [35, 59] conduct some outdoor experiments at 28 and 38 GHz with different beamwidth antennas and measure the incurred path loss. [38] provides similar outdoor LOS and NLOS tests and collect data of captured energy (received power) for several beamwidth values at 28 and 40 GHz. Both experiments show that wider beams have better performance, i.e. capture more energy and experience less path loss. In [60], optimum beamwidth is measured in case of blockage occurs within the channel where wider beamwidths are provided based on beam expansion. While the nonnegligible effect of the beamwidth on mmWave communications is demonstrated with several other measurement results, on the other hand, very few beamwidth analyses on the performance metrics are proposed so far. In [58], it is shown that there is an optimal non-zero beamwidth (around 5°) that maximizes the coherence time of the time-varying vehicular channel at 60 GHz. In [57], analysis results show that 10° beamwidth has better coverage, less interference compared to 30° for mmWave cellular networks. A more related work [56] studies AoA estimation error effects on bit-error-rate (BER) with different beamwidths for the clustered channel model. Finally, a detailed analysis of the link between the channel angular dispersion and the antenna structure is given in [55]. However, the channel is simply assumed to be Rician and no clustering approach is adopted as generally seen in mmWave channels. To the best of authors' knowledge, a detailed theoretical analysis of the beamwidth and received power relation in the case of misalignment for clustered mmWave channels is not studied.

In the first part of the dissertation, we propose a spatial ray-tracing mmWave intra-cluster channel model (RT-ICM) that takes only first-order reflections into account. In our model, we also add the scattering effect based on the material properties. The

model outputs the power distribution both in angle and time domain within the cluster and can be used for both indoor and outdoor mmWave systems in any type of environments given the conditions that the required physical parameters for ray-tracing are provided. We further provide a MIMO channel model that consists of nonoverlapping clusters and discuss that pencil-shape beamwidth provided by massive MIMO allow an increased number of single-order clusters in mmWave. Furthermore, we give the insights that, with the combination of massive MIMO and the proposed channel model, maximum spatial usage of the channel can be achieved using several beams with different beamwidths directed to detected clusters. The advantage of the proposed model is that it provides the accuracy of the deterministic approach and the simplicity of the stochastic approach while comes with an intra-cluster model addition to the hybrid approaches. We also show that the results of the proposed model match well with the published indoor mmWave measurements.

In the second part, we provide an analytical framework for the optimum beamwidth that maximizes the received power for indoor mmWave clusters, in the case of misalignment. We first give the relation between beamwidth and the captured power from the cluster. To do so, we use two different intra-cluster channel models, IEEE 802.11ad [10] and our work, RT-ICM. Then, we combine it with the antenna gain at an arbitrary cluster AoA and provide an overall received power and beamwidth relation. In the analysis, we consider the uniform linear array (ULA) antenna type for the antenna gain, and two beam models to approximate the main lobe array pattern; rectangular and triangular. We show that when the misalignment error is smaller than the standard deviation of the cluster power spectrum, the optimum beamwidth is at zero, while the theoretical maximum received power approaches to a constant. For this case, we give practical limits of the optimum beamwidth with the relation to the number of elements such that sacrificing from the maximum received power in the order of tenths can reduce the required number of antenna elements significantly. However, when the alignment error is larger than the standard deviation, we show that the optimum beamwidth increases rapidly to a level larger than the alignment error. Finally, we evaluate the performance of the analysis by comparing the analytical results with simulations for

an indoor mmWave cluster. We also add the similar analysis with UPA and compare to the one with ULA. The work we propose in this dissertation will give insights to the optimum antenna array design in both MIMO and massive MIMO applications for future mmWave systems network.

In the last part of the dissertation, we propose two types of fast beam searching algorithms that can be used in the replacement of the current mmWave WLAN and WPAN standards such as 802.11ad and 802.15.3c; thereby increasing the MAC performance of the beamforming. The searching mechanisms are basically the adaptations of two fundamental fast searching algorithms used in data structures, binary search and linear search. Relying on the fact that 60 GHz communication is efficient mostly for LOS environments [10] and assuming the first and second order reflections from walls reach receiver always with less SNR than of the LOS ray, proposed methods suggest ignoring the "far" sectors directly without sending a frame by applying searching algorithms. Suggested searching methods can be directly applied as Sector Sweep Level (SLS) phase in IEEE 802.11ad and as sector-level training phase (as well as beam-level training phase) in IEEE 802.15.3c. Proposed algorithms reduce the steps in training and, hence, the beamforming setup time. In addition, they save power by reducing the number of frames to be sent. For binary search beamforming (BSB), the advantages are gained at the expense of an increase in the error probability due to false sector pairing, in certain cases.

Part I

Channel Modeling

Chapter 2

Ray Tracing Intra-Cluster Channel Model (RT-ICM)

2.1 Overview of mmWave Spatial Channel Models

Several spatial channel models are proposed and they can be categorized into 3 types based on the approach [5, 9]: Statistical, deterministic and hybrid. In statistical channel modeling (SCM), statistics of the channel parameters are aimed to be obtained [13, 14, 19, 20, 33]. Time, amplitude and phase of a multipath component are the main parameters of a propagation channel and are reproduced in a clustered SCM statistically in the early years for conventional microwave wireless communication systems. SCMs that also model the angular parameters of the channel is called statistical spatial channel model (SSCM) [14, 21]. In [14], angle statistics of the multipath components are obtained through the measurements and both inter- and intra-cluster angle of arrivals are modeled independent of time statistics. SSCMs are generic models that sacrifices accuracy to gain from the computational efficiency.

In deterministic approach, however, propagation mechanism is tracked geometrically based on the physics of the electromagnetic wave propagation and the channel parameters are calculated at the receiver end [5, 9]. Ray tracing [30–32] and electromagnetic wave theory simulations such as finite-difference-time-domain (FDTD) are the main deterministic channel modeling procedures. Ray tracing treats the multipath components as rays that travel according to the optics physics whereas the EM-wave theory approach uses Maxwell equations to initiate the propagation and updates the equations along the way to model how the wave propagates within the channel. Since both methods are inherently geometrical models, parameters can be calculated without the need of any type of measurements as in the case of SSCM. Temporal parameters, on the other hand, are computed based on the distances that the wave travels over

the channel. However, when ray tracing is employed, measurement limitations should be taken into account as well when determining the number of multipath components and their amplitudes and phases too. Depending on the knowledge of the environment, both approaches result in a quite accurate modeling as the channel is tracked according to the underlying physics of the propagation. In fact, deterministic approaches need to have the exact information of the real environment to accurately model the channel. However, even with the exact information, tracing the high number of rays over the propagation channel is computationally expensive. Fortunately, with the sparsity of the mmWave channel, tracing up to second order reflection characterizes the parameters of the channel almost perfectly [10, 33].

Because of the high complexity of the channel, deterministic approaches fail to estimate the intra-cluster parameters. On the other hand, in SSCMs, inaccuracy is the trade-off. Considering the site-specific limitation of the mmWave systems, determination of the cluster locations both in time and angular domain is critical. Especially a small error in angular parameters yields a misalignment in antennas beamforming that may even cause a link failure.

The method of the combination of stochastic and deterministic approaches in mmWave became popular recently and called geometry-based stochastic channel model (GSCM). In [15], double-directional model is proposed as a GSCM where antenna effects to the directionality can be extracted from (and re-embedded to) the propagation channel angle characteristics. GSCM is already adopted by the wireless standards such as 3GPP [6], IEEE 802.11ad [10], IEEE 802.11ay [11], MiWEBA [7] and COST2100 [8]. In that hybrid approach, weak sides of the models are filled with the other approach. For example, using ray tracing, cluster positions (both in time and angle domain) are determined exactly whereas the intra-cluster parameters are defined stochastically [9].

Although the hybrid method outputs more accurate and site-specific results than the stochastic approach and faster and more generalized results than the deterministic approach, yet the intra-cluster modeling problem is still not addressed. Especially, a realistic angular model of a cluster is vital for designing and developing beamforming algorithms accurately in mmWave systems. In 3GPP Channel Model [6, 36], the

intra-cluster time parameters are modeled statistically based on the combination of ray tracing and measurement. But, angular parameters modeling is solely based on measurements and the number of paths within the cluster as well as their powers are fixed for certain type of environments which may easily be far away from the practical cases. On the other hand, 60GHz indoor standards 802.11ad [10], 802.11ay [11] and 802.15.3c [12] adopt statistical intra-cluster model where the multipath components arrivals are approximated as Poisson process, rooted from the S-V model [13]. Angular behavior of the rays within the cluster are simply modeled as Gaussian in [10, 11] and Laplacian in [12].

In mmWave channels, the LOS component and the low-order reflections determine mostly the whole communication channel [10, 33]. Hence, a ray tracing algorithm that consists only of low-order reflections would reveal most of the cluster-level information both in the temporal and in the spatial domain [18]. Then, instead of creating an end-to-end ray tracing channel model that covers several complex propagation mechanisms, generating a ray tracing algorithm for only first-order reflections in the environment would reflect most of the channel properties.

As a result, a ray tracing algorithm that considers only first-order reflections would be both easy to implement and computationally inexpensive while revealing most of the cluster-level information both in the temporal and in the spatial domain [18]. The beauty of the proposed model is that it provides the accuracy of the deterministic approach and the simplicity of the stochastic approach while adding the intra-cluster feature to the hybrid model.

Recalling that considering only the reflection phenomenon yields failing to characterize intra-cluster channel further. Thus, we need to add scattering and diffraction effects of the first-order reflectors on top of first-order reflections. Fortunately, measurement results show that mmWave channels can be assumed unaffected by diffraction [34], thus we can eliminate the diffraction and focus only on reflection and scattering for the first-order reflections.

In this part of the dissertation, we propose a geometrical first-order reflection model using a ray tracing algorithm that outputs time and angular parameters, by also taking

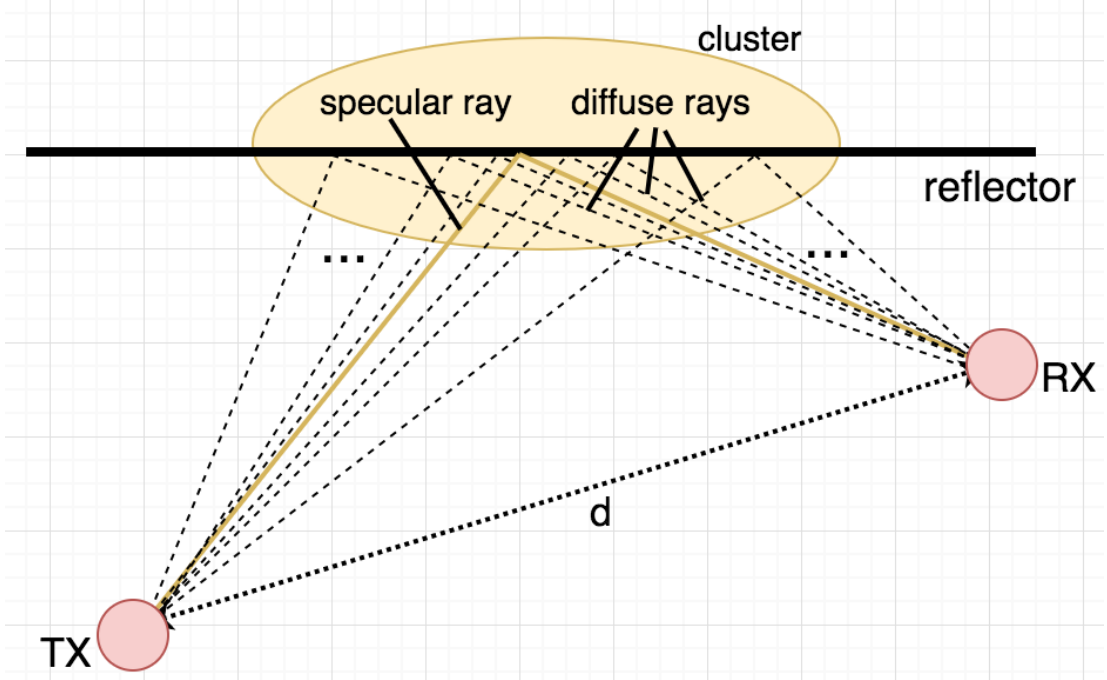


Figure 2.1: Cluster definition of the model

the scattering effects into account that a conventional ray tracing doesn't consider. As the next section suggests, each first order reflection in a mmwave channel can be considered as a cluster thanks to the sparse feature of the mmWave channels.

2.2 Cluster Definition of the Model

Let two communicating stationary devices be positioned at a distance d from each other, as seen from the top view in Fig. 2.1. A rough surface acts as a reflector that creates the cluster which includes several rays that are generated by diffuse scattering. Note that, only one ray obeys the Snell's Law [30] in the cluster model and it is called as the *specular ray*, referring to the specular reflection. The others are going to be called as *diffuse rays*, referring to the diffuse reflections. Both ray types are shown in Fig. 2.1. Only the 2-D azimuthal plane is considered in the model.

In our model, for non line-of-sight (NLOS) scenarios, we restrict the clusters to be generated via first-order reflections only. We also let each reflector create only one cluster. In other words, the number of clusters equals the number of first-order reflectors in the environment. Also, when we discuss multi-cluster scenarios, we assume

the clusters do not overlap spatially.

We represent the transmitter (TX) and receiver (RX) with circles in Fig. 2.1 but the proposed model assumes them as point sources. Hence, each ray leaves the transmitter, reflects from a unique point at the reflector, and further reaches the receiver with a unique angle of arrival (AoA).

2.3 Basic Geometric Model (BGM)

In order to output the spatial behavior of the channel, geometrical parameters of the communication environment have to be specified. In this subsection, a geometric simple model of the environment is provided. Unless otherwise stated, all distances are in meters and angles are in degrees. We illustrate angles in diagrams with clockwise arrows if they are positive, counterclockwise otherwise.

2.3.1 Environment Setup

Considering the specular ray and one diffuse ray, all main parameters can be defined as seen in Fig. 2.2. As seen, the shortest ray within the cluster is the specular ray. This can be proved by simply mirroring either the receiver or the transmitter with respect to the wall.

The distances given in the diagram are defined in Table 2.1. Hence, the length of the specular ray is $l_{sp} = d_1 + d_2$. Similarly, the length of the diffuse ray is

$$l_{dif} = l_1 + l_2 \quad (2.1)$$

The formulation will be setup according to Fig. 2.2 and then the validation of the formulas for other scenarios will be checked in Section 2.3.5. Geometrical derivations are given in Appendix A.1.

2.3.2 Calculating Path Lengths and Angles

With the given distances d , h_t and h_r , specular ray length is $l_{sp} = \sqrt{s^2 + (h_t + h_r)^2}$ where $s = \sqrt{d^2 - |h_t - h_r|^2}$. The specular ray AoA with respect to reflector normal at

Table 2.1: Geometrical Notations

Notation	Definition
d	length between the transmitter and receiver
h_t	length between the transmitter and the reflector
h_r	length between the receiver and the reflector
s	length between the reflector normal at transmitter (RNT) and the reflector normal at receiver (RNR)
d_1	length between specular ray reflection point and the receiver
d_2	length between specular ray reflection point and the transmitter
l_1	length between diffuse ray reflection point and the receiver
l_2	length between diffuse ray reflection point and the transmitter
s_1	length between specular ray reflection point and the RNT
s_2	length between specular ray reflection point and the RNR
s'_1	length between diffuse ray reflection point and the RNT
s'_2	length between diffuse ray reflection point and the RNR
ϕ_s	specular ray angle of arrival (AoA) with respect to the RNR
Ω_s	specular ray AoA with respect to the line-of-sight (LoS) line
α	offset AoA between specular and diffuse ray
σ	tilt angle of the reflector with respect to LoS line
l_{neg}	reflector length that covers diffuse rays with negative α
l_{pos}	reflector length that covers diffuse rays with positive α
s_{pos}	length between the receiver-side reflector endpoint and the RNR
α^+	positive offset AoA support limit
α^-	negative offset AoA support limit
Θ	beamwidth of the transmitter beam
l_t	length of the transmitter side beam cover at reflector
l_r	length of the receiver side beam cover at reflector
s_t	length between the transmitter side beam edge and the RNT

receiver (RNR) is $\phi_s = \cos^{-1}((h_t + h_r)/l_s)$. Then, the diffuse ray length for a given α is

$$l_{dif} = \frac{h_r}{\cos(\phi_s - \alpha)} + \sqrt{h_t^2 + \left(s - \frac{h_r}{\cos(\phi_s - \alpha)} \sin(\phi_s - \alpha)\right)^2} \quad (2.2)$$

Finally, the specular ray AoA with respect to LoS ray is $\Omega_s = 90 - \phi_s + \sigma$ where, $\sigma = \sin^{-1}((h_t - h_r)/d)$ is the tilt angle as seen from Fig. 2.2.

2.3.3 Timing Parameters and Time-Angle Relation

The time of arrival (ToA) of the line-of-sight (LOS) ray is, $t_{los} = d/c$ where, c is the speed of light. Similarly, $t_s = l_s/c$ and $t_{dif} = l_{dif}/c$ are the ToA of the specular and diffuse ray, respectively. Finally, $\tau = t_{dif} - t_s$ is the diffuse ray *delay* with respect to

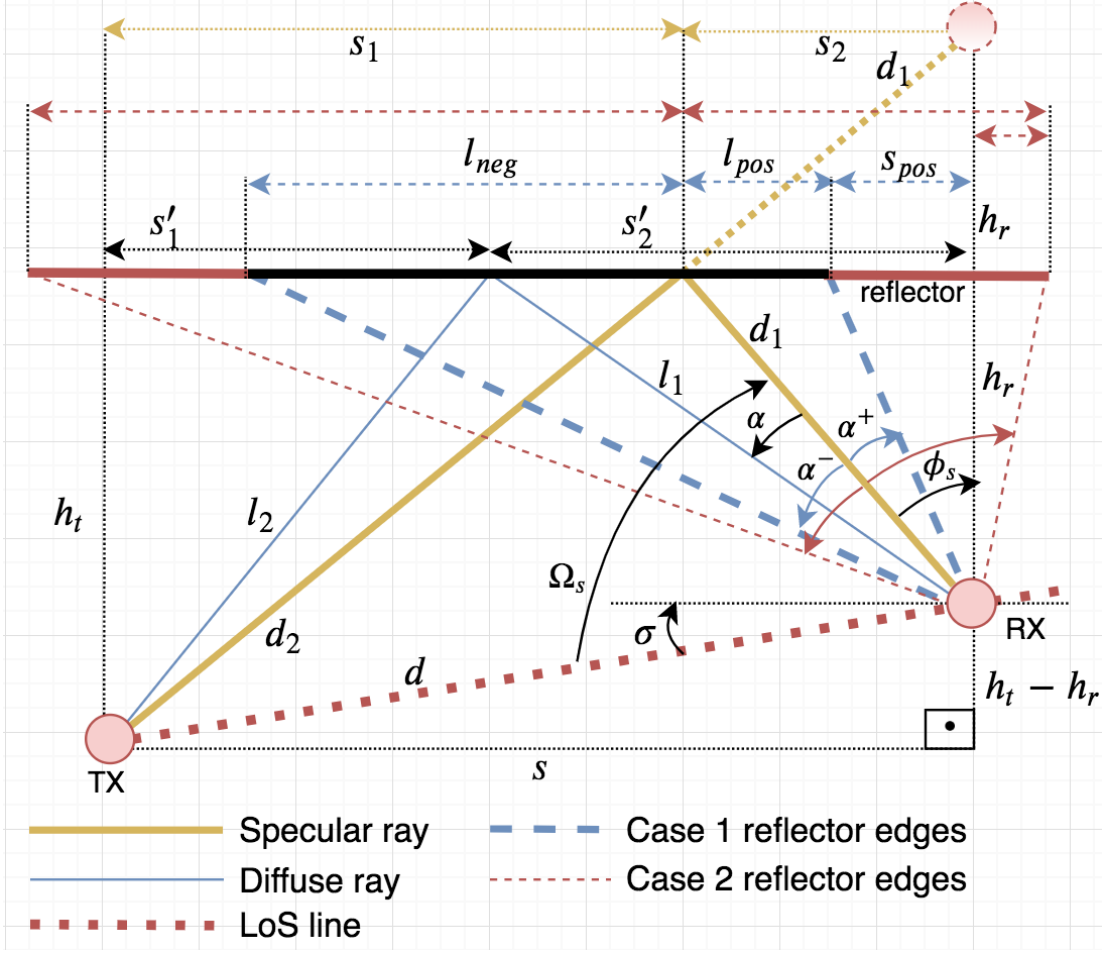


Figure 2.2: Basic geometrical model of the cluster

the specular ray.

Fig. 2.3 displays the τ - α relation for different values of h_t and h_r while d is fixed to 35 m. The range for α is selected as $[-10^\circ, 10^\circ]$ which is a typical angle spread of a cluster. As seen, for any $\{h_t, h_r\}$ pair, the relation is not symmetric. That means delays are not necessarily equal for two equal opposite signed offset AoAs. Another important result is that, the delay-angle relation highly depends on the environment. Even a very small change in distances yields much different delays for $\alpha < 0$.

2.3.4 Support Region

Several effects exist in practical scenarios that bound the angle spread of the receiver. We account those constraints on α and call the resultant available range as the *support*

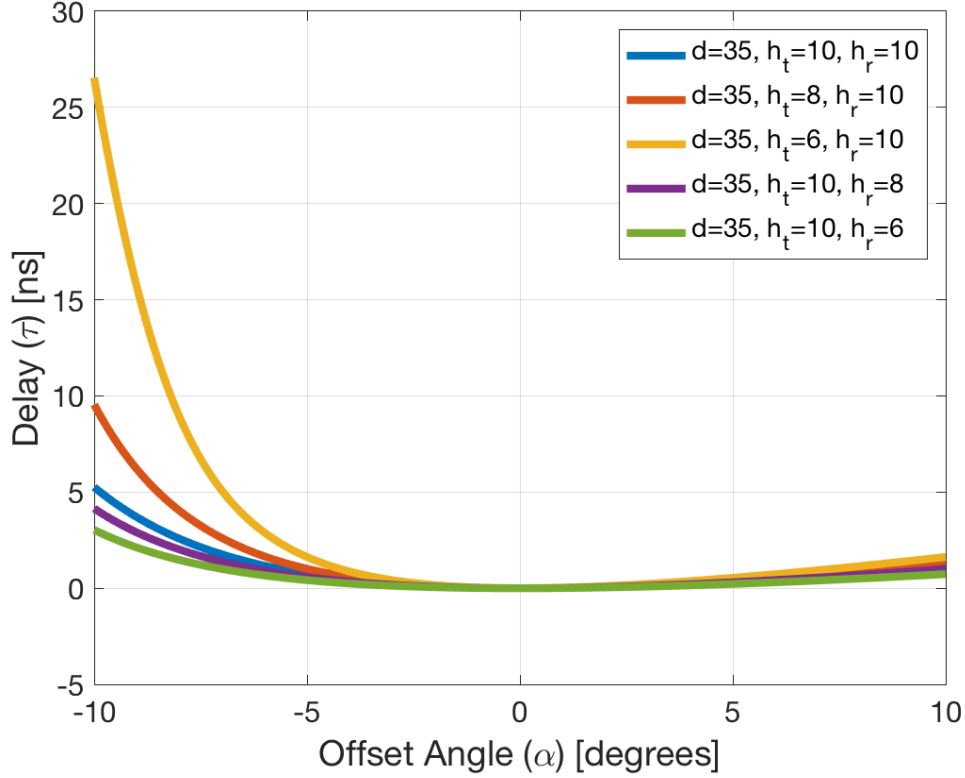


Figure 2.3: Relation between offset AoA and diffuse ray delay

region. We also define a region on the reflector surface that covers all the reflection points, called *visible region*. The visual meaning of these terms are shown in Fig. 2.4. Support region is limited primarily by the reflection geometry, secondarily by the visible region. Visible region is determined by the reflector length and the transmitter beamwidth. We give the ranges in the next subsections for each while the details are provided in Appendix A.1.2.

Reflection Geometry

h_t and h_r change the geometry drastically as seen from Fig. 2.3. Hence, two cases, $h_t > h_r$ and $h_t < h_r$, should be checked separately.

For case $h_t > h_r$, as seen from Fig. 2.2, a positive tilt angle σ is introduced that needs to be taken into account and calculated as $\sigma = \sin^{-1}((h_t - h_r)/d)$.

For case $h_t < h_r$, as seen from Fig. 2.2, accounting the leftmost and rightmost

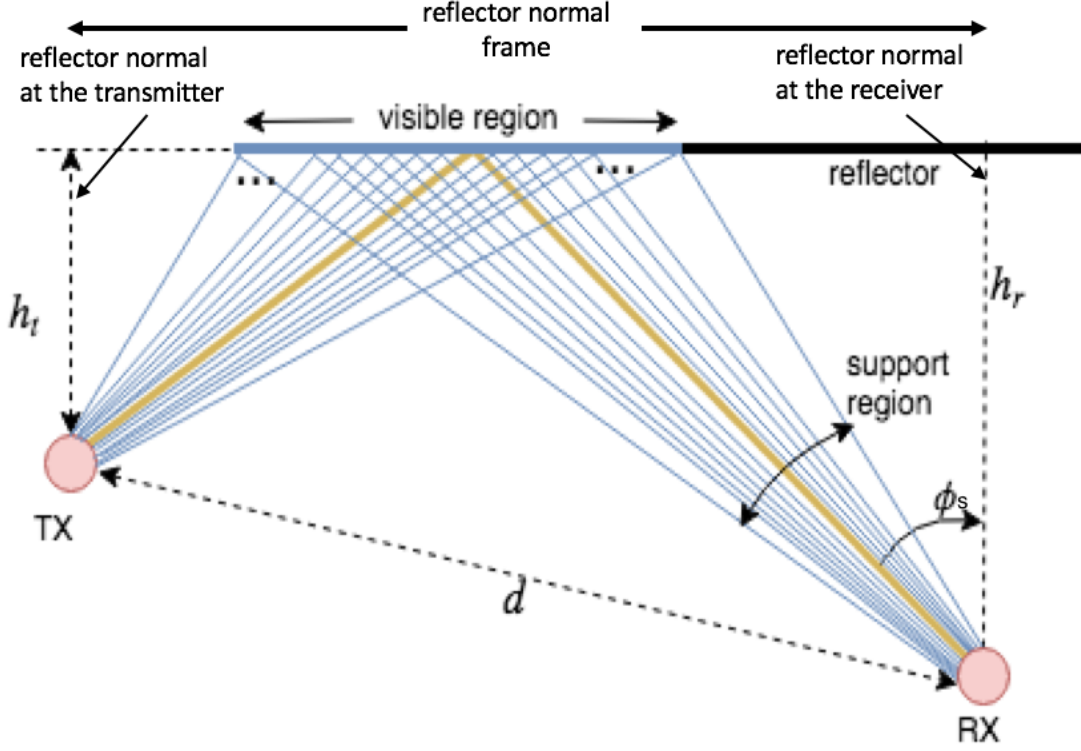


Figure 2.4: Diagram of offset AoA limitations

possible reflections, $\phi_s - \sigma + 90^\circ > \alpha > \phi_s - 90^\circ$. Similarly, for $h_t < h_r$, the range is given as $\phi_s + 90^\circ > \alpha > \phi_s - \sigma - 90^\circ$ as $\sigma < 0$ now and bounds the negative α .

Visible Region

Reflector length is an environmental parameter that affects the visible region geometrically, whereas the transmit beamwidth is a system parameter limitation. Reflector length limitation is illustrated in Fig. 2.2 for two cases. Ignoring the misalignment problems and sidelobes in the radiation pattern, we consider the transmit beam shape as a square wave that is steered towards the specular ray. The diagram in Fig. 2.5 visualizes the approach for two cases. Related parameters are listed in Table 2.1. Hence, minimum of two limitations at both sides will determine the *visible region*. Analytically,

$$\begin{aligned}
 w_t &= \min(l_t, l_{neg}) \\
 w_r &= \min(l_r, l_{pos})
 \end{aligned} \tag{2.3}$$

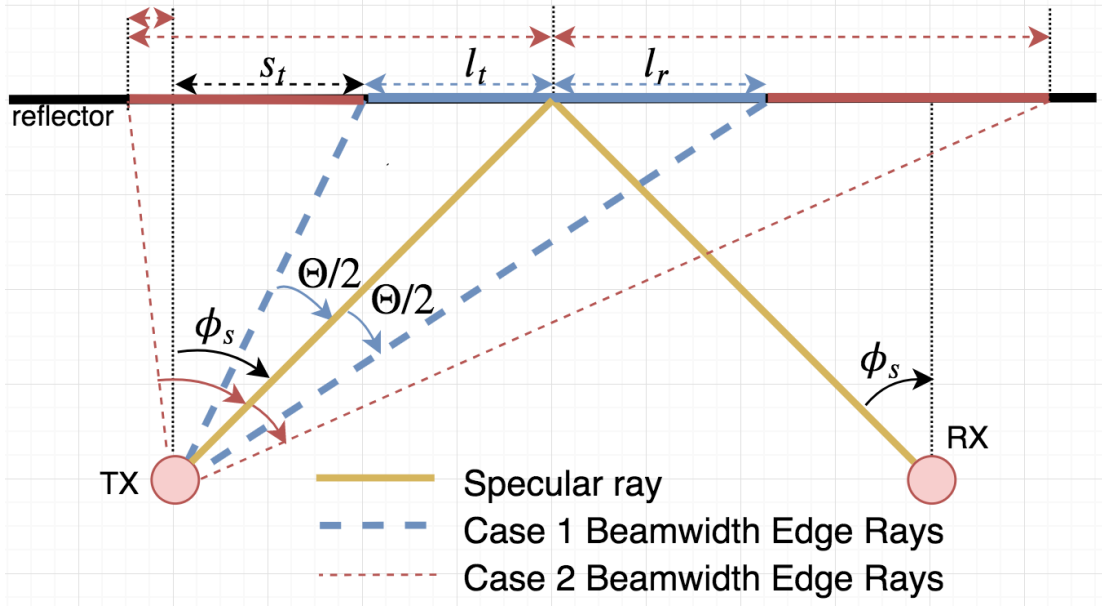


Figure 2.5: Transmitter beamwidth limitation

Table 2.2: Resultant Support Range for α

Case	Support Range	
$h_t \geq h_r$	α^-	$\max \{ \phi_s - 90^\circ, \alpha_{neg} \}$
	α^+	$\min \{ \phi_s - \sigma + 90^\circ, \alpha_{pos} \}$
$h_t < h_r$	α^-	$\max \{ \phi_s - \sigma - 90^\circ, \alpha_{neg} \}$
	α^+	$\min \{ \phi_s + 90^\circ, \alpha_{pos} \}$

where w_t and w_r are the transmitter and receiver side visible region lengths, respectively. As an example, in Fig. 2.4, we let the w_t to be limited by the reflector length. And w_r is limited by the transmitter beamwidth. Note that the knowledge of the reflector length is not enough as l_{pos} is not necessarily equal to l_{neg} . Hence, along with d , h_t , h_r and Θ , both sides reflector lengths, l_{pos} and l_{neg} , should be given as inputs to the model as well. Derivations of l_t and l_r are given in Appendix A.1.2.

In order to determine a range for the offset AoA due to the visible region, we backtrack the received rays that reflect from the endpoints of the region. Then, the offset AoA upper and lower bounds due to the visible region are

$$\alpha_{neg} < \alpha < \alpha_{pos} \quad (2.4)$$

where, $\alpha_{neg} = \phi_s - \tan^{-1}((d_1 \sin \phi_s + w_t)/h_r)$ and $\alpha_{pos} = \phi_s - \tan^{-1}((d_1 \sin \phi_s - w_r)/h_r)$.

Finally, combining with the reflection geometry limitation and having the tighter

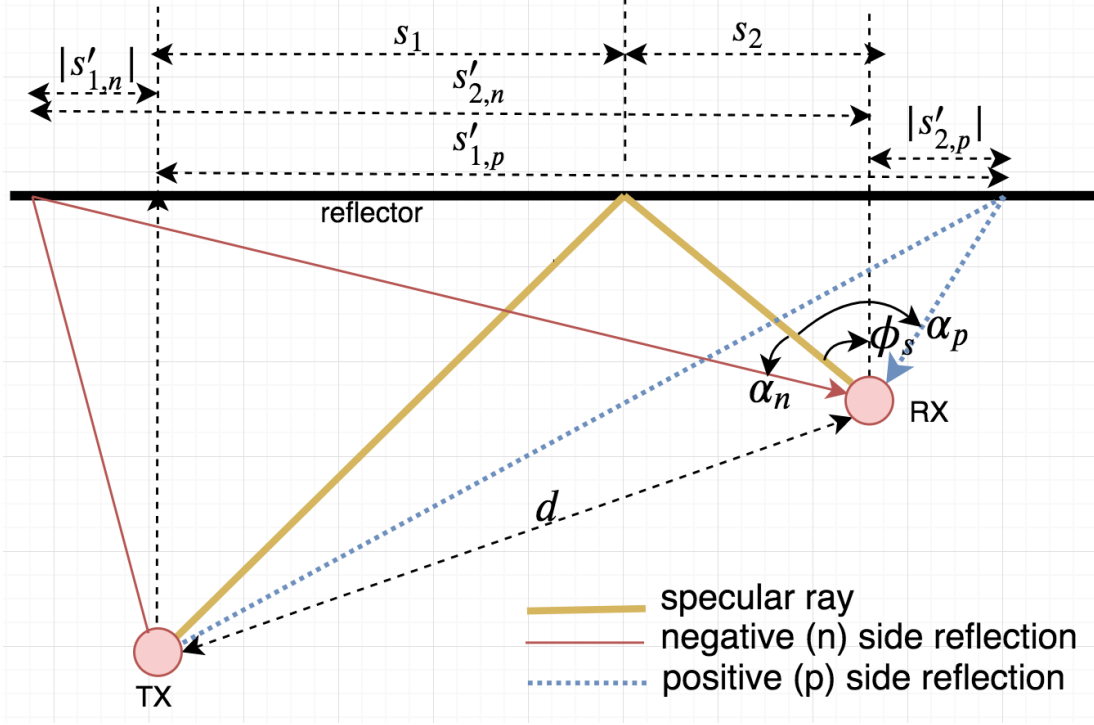


Figure 2.6: Diagrams for the cases diffuse ray reflects from out of the normals frame for positive (with α_p) and negative (with α_n) reflections

constraint on both sides, we give the expressions for the resultant support region for $h_t \geq h_r$ and $h_t < h_r$ in Table 2.2 with $\alpha \in [\alpha^-, \alpha^+]$ where, $\alpha^- < 0$ and $\alpha^+ > 0$.

2.3.5 Formulation Validation for Other Scenarios

In this subsection, we check the other scenarios of which given equations so far were not considering in the analytical setup. These scenarios can be basically defined as the reflections occur outside of the reflector normal frame which is demonstrated in Fig. 2.4. In Fig. 2.2 and 2.5, other scenarios are shown as Case 2 for reflector length and transmitter beamwidth calculation, respectively, while Fig. 2.6 is given for path length calculations. We claim that the setup formulations in the previous sections are still valid and refer the reader to Appendix A.1.3 for the proofs.

2.4 Intra-Cluster Channel Model Setup using Basic Geometric Model

In this section, using the BGM, we generate a first-order reflection cluster that consists of multiple rays as defined in Section 2.2. Throughout the chapter, we assume that both the channel and the transmitter-receiver pair are stationary. This implies that the channel impulse response (CIR) is time-invariant.

To estimate the channel parameters, we propose a *deterministic approach* where we let infinitely many rays depart from the transmitter. In particular, we will introduce the model setup, give a theoretical cluster CIR (TC-CIR) at the receiver antenna front, and calculate its parameters. Finally, we study how to bin the resultant profiles to get the practical multipath CIR. To do so, we create a novel mmwave spatial cluster model.

2.4.1 System Setup

Fig. 2.4 illustrates the infinitely many rays approach where the number of rays within the visible region is assumed to be infinity. To approximate the infinity number of rays, we digitize the support range with very small spacing ($\Delta\alpha$). So, the number of rays in digitized spatial domain is $N_r = \lfloor (\alpha^+ - \alpha^-)/\Delta\alpha \rfloor$ where α^+ and α^- are given in Table 2.2. Then, the offset AoA of k -th ray in the cluster

$$\alpha_k = (\alpha^-) + k\Delta\alpha \quad (2.5)$$

where $k = 0, 1, \dots, N_r - 1$, excluding the specular ray offset AoA of 0, i.e. $\alpha_s = 0$.

With these definitions, the BGM can be applied directly. This method scans for all α values within the support range with $\Delta\alpha$ increments. For every α_k , it calculates the τ_k , the delay of k -th ray within the cluster. Hence, the length and delay for the k -th ray in the cluster can be given as

$$l_k = \frac{h_r}{\cos(\phi_s - \alpha_k)} + \sqrt{h_t^2 + \left(s - \frac{h_r}{\cos(\phi_s - \alpha_k)} \sin(\phi_s - \alpha_k) \right)^2} \quad (2.6)$$

and $\tau_k = t_k - t_s$ where t_s is the ToA of the specular ray already defined in BGM and $t_k = l_k/c$ is the ToA of the k -th diffuse ray.

As a result, the baseband TC-CIR becomes

$$c(t, \omega) = a_s e^{j\varphi_s} \delta(t - t_s) \delta(\omega - \Omega_s) + \sum_{k=0}^{N_r-1} a_k e^{j\varphi_k} \delta(t - t_s - \tau_k) \delta(\omega - \Omega_s - \alpha_k) \quad (2.7)$$

where, t and ω are the reference ToA and AoA variables; a_s , φ_s , t_s , and Ω_s are the amplitude, phase, ToA and the AoA¹ of the specular ray; a_k , φ_k , τ_k , α_k are amplitude, phase, delay, offset AoA of the k -th ray, respectively. $\delta(\cdot)$ is Dirac delta function and N_r is the number of diffuse rays. In section 2.4.3 and 2.4.4 we will give the formulation for estimating the amplitudes a_k and phases φ_k for the k -th ray.

2.4.2 Directive Diffuse Scattering Model

In mmWave channels, even very tiny variations in a typical reflector create scattering since the wavelength is very small [7, 11, 18]. According to the measurement results at 60 GHz given in [24], received power due to the diffuse scattering was as high as 26% of the total cluster power. This implies that, diffuse scattering is a non-negligible component of the propagation mechanism in mmWave channels and thus, must be taken into account when modeling the cluster channels. The angular shape of the scattering event should also be modeled in order to estimate the directions (as well as the relative powers with respect to the specular ray) of the diffuse rays.

In [41], scattering event is modeled with 3 different patterns. According to the measurements, the directive pattern is the most accurate model and given in our context as

$$\rho_k(\psi_k, m_1, m_2) = m_2 \frac{((1 + \cos \psi_k)/2)^{m_1}}{\int_0^{180} ((1 + \cos \gamma)/2)^{m_1} d\gamma} \quad (2.8)$$

where, $\rho_k(\psi_k, m_1, m_2)$ is defined to be the relative diffuse scattering power coefficient of the k -th diffuse ray with respect to its specular reflected ray. Here, ψ_k is the angle between the specular reflected ray and the diffuse reflected ray of the k -th diffuse ray, reflector scattering characteristic parameters m_1 and m_2 are the width of the scattering pattern and the scaling loss factor, respectively. Note that the function reaches its

¹For the rest of the chapter, we refer AoA to the AoA with respect to LoS line, omitting the LoS reference point.

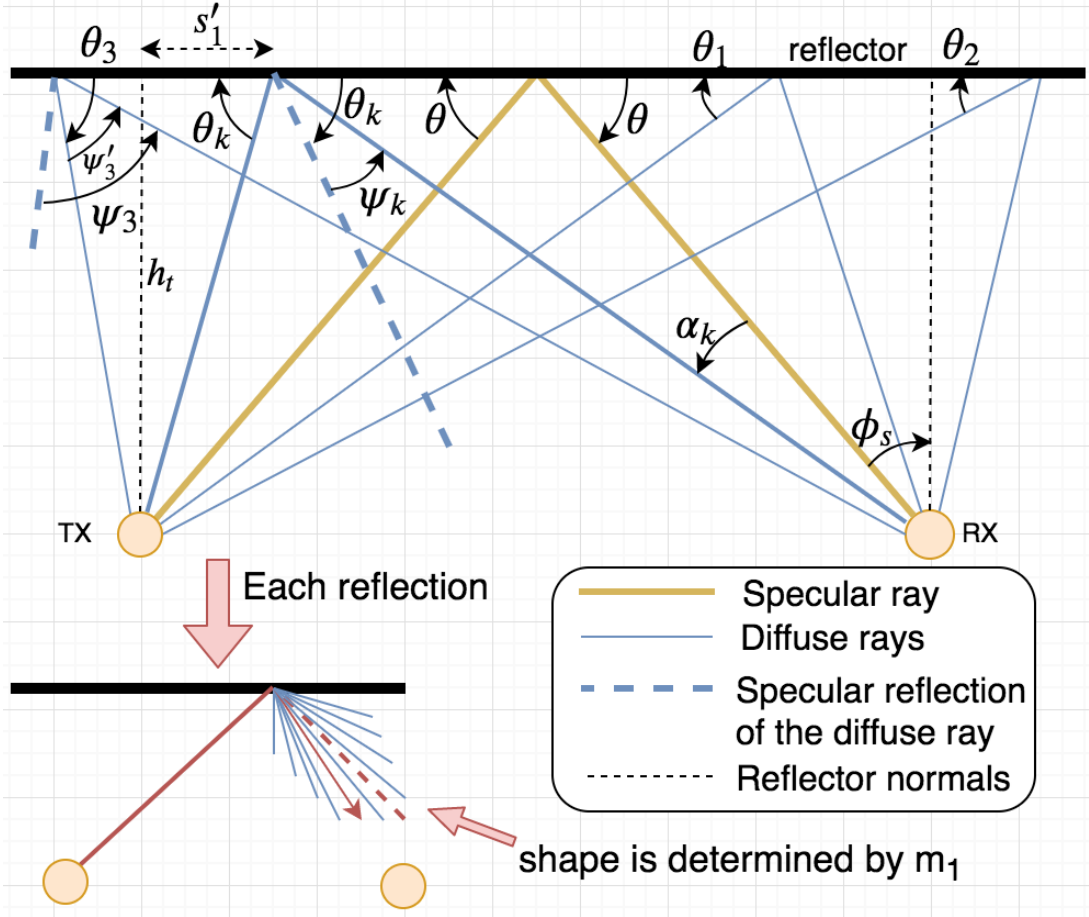


Figure 2.7: Updated cluster model diagram with the addition of diffuse scattering pattern

maximum at $\psi_k = 0$, i.e. specularly reflected ray of the k -th diffuse ray. And $\rho_k = m_2$ for $\forall m_1$ in this case. Note that, we have assumed m_1 to be equal for all k ; meaning that the roughness of the surface is uniform and doesn't depend on the grazing angle.

As the Fig. 2.7 demonstrates, scattering is assumed to occur at each reflection point of the incident ray, and only one ray in the scattered pattern can reach the receiver. Also note that each incident ray has its own grazing angle, θ_k . In this context, the BGM needs to be updated too. Consider the diffuse ray with the grazing angle θ_k in Fig. 2.7. Since only one reflected ray reaches the receiver, we only take one direction into account within the scattering pattern. In order to calculate the offset direction (ψ_k) of the k -th diffuse ray, first we need to find the grazing angle associated that ray, i.e. θ_k . From Snell's Law, grazing angle of the incident ray equals to the grazing angle

of the reflected specular. Then,

$$\theta_k = \tan^{-1} \frac{h_t}{|s'_1|} \quad (2.9)$$

where, s'_1 is given in Appendix A.1. ψ_k and α_k are negative in the diagram. Hence,

$$\psi_k = 90 - (\phi_s - \alpha_k) - \theta_k \quad (2.10)$$

We claim that the formulas are valid for all cases. The proof is provided in Appendix A.2.

2.4.3 Power Calculation of the Rays

We define the transmission equation for the k -th ray such that the received ray power is given as

$$P_k = \frac{P_T G_T G_R}{L_k R_k S_k} \quad (2.11)$$

where, P_T is the transmit power; G_T and G_R are the transmitter and receiver antenna gain, respectively; L_k , R_k and S_k are the losses applied to the k -th ray due to free space, reflection and scattering, respectively. In the following sections, we give expressions for L_k , R_k , S_k .

Free Space Loss

The path loss applied to the k -th ray in linear scale is

$$L_k = \left(\frac{\lambda}{4\pi l_k} \right)^2, \quad k = 0, 1, \dots, N_r - 1 \quad (2.12)$$

where, λ is wavelength of the carrier frequency and l_k is the length of the ray given in Eq. (2.6).

Reflection Loss

Reflection loss applied to the incident electric field can be characterized through the *Fresnel reflection coefficient* (Γ) [27]. The simplified versions of the equations for vertically and horizontally polarized k -th ray in our model are respectively given as,

$$\Gamma_k^{\parallel} = \frac{-\varepsilon_r \sin \theta_k + \sqrt{\varepsilon_r - \cos^2(\theta_k)}}{\varepsilon_r \sin \theta_k + \sqrt{\varepsilon_r - \cos^2(\theta_k)}} \quad (2.13)$$

$$\Gamma_k^{\perp} = \frac{\sin \theta_k - \sqrt{\varepsilon_r - \cos^2(\theta_k)}}{\sin \theta_k + \sqrt{\varepsilon_r - \cos^2(\theta_k)}} \quad (2.14)$$

where, θ_k is the grazing angle defined in Eq. (2.9) and ε_r is the relative permittivity of the reflection material which doesn't depend on the carrier frequency [25, 40].

As a result, reflection loss coefficients in linear scale for k -th ray are defined as

$$R_k = \begin{cases} R_k^{\parallel} = 1/|\Gamma_k^{\parallel}|^2 & \text{if vertical pol.} \\ R_k^{\perp} = 1/|\Gamma_k^{\perp}|^2 & \text{if horizontal pol.} \end{cases} \quad (2.15)$$

Scattering Loss

The scattering loss is studied in [39] and the loss coefficient for the specular component is given as

$$\rho_s(\theta) = \exp \left(-0.5 \left(\frac{4\pi\sigma_h}{\lambda} \sin \theta \right)^2 \right) \quad (2.16)$$

where, σ_h is the standard deviation of the surface height (h) about the local mean within the first Fresnel zone, λ is the carrier wavelength, and θ is the grazing angle. Here, variations on the surface at a surface height, h , is modeled as a Gaussian distributed random variable [25].

On the other hand, for the k -th incident ray, the relation between the power degradation at k -th specular ray and its any diffuse ray is given in Eq. (2.8) via a scattering pattern.

Hence, the scattering loss for the k -th ray can be given as

$$S_k = \left(\frac{1}{\rho_{s,k}\rho_k} \right)^2 \quad (2.17)$$

where, $\rho_{s,k}$ is the specular ray coefficient that expresses the loss applied to the k -th incident ray caused by the roughness of the material and is given by $\rho_{s,k} = \rho_s(\theta_k)$, and ρ_k is the coefficient that accounts the loss due to the power dispersion after scattering given in Eq. (2.8).

Finally, since we introduce amplitudes in the cluster channel model in Eq. (2.7), power can be converted to absolute value of amplitudes via $|a_k| = \sqrt{P_k}$.

2.4.4 Phase Calculation of the Rays

Reflected rays arrive at the receiver with different phases due to the difference in their path lengths and at a grazing angle. Hence, in order to be able to sum the ray powers properly, phase information of each ray should be calculated deterministically.

Phase Offset due to Path Distances

The phase offset of the k -th ray due to the path difference with respect to the specular ray can be given as $\Delta\varphi_{D,k} = (2\pi(l_k - l_s))/\lambda$.

Phase Offset due to Reflection

Note that Fresnel equations given in (2.13) and (2.14) are complex coefficients. Hence, we can define the phase offset introduced by the reflection to the k -th ray as

$$\Delta\varphi'_{R,k} = \begin{cases} \angle\Gamma^{\parallel} & \text{if vertical pol.} \\ \angle\Gamma^{\perp} & \text{if horizontal pol.} \end{cases} \quad (2.18)$$

In order to be able to calculate a total phase offset of a ray, we need to align the phase to the same reference (specular ray phase offset) with the previous subsection. Hence, we correct the phase offset of the k -th ray due to the reflection with respect to the specular ray as $\Delta\varphi_{R,k} = \Delta\varphi'_{R,k} - \Delta\varphi'_{R,spec}$.

Overall, phase offset of the k -th ray with respect to the specular ray is given as

$$\Delta\varphi_k = \Delta\varphi_{D,k} + \Delta\varphi_{R,k} \quad (2.19)$$

Note that, $\Delta\varphi_k = \varphi_k - \varphi_s$. Further, assuming $\varphi_s = 0$, $\Delta\varphi_k = \varphi_k$.

2.4.5 Binned Intra-Cluster Channel Model

Since all the rays are not resolvable by the receiver due to limited resolution, an additional discrete binning is needed on top of the theoretical approach given in Section 2.4.1. The resultant CIR can be viewed in the time domain and/or in the angle domain. While the time resolution is determined by the baseband signal bandwidth, the angle resolution is a measurement/beamforming system parameter. Note that the number of multipath components (MPCs) in time domain is not necessarily equal to the number of MPCs in angle domain as the relation between AoA and ToA of the ray is nonlinear. Hence, angle and time profile of the channel from the theoretical response should be derived separately. In this chapter, for the sake of brevity, we only provide the angle profile. But, it is worthwhile to note that the derivation of the time profile is analogous.

The binning process comprises of two stages: (1) filtering over an angle period which is called a "bin" and (2) sampling at the beginning of each bin which results in a "sample" or a MPC. We perform binning over 360° as the BGM doesn't impose any limitation on the AoA. Hence, defining $\Delta\tilde{\alpha}$ is the angle resolution, the maximum number of nonzero MPCs in the resultant angle profile is $\tilde{N}_r = \lceil 360/\Delta\tilde{\alpha} \rceil$.

Here, we define $\Omega_k = \alpha_k + \Omega_s$ as the k -th ray AoA. From Eq. (2.5), Ω_0 is the starting angle of the cluster in the support range. Assuming that the binning starts exactly at 0° , the starting index of the cluster in the binned version is $q = \lfloor \Omega_0/\Delta\tilde{\alpha} \rfloor$. Then, $0 \leq q \leq \tilde{N}_r - 1$. Finally, the number of nonzero MPCs in the cluster is $N_{nz} = \lceil (\alpha_{N_r-1} - \alpha_0)/\Delta\tilde{\alpha} \rceil$.

With these definitions, the resultant discrete angle impulse response for the cluster (C-CIR) can be given as following:

$$\tilde{c}[n] = \sum_{i=q}^{q+N_{nz}-1} \tilde{a}_{i-q} e^{j\tilde{\varphi}_{i-q}} \delta[n-i] \quad (2.20)$$

where, $\delta[\cdot]$ is the Kronecker delta function and n is the reference AoA index. \tilde{a}_l and $\tilde{\varphi}_l$ are amplitude and phase of the $l = (i - q)$ -th MPC, respectively. They are obtained via the phasor summation of the rays within the bin and can be shown as

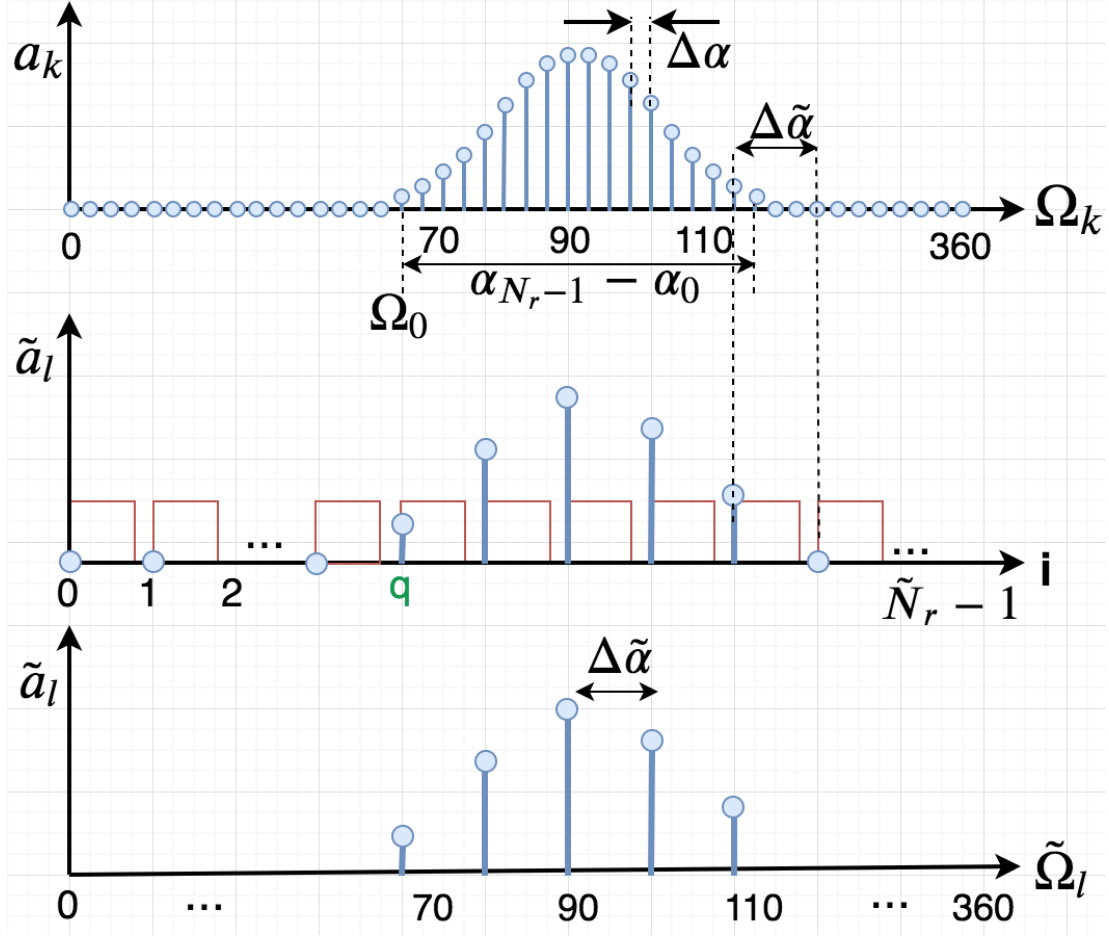


Figure 2.8: Example illustration of the binning procedure.

$$\tilde{a}_l e^{j\tilde{\varphi}_l} = \sum_{t=lN_b}^{(l+1)N_b-1} a_t e^{j\varphi_t} \quad (2.21)$$

where, $l = 0, 1, \dots, N_{nz} - 1$ and $N_b = \lfloor \Delta\tilde{\alpha}/\Delta\alpha \rfloor$ is the number of rays within a bin.

Finally, AoA mapping of MPCs from the index domain to the angle domain can be given as $\tilde{\Omega}_l = (q + l)\Delta\tilde{\alpha}$. An example illustration of the overall process is shown in Fig. 2.8.

In the final step, MPCs that have power lower than the receiver sensitivity are discarded. That is, whenever $10 \log |\tilde{a}_l|^2 < P_{RS}$ where, P_{RS} is the receiver sensitivity, the MPC is removed from the C-CIR.

To summarize the overall proposed model, a flowchart showing the operations required to obtain the time and angle domain representations of the cluster for a particular

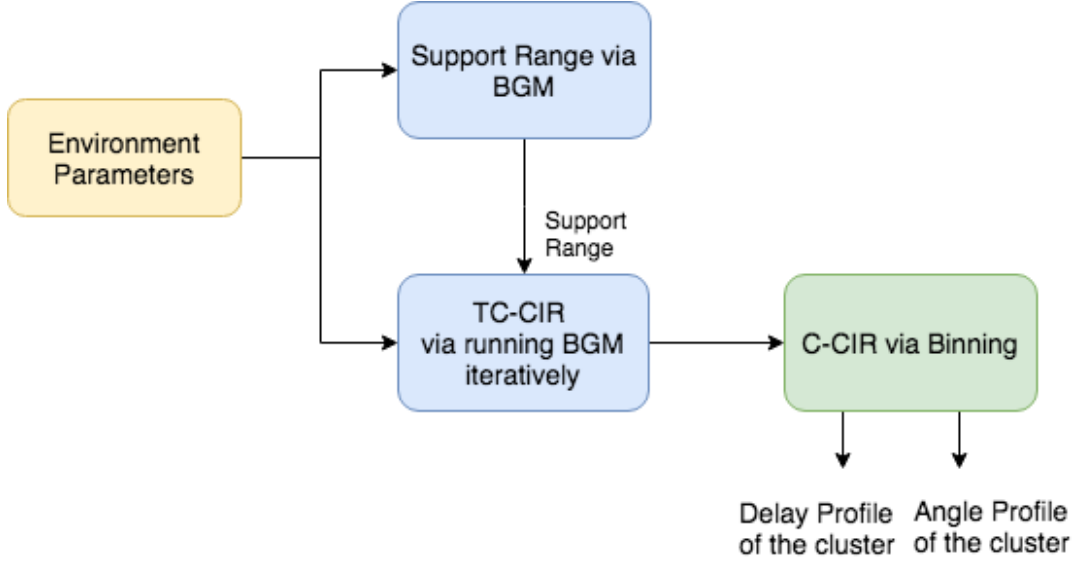


Figure 2.9: Flowchart diagram of the C-CIR generation.

communication system is given in Fig. 2.9.

2.5 Extension to MIMO

2.5.1 Angular Channel Impulse Response

In this chapter, we created a channel model for the cluster in the channel. However, the extension model that covers the overall channel can also be introduced. Assuming that the channel has N_{cl} non-overlapping first order reflection clusters, extension of the cluster parameters are straightforward. The k -th ray AoA of the j -th cluster is $\Omega_k^{(j)} = \alpha_k^{(j)} + \Omega_s^{(j)}$ where, $\Omega_s^{(j)}$ and $\alpha_k^{(j)}$ are the specular ray AoA and the k -th ray offset AoA of the j -th cluster, respectively. Then, $\Omega_0^{(j)}$ is the starting AoA of the j -th cluster. After binning the theoretical response, starting AoA index of the j -th cluster is given as $q^{(j)} = \lfloor \Omega_0^{(j)} / \Delta\tilde{\alpha} \rfloor$ where, $0 \leq q^{(j)} \leq \tilde{N}_r - 1, \forall j$. Finally, the number of nonzero MPCs in the j -th cluster is $N_{nz}^{(j)} = \lceil (\alpha_{N_r-1}^{(j)} - \alpha_0^{(j)}) / \Delta\tilde{\alpha} \rceil$.

Then, the discrete channel angle response that only considers single-order reflection clusters is given as

$$\begin{aligned}
h[n] &= \sum_{j=0}^{N_{cl}-1} \tilde{c}^{(j)}[n] \\
&= \sum_{j=0}^{(N_{cl}-1)} \sum_{i=q^{(j)}}^{(q^{(j)}+N_{nz}^{(j)}-1)} \tilde{a}_{i-q^{(j)}}^{(j)} e^{j\tilde{\varphi}_{i-q^{(j)}}^{(j)}} \delta[n-i]
\end{aligned} \tag{2.22}$$

where, $\tilde{c}^{(j)}[n]$ is discrete channel angle response of the j -th cluster given in Eq. (2.20). After plugging it into the equation, we get the result in Eq. (2.22) where, we define $\tilde{a}_l^{(j)}$ and $\tilde{\varphi}_l^{(j)}$ are amplitude and phase of the l -th MPC of the j -th cluster, respectively. Here, $l = i - q^{(j)} = 0, 1, \dots, N_{nz}^{(j)} - 1$. Note that Eq. (2.22) still has $\tilde{N}_r = \lceil 360/\Delta\tilde{\alpha} \rceil$ bins.

Analogous to the single cluster case, absolute AoA of the l -th MPC of the j -th cluster can be obtained by $\Omega_l^{(j)} = (q^{(j)} + l)\Delta\tilde{\alpha}$.

2.5.2 LoS Ray Parameters

Note that, if the scenario is LOS, we will consider that one of the clusters will be through LOS, i.e. no reflection. As in other ray tracing algorithms, we model that cluster with the single LOS ray. In this case, LOS ray AoA is $\Omega_{LOS} = 0$. And its power in linear scale is given by $P_{los} = (P_T G_T G_R / L_{los})$ where L_{los} is the LOS ray attenuation due to the free space path-loss and given as $L_{los} = (\lambda/4\pi d)^2$.

2.5.3 MIMO Beamformed Channel Angle Response

In the BGM setup, we discuss the cluster angle spread limitation due to transmit beamwidth. In mmWave MIMO systems, owing to the large antenna arrays, very small values of antenna beamwidth can be accomplished. For instance, less than 1° beamwidth can be achieved using 64 antenna elements [27]. This makes the transmit beamwidth a dominant limitation factor in our intra-cluster model, especially for indoor environments. The same phenomenon occurs in outdoor mmWave applications if massive MIMO is used in the communication system where even smaller beamwidth can be achieved. This is because h_t is also a factor that determines the beamwidth limitation

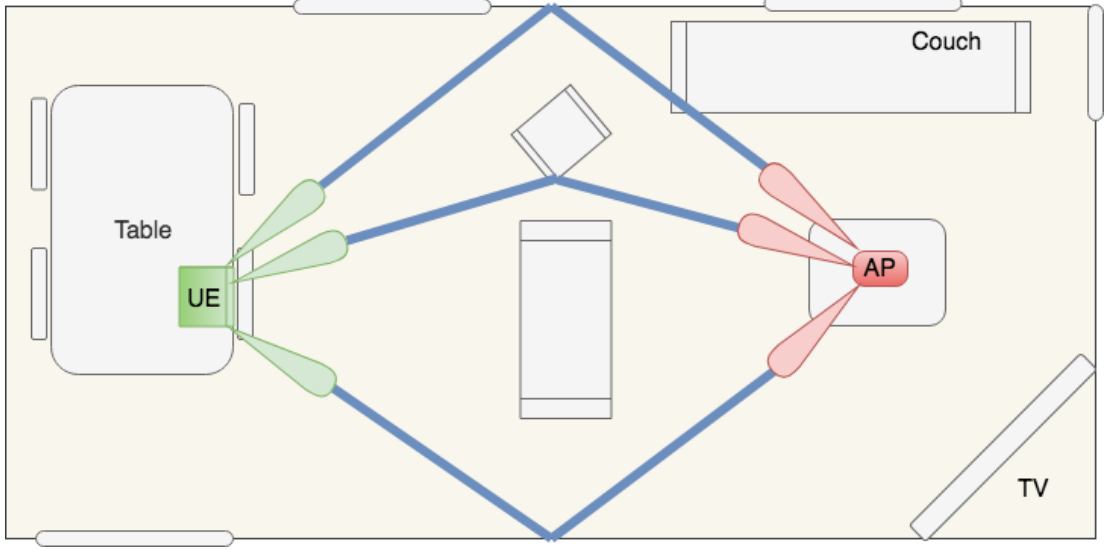


Figure 2.10: Illustration of the non-overlapping first-order clusters in a MIMO communication scenario within a typical living room environment

and it should be relatively small to keep the transmit beamwidth as a dominant limiting factor. As a result, several spatially separated single-order reflection clusters are provided within the channel. Further, if the transmitter and receiver have the enough number of RF chains to create and process all clusters independently at the same time, a beamformed link can be provided to each cluster. Fig. 2.10 gives an example for a typical living room with 3 clusters and corresponding beams at the transmitter and receiver.

Proceeding with the consideration of a dedicated transmit-receive beamformed link per cluster, each cluster can be modeled as a SISO channel. Further, we consider that the clusters are perfectly separated in the spatial domain. That is, the beams aligned to the different first-order reflection directions do not overlap with each other. With this assumption, the extension to MIMO becomes straightforward and the beamformed channel matrix reduces to

$$\mathbf{H} = \begin{bmatrix} \mathbf{h}_{11} & 0 & \dots & 0 \\ 0 & \mathbf{h}_{22} & \dots & 0 \\ \vdots & \vdots & \ddots & \vdots \\ 0 & 0 & \dots & \mathbf{h}_{N_{cl}N_{cl}} \end{bmatrix} \quad (2.23)$$

where, \mathbf{h}_{jj} is the beamformed link coefficient vector for the j -th cluster. In this

case, the angle domain representation given in Eq. (2.22) becomes the beamformed link angle response and $\tilde{\alpha}_l^{(j)}$ constitutes \mathbf{h}_{jj} .

2.6 Conclusion

In this chapter, we create a ray tracing intra-cluster model, RT-ICM, for mmWave channels that includes only the first-order reflection rays. We also take diffuse scattering into account as the scattering has a non-negligible contribution in mmWave channels. Specifically, we aim at a spatial representation of the cluster at the receiver end. Further, since the mmWave channels are sparse and clusters are spatially separated most of the time, we claim that the proposed intra-cluster model can be generalized to the MIMO channel model simply by replicating it for each cluster. We discuss that, in fact, the transmit beamwidth can be the dominant limitation factor on the clusters angle spread in MIMO applications; thereby increasing the number of first-order clusters further. The model we build here will give insight to the beamformer designs in mmWave for stationary environments. In the next chapter, we implement the model to a literature measurement scenario and show that our intra-cluster model estimates the angular spectrum with high accuracy. Furthermore, we will validate the model using a full scan EM solver software.

Chapter 3

Implementation and Validation of RT-ICM

Understanding millimeter-wave (mmWave) channels is still a popular research area. In order to increase the beamforming efficiency, optimum spatial usage of the channel is targeted. While the mmwave channel behavior is understood with several measurements and channel models, however, only a little study is present that discusses the angular characteristics of mmWave bands at the cluster-level. In the previous chapter, we addressed this need at mmWaves and proposed a ray-tracing based intra-cluster model (RT-ICM) for stationary environments, by considering only first-order reflections. In this chapter, we validate RT-ICM by implementing and comparing it to published measurements made in a classroom at 60 GHz. We investigate its accuracy further by comparing it with an electromagnetic (EM) solver software results. Furthermore, we show that the RT-ICM results agree with measurement-based IEEE 802.11ad intra-cluster model results. We demonstrate that, due to its extremely simplified computation, RT-ICM estimates the channel parameters with high accuracy. Finally, since RT-ICM provides the cluster power angle profile, we discuss the insight about how this result can increase the beamforming efficiency.

3.1 Incoherent and Coherent Power Calculations

The proposed cluster channel model comprises three main steps; namely, basic geometry modeling, theoretical cluster modeling, and binned channel impulse response generation. First, Basic Geometric Model (BGM) takes the environment parameters regarding the first-order reflection as inputs and generates the supported angle spread (SAS), $S_{\Omega} = \alpha_{N_r-1} - \alpha_0$, at the receiver. Second, running the BGM for each diffuse ray within the supported angle spread; angle, time, power and phase of the rays

are calculated; thereby generating the theoretical cluster impulse response. The output theoretical baseband cluster impulse response (TC-CIR) is given in 2.7. Finally, TC-CIR is binned in the angle domain according to the angle resolution of the communication/measurement system. Basically, the binned version is the impulse response that the receiver *sees*. We simply call it cluster channel impulse response (C-CIR) given in 2.20.

In this context, we are able to calculate the total power at the front of the receiver antenna and after the receiver processing, i.e. after resolution is applied. We call the former as *incident cluster power* and the latter as *received power*. Respectively, they can be given as followings:

$$P_i = (a_s)^2 e^{j\varphi_s} + \frac{S_\Omega}{N_r} \sum_{k=0}^{N_r-1} (a_k)^2 e^{j\varphi_k} \quad (3.1)$$

$$P_r = \frac{S_\Omega}{N_{nz}} \sum_{l=0}^{N_{nz}-1} (\tilde{a}_l)^2 \quad (3.2)$$

where, N_{nz} is the number of received nonzero multipath components (MPCs); \tilde{a}_l and $\tilde{\varphi}_l$ are the amplitude and phase of the l -th bin (or MPC), respectively. Note that once receiver resolves the MPCs, their phases are irrelevant. Also, we calculate the incoherent incident power which is, basically, what an omnidirectional antenna would have received. For completeness, we give the coherent incident cluster power as,

$$P_{i,C} = (a_s)^2 + \frac{S_\Omega}{N_r} \sum_{k=0}^{N_r-1} (a_k)^2 \quad (3.3)$$

In all equations, S_Ω/N_r or S_Ω/N_{nz} term is inserted for the integral approximation.

3.2 Full Scan EM Software

We use Wireless Insite® as a full scan electromagnetic (EM) propagation software. This software is selected due to its accuracy, specifically, at site-specific mmWave applications. Furthermore, it also takes diffuse scattering into account by introducing material roughness in the environment. In that aspect, Wireless Insite® is the most comparable software with RT-ICM results. In this section, we briefly state how the software works and show the main differences to RT-ICM.

The software predicts the channel using a 3-D ray-tracing model. With user specified ray spacing, it generates rays from the transmitter (TX) and applies reflection, diffraction and diffuse scattering channel impairment mechanisms based on the environment.

The software uses the diffuse scattering model given in [41]. Briefly, it divides the reflection surface into tiny facets and calculates the electric field of the ray that hits to each facet. After integrating over the entire surface, it displays two aggregated diffuse paths at power weighted average points on the surface. That means that the software displays the aggregated path angle of arrivals, not actual paths. By using the model given in [41], the software is able to provide the specular power and diffuse power at the receiver for each reflector; thereby providing a total power for each cluster, i.e. total cluster power.

On the other, RT-ICM divides the *receiver* side into many incoming rays based on the pre-calculated supported angle spread, S_Ω . It traces all diffuse rays individually; thereby creating a detailed power profiles at the receiver. Therefore, while we will compare the coherent and incoherent received power and cluster AoAs with the software, the cluster angle distribution will not be compared.

Finally, the software doesn't consider the receiver resolution. However, the channel sounding measurements impose angle resolution by means of its technique. In the applications, beam scanning during beamforming setup creates the angular footprint at the receiver, which also introduces angular resolution. RT-ICM addresses this phenomenon with an additional binning step. Hence, we will be able to compare and validate RT-ICM via the full scan software as well as the measurement results.

3.3 Implementation

In this section, we implement the proposed ray tracing channel model, RT-ICM, using the experimental platform performed in [16]. We express the measurement scenario briefly and then describe how we replicate it in RT-ICM and in the software with respect to parameters selection and settings.

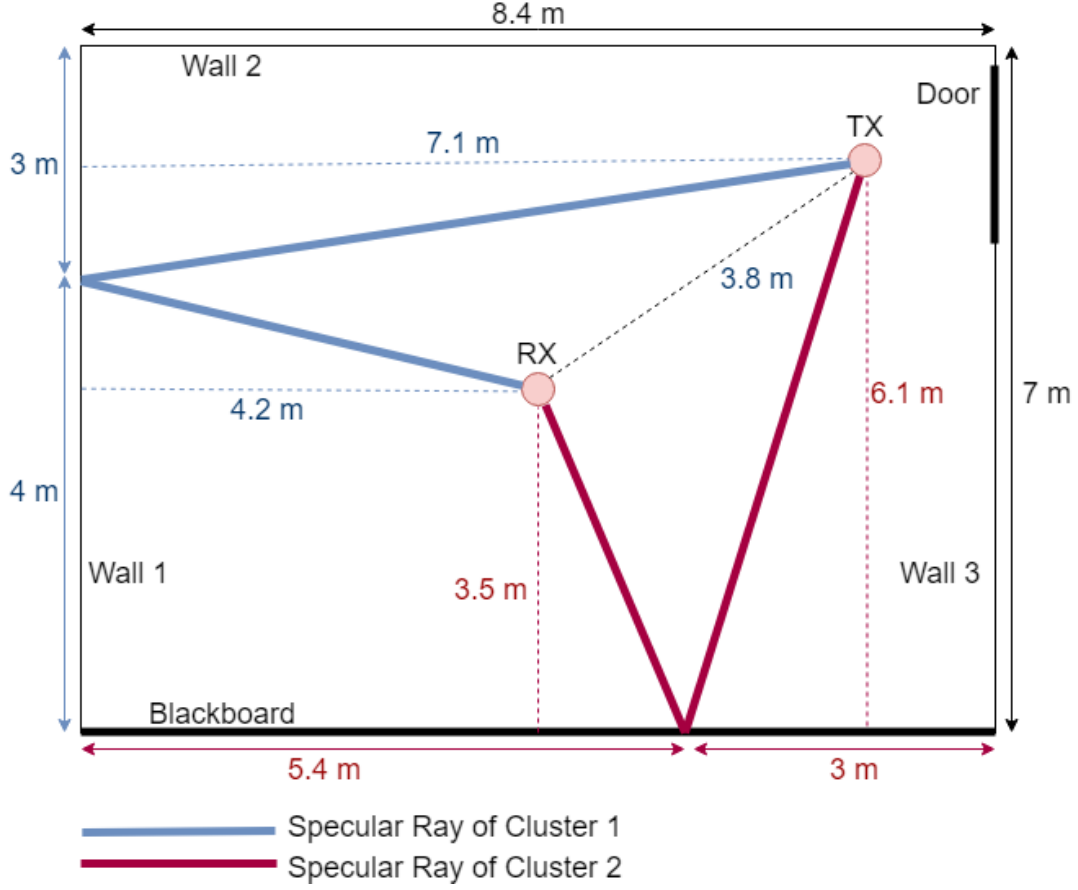


Figure 3.1: Measurement environment and the distance parameters when receiver is in the room center.

3.3.1 Indoor 60 GHz - Classroom Environment [16]

In [16], several measurements are held to characterize the spatial and temporal behaviors of the indoor channels at 60 GHz. Totally, 8 experiments are performed in 4 types of environments. Those environments were room, hallway, room to room and corridor to room. Both measurement and statistical results are provided for each measurement. Since the data is collected using spin measurements, power angle profile of the channel is also created. In this chapter, we will replicate the measurement environment and the system parameters for the two classroom measurements in [16] and implement the proposed channel model.

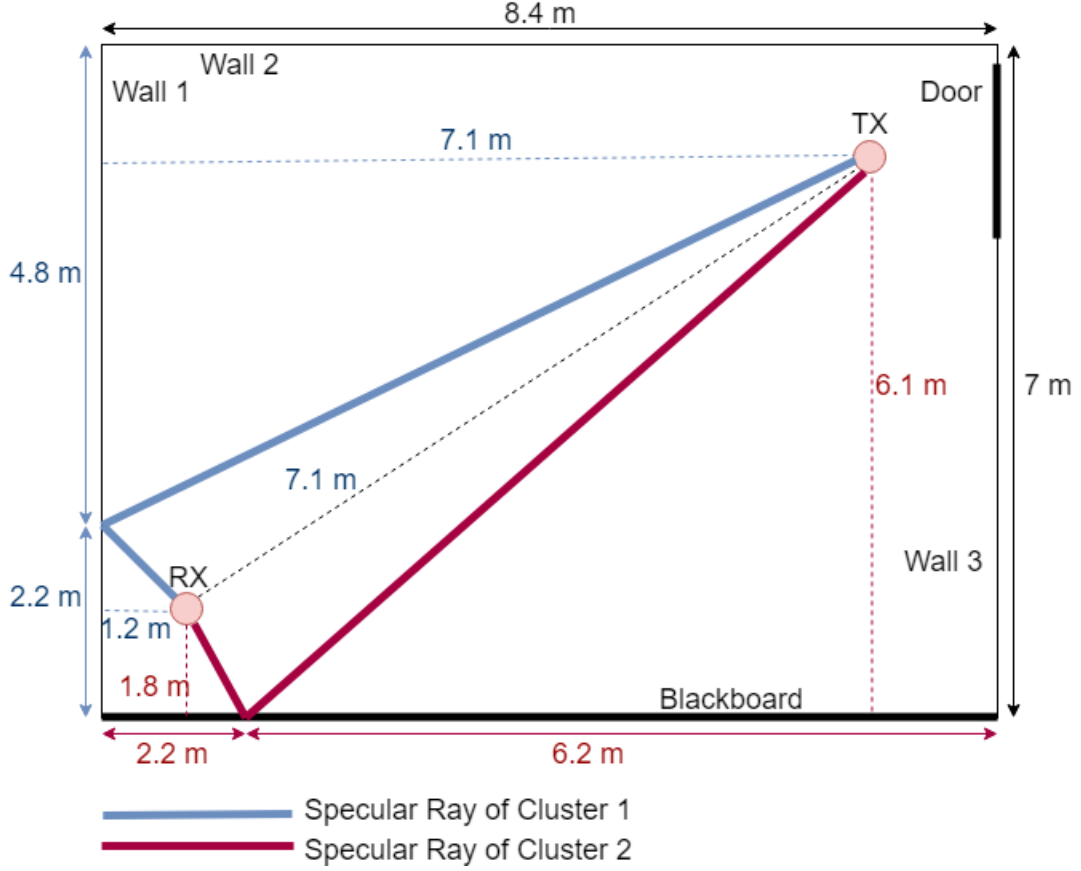


Figure 3.2: Measurement environment and the distance parameters when receiver is in the room corner.

Receiver is at the Center

The top view of the measurement environment is sketched in Fig. 3.1. In this first scenario, transmitter is located at the corner and the receiver is in the center of an 8.4×7 m empty room. One side of the room is covered with a blackboard while the others are indoor building walls. Transmitter has a horn antenna with a beamwidth of 90° which is directed towards the receiver. And the angle resolution during the spin measurements at the receiver is given as 5° .

Receiver is on the Corner

The measurement environment is sketched in Fig. 3.2 for the second scenario where the receiver is placed on the corner. All parameters kept same.

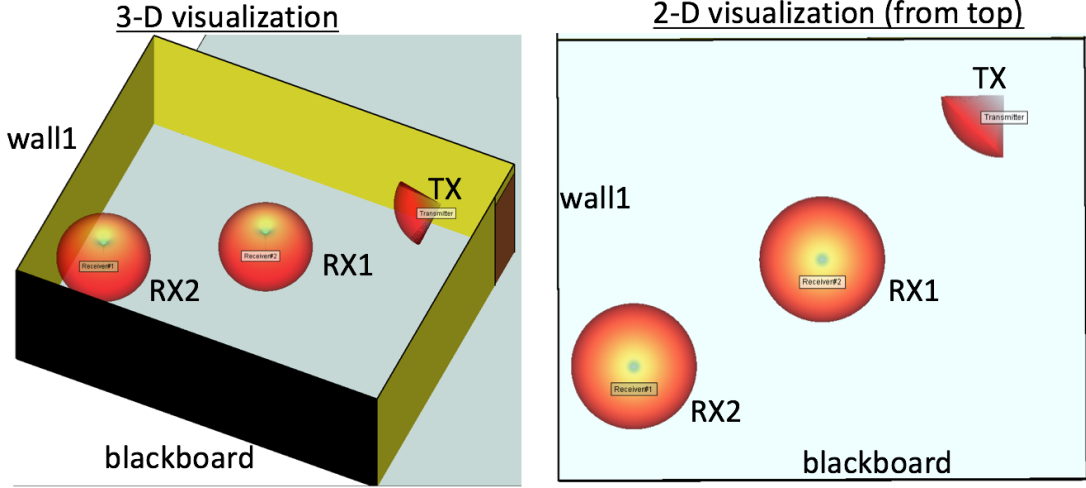


Figure 3.3: Environment and measurement scenario created in Wireless Insite.

3.3.2 RT-ICM Setup

Although 4 potential reflectors are present within the room, the only possible first-order reflections are through the "Wall-1" and "Blackboard" that are shown in Fig. 3.1. The transmit beamwidth for each cluster is assumed to be $\Theta = 45^\circ$. We set the diffuse scattering pattern order $m_1 = 17$ for the plasterboard wall-1 and $m_1 = 25$ for the blackboard (made of slate-stone). The scaling factor for these materials are $m_2 = 23$ and $m_2 = 19$, respectively. These trade-off parameters are fine-tuned such that the angle spread and received power are in good agreement with measurements. In that way, a parameter pair (m_1, m_2) is obtained for each material. We pick $N_r = 1000$ as the larger values don't contribute significant difference. Finally, based on the measurement results, we choose the power threshold as $P_{RS} = -70$ dBm. The other parameters for the clusters are given in Table 3.1.

3.3.3 Wireless Insite® Setup

We replicate the environment in 3-D as shown in Fig. 3.3. The walls and blackboard materials are selected to be plasterboard and slate stone, respectively. The ground is concrete but the ceiling is ignored. We use the same distance parameters as in RT-ICM. A directional antenna with 90° azimuth and elevation beamwidth is set for the transmitter. On the other hand, to replicate the channel sounding measurements, an

Table 3.1: Input Parameters of the Model (d , h_t , h_r , l_{neg} , l_{pos} [meters], σ_h [mm]) P_T [dBm], G_T , G_R [dB], P: polarization, V:vertical, H: horizontal)

Measurement (Cluster - P)	d	h_t	h_r	l_{neg}	l_{pos}	ε_r	σ_h	P_T	G_T	G_R
Room-center (1-H)	3.8	7.1	4.2	4	3	2.9	0.3	25	6.7	29
Room-center (2-H)	3.8	6.1	3.5	3	5.4	7.5	0.1	25	6.7	29
Room-corner (1-H)	7.1	7.1	1.2	2.2	4.8	2.9	0.3	25	6.7	29
Room-corner (2-H)	7.1	6.1	1.8	6.2	2.2	7.5	0.1	25	6.7	29

omnidirectional antenna is used for the receiver. All antennas are aligned at the same height.

The parameters for diffuse scattering model are selected as followings: scattering width (α) is $\alpha = 5$ and $\alpha = 8$; scaling factor (S) is $S = 0.4$ and $S = 0.2$, and cross-polarization factor (X) is $X = 0.2$ and $X = 0.2$, all, respectively, for wall1 and blackboard. We set the maximum number of reflections as 16, diffraction as 1. In order to shorten the computational time, the diffuse scattering is taken into account only from the last reflection for each path. Finally the ray spacing is 0.05. The list of other parameters is given in Table 3.1.

3.4 Simulation Results

In this section, we compare the RT-ICM results with the measurement and EM software results. As we discussed in Sec. 3.2, Wireless Insite® does not provide the ray-level power profiles at the output due to the aggregation of diffuse rays. Also, it doesn't consider the angle resolution when calculating the received power. Hence, we split the comparison into two, (1) angle dispersion and binned peak power comparison with measurement results (2) total, specular and diffuse power with software results. Cluster AoAs are comparable for all three results.

Finally, we create another subsection here to compare the results with the indoor channel model adopted in IEEE 802.11ad and IEEE 802.11ay.

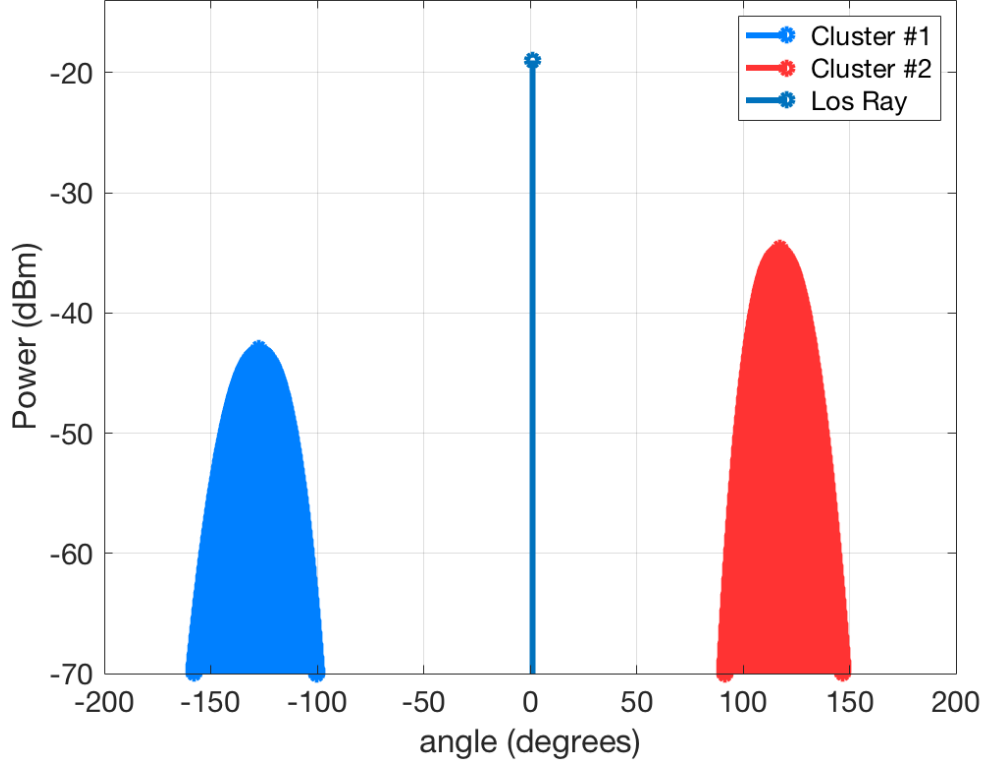


Figure 3.4: Theoretical Power Angle Profile of the channel when receiver is in the center of the room.

3.4.1 Comparison with Measurement Results

Receiver is at the Center

For center receiver test, the resultant theoretical angle domain response of the model is given in Fig. 3.4. The ray that arrives with zero AoA is the LOS ray. Resultant specular ray AoA cluster-1 and cluster-2 are $\Omega_s^{(1)} = -127^\circ$ and $\Omega_s^{(2)} = 117^\circ$, respectively. Supported angle spreads of the clusters are $S_\Omega^{(1)} = 57^\circ$ for cluster-1 and $S_\Omega^{(2)} = 55^\circ$ for cluster-2. The angular spectrum and the numerical values are in agreement with the measurement result figure provided in [16] which shows the AoAs as -128° and 118° and the approximate angle spreads as 55° and 40° .

On the other hand, to compare the power spectrum in angle domain, power angle profile result after the binning (with $\Delta\tilde{\alpha} = 5^\circ$) is provided in Fig. 3.5. The received peak powers of cluster-1 and cluster-2 relative to that of LOS ray are 21 dB and 11 dB.

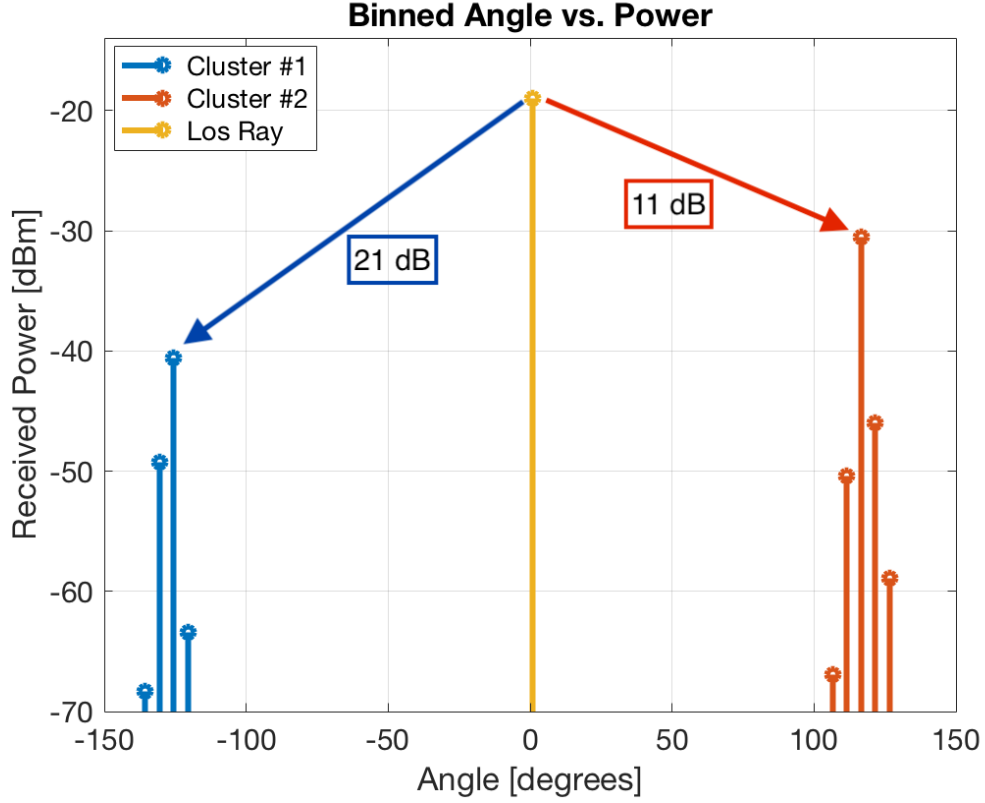


Figure 3.5: Binned Power Angle Profile of the channel when receiver is in the center of the room.

These also match with measurement results where they were approximately 19 dB for cluster-1 and 9 dB for cluster-2.

Receiver is on the Corner

The measurement environment is drawn in Fig. 3.2 for the second scenario where the receiver is placed on the corner. The parameters are given in Table 3.1.

Theoretical angle response given in Fig. 3.6 shows that the cluster-1 has an AoA of -120° whereas the cluster-2 AoA is 91° . Their supported angle spreads are 79° and 64° . The measurement result figure in [16] gives the AoAs as -120° and 90° and the spreads approximately are 50° and 58° for the cluster-1 and cluster-2, respectively. Similar to the previous measurement, binned version of the angle spectrum is given in Fig. 3.7. As seen, the relative received peak powers of cluster-1 and cluster-2 are 8 dB and 1 dB. They are approximately 7 dB and 0 dB in the measurements.

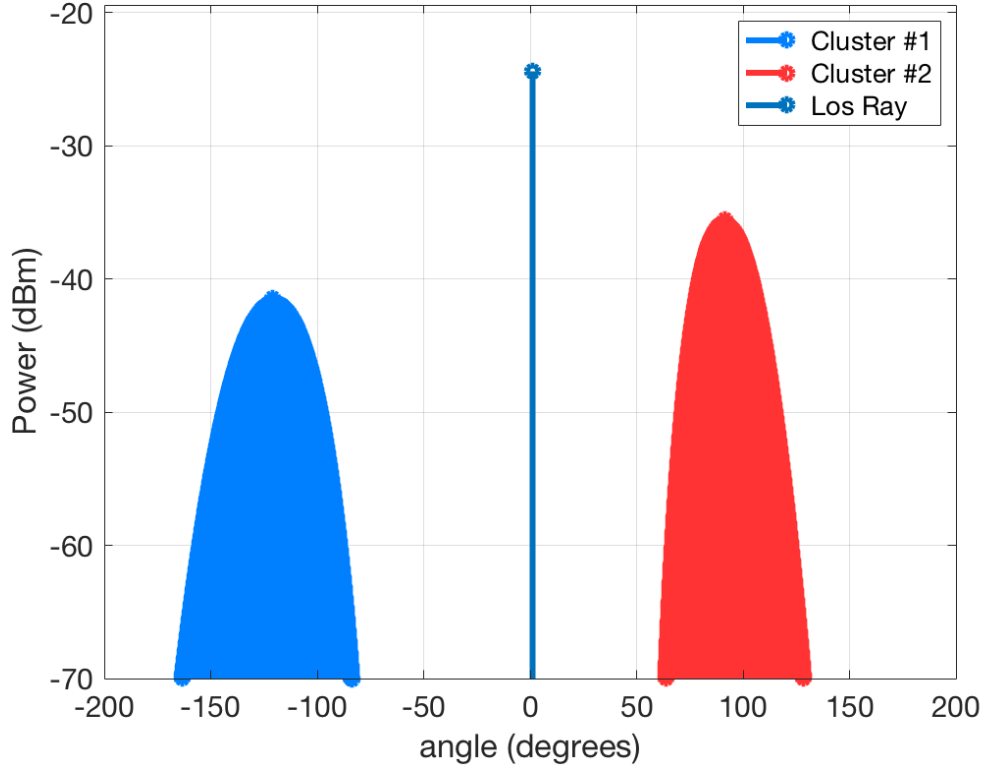


Figure 3.6: Theoretical Power Angle Profile of the channel when receiver is in the corner of the room.

3.4.2 Comparison with Wireless Insite®

Receiver is at the Center

Although we set the number of paths as 100 in the software, the path number that exceeds the power threshold of -70 dB is only about 20 – 25. And those are mostly from the first-order reflections. The visualization of the paths that exceed the threshold are shown in Fig. 3.8. Same effect is seen when the receiver is on the corner.

As seen from the AoA comparison of RT-ICM and the software in Fig. 3.9, the RT-ICM captures most of the channel information by only considering the first-order reflections¹. For this experiment, software displays the LOS power as -19.18 dBm; specular power of wall1 and blackboard reflections as -40.93 dBm and -34.09 dBm; total incoherent cluster power of wall1 and blackboard reflections as -38.06 dBm and

¹Note that we change the angle span from $[-180, 180]$ to $[0, 360]$.

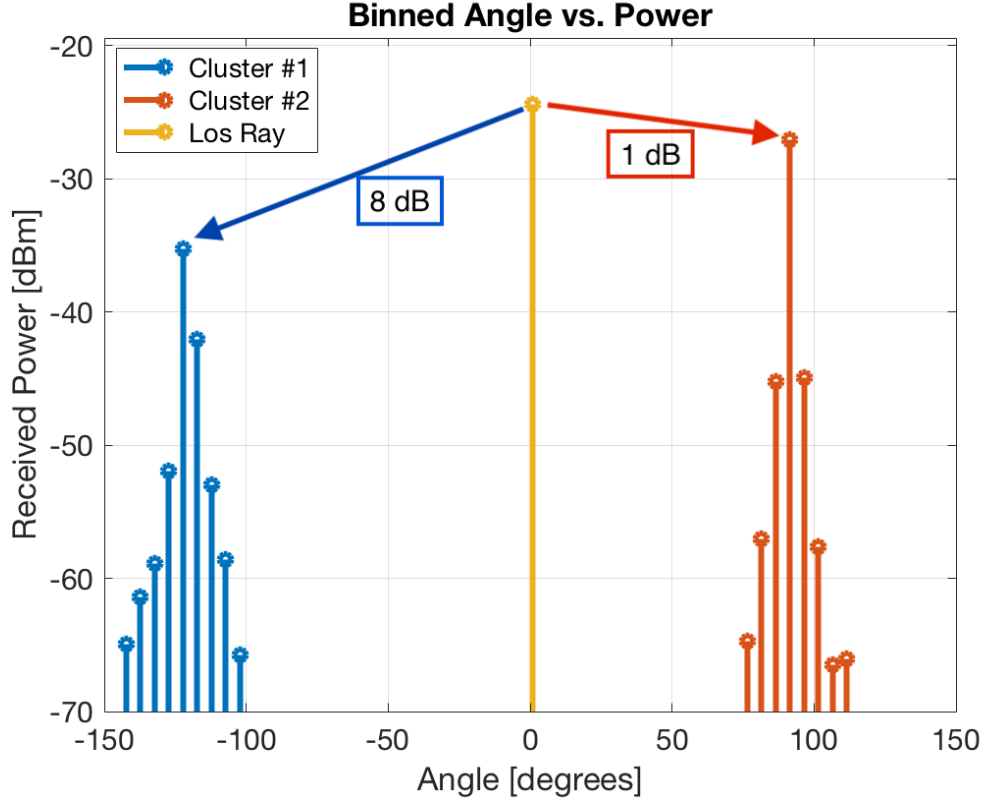


Figure 3.7: Binned Power Angle Profile of the channel when receiver is in the corner of the room.

−33.68 dBm, respectively. These match with the following RT-ICM results in the same order: LOS power is −18.95 dBm, specular powers are −42.93 dBm and −34.61 dBm and the total incoherent cluster powers are −37.9 dBm and −29.0 dBm. The comparison is visualized in Fig. 3.10 with the addition of the measurement results too. Here, we assume the peak cluster powers given in the measurements as the specular power. Finally, the total incoherent *channel* power in the software is estimated as −19.44 dBm while RT-ICM total incoherent *channel* power is −18.47 dBm. The software total coherent power is −18.51 dBm and the RT-ICM total coherent power is −17.11 dBm.

Receiver is on the Corner

The comparisons for AoA and power of the channel when the receiver is on the corner are given in Fig. 3.11 and 3.12. In this case, the total incoherent channel power is estimated as −23.93 dBm in the software whereas RT-ICM calculates it as −22.1 dBm.

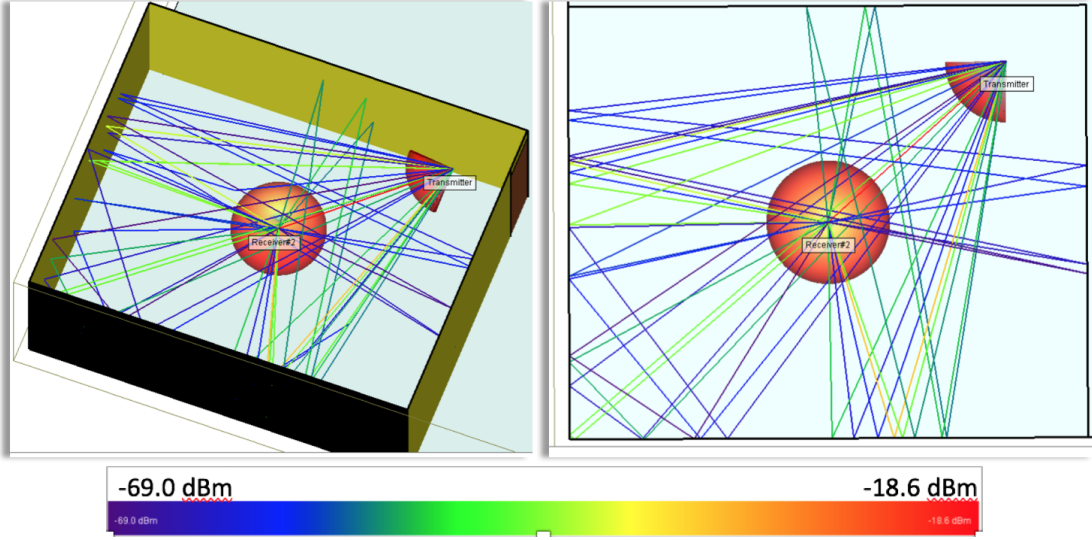


Figure 3.8: Visual representation of the channel paths that exceed -70 dB power threshold when receiver is at the center.

Their total coherent power is -22.25 and -19.54 , respectively. Although RT-ICM doesn't consider the higher order reflections and diffractions, total power is higher than the software estimations in both scenarios. This is mainly due to the RT-ICM's higher diffuse power estimations compared to the software. This can be seen from Fig. 3.10 and 3.12.

3.4.3 Comparison with IEEE 802.11ad/ay

Finally, we compare RT-ICM with the indoor intra-cluster model adopted by the WLAN mmWave standards, IEEE 802.11ad and IEEE 802.11ay. The model proposed in these standards is based on the measurements and ray-tracing. It models the intra-cluster power-angle distribution of indoor environments as Gaussian with a standard deviation of $\sigma = 5$ for conference rooms and office cubicles, $\sigma = 10$ for living rooms. In our application here, the dimensions of the room is somewhere between the living room and the office cubicle. Hence, we expect a gaussian distribution with a standard deviation between 5 and 10.

In RT-ICM, the diffuse scattering loss is modeled with a raised-cosine function which results in a *Gaussian-like* received power spectrum in the spatial domain in the linear

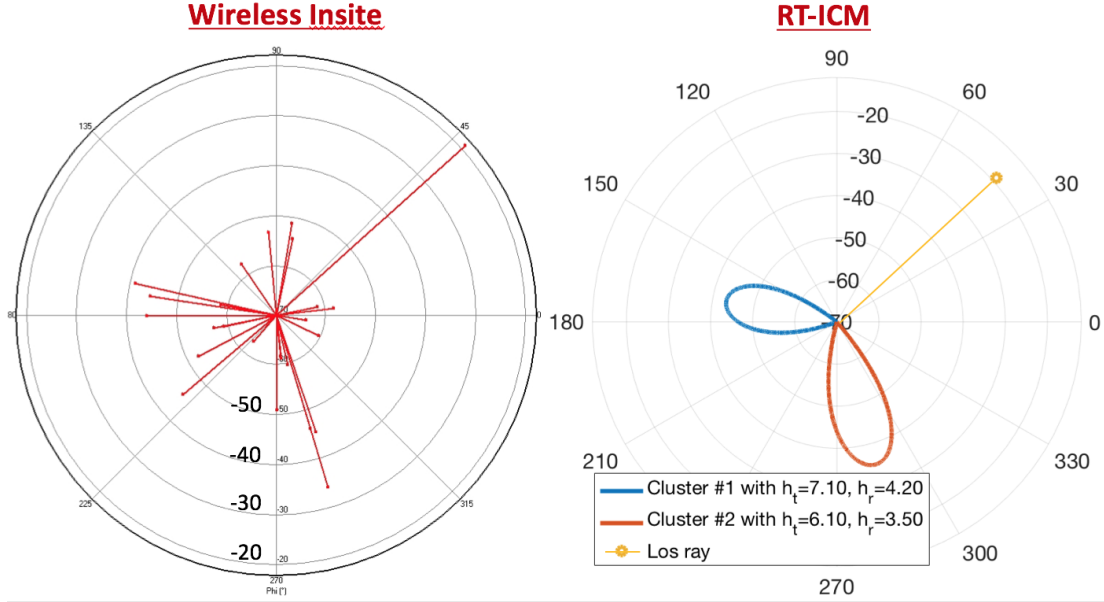


Figure 3.9: Channel AoA comparison of the software and RT-ICM when receiver is at the center.

scale. Hence, we seek to fit a Gaussian function to the power angle profile output of RT-ICM. The Gaussian function is of the form $g(\phi) = ue^{(\phi-x)^2/v^2}$ where the parameters u , v and x control the peak, the width and the mean of the function, respectively. We select these parameters such that the resultant function fits best to the data. An algorithm is proposed for Gaussian fitting in [61].

As an example, for the scenario where the receiver is at the center, blackboard cluster power angle profile is plotted in linear scale in Fig. 3.13 along with its fitted Gaussian as well as IEEE 802.11ad channel model. Here, the standard deviation of the fitted Gaussian is $\sigma_{RT} = v/\sqrt{2} = 6.81^\circ$ and compared with $\sigma = 5^\circ$ WLAN model. For wall1 cluster, we find out that $\sigma_{RT} = 4.24^\circ$. When the receiver is on the corner, the standard deviation for blackboard and wall1 becomes $\sigma_{RT} = 8.28^\circ$ and $\sigma_{RT} = 5.73^\circ$, respectively, which are in a good agreement with the measurement-based mmWave WLAN standard intra-cluster model.

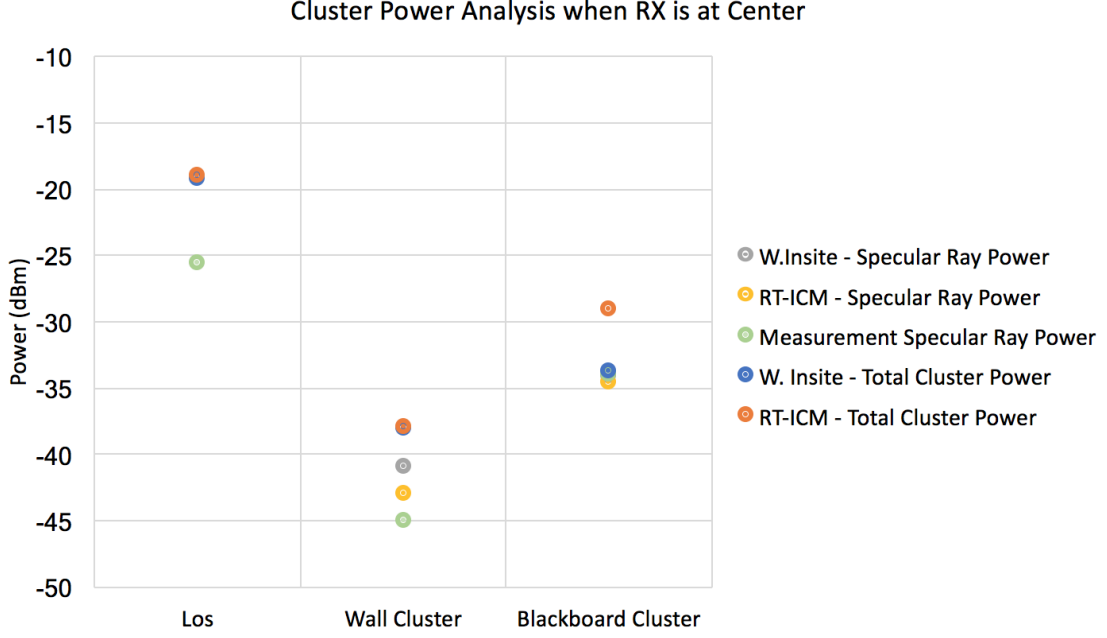


Figure 3.10: Power Comparison when receiver is at the center.

3.5 Conclusion

In this chapter, we validate our novel ray-tracing based mmWave intra-cluster model, RT-ICM, by implementing it into a published classroom measurements at 60 GHz. We provide cluster power expressions for RT-ICM. Then, we replicate the measurements with a 3-D ray tracing full scan software and perform a deeper comparison with RT-ICM results. Finally, we compare the results with the measurement based intra-cluster model introduced in mmWave WLAN standards. We show that the proposed simple mmWave intra-cluster model estimates the angular spectrum with high accuracy.

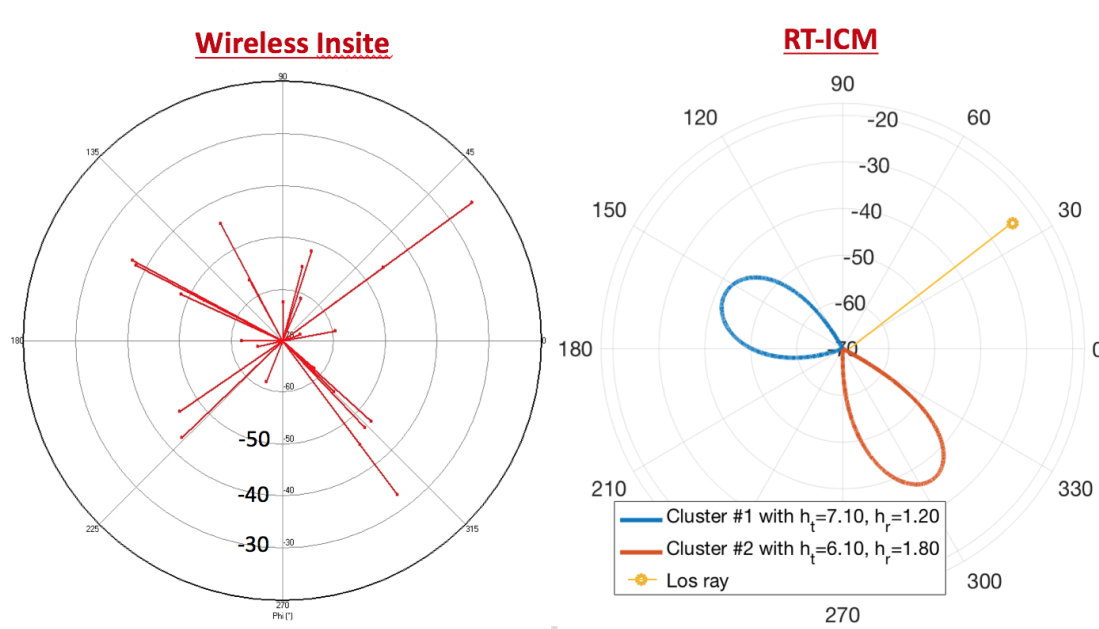


Figure 3.11: Channel AoA comparison of the software and RT-ICM when receiver is at the corner.

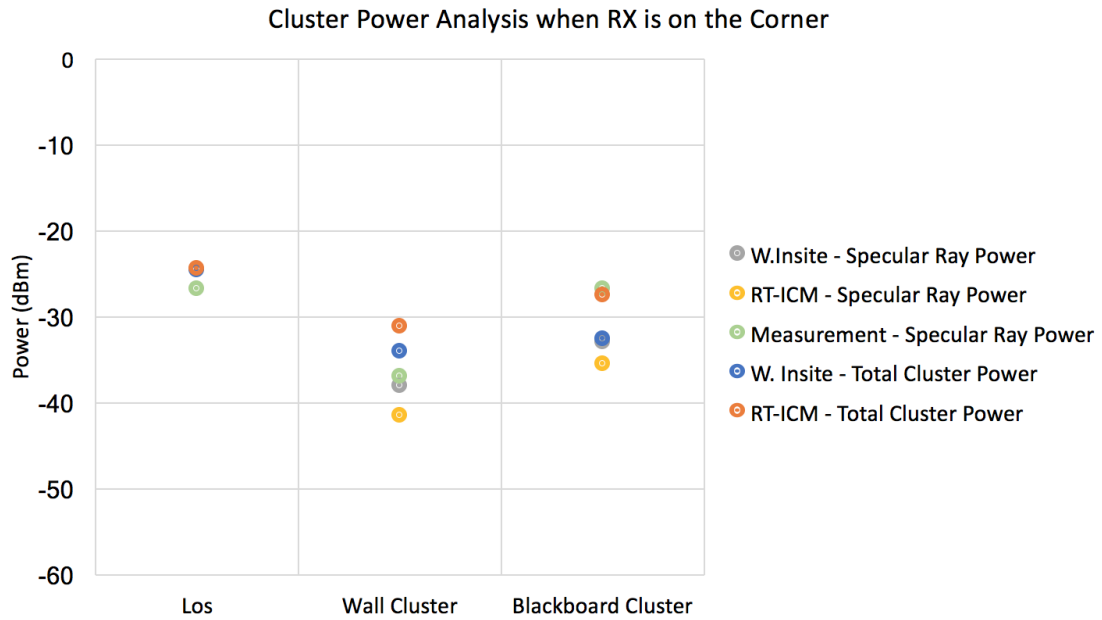


Figure 3.12: Power Comparison when receiver is at the corner.

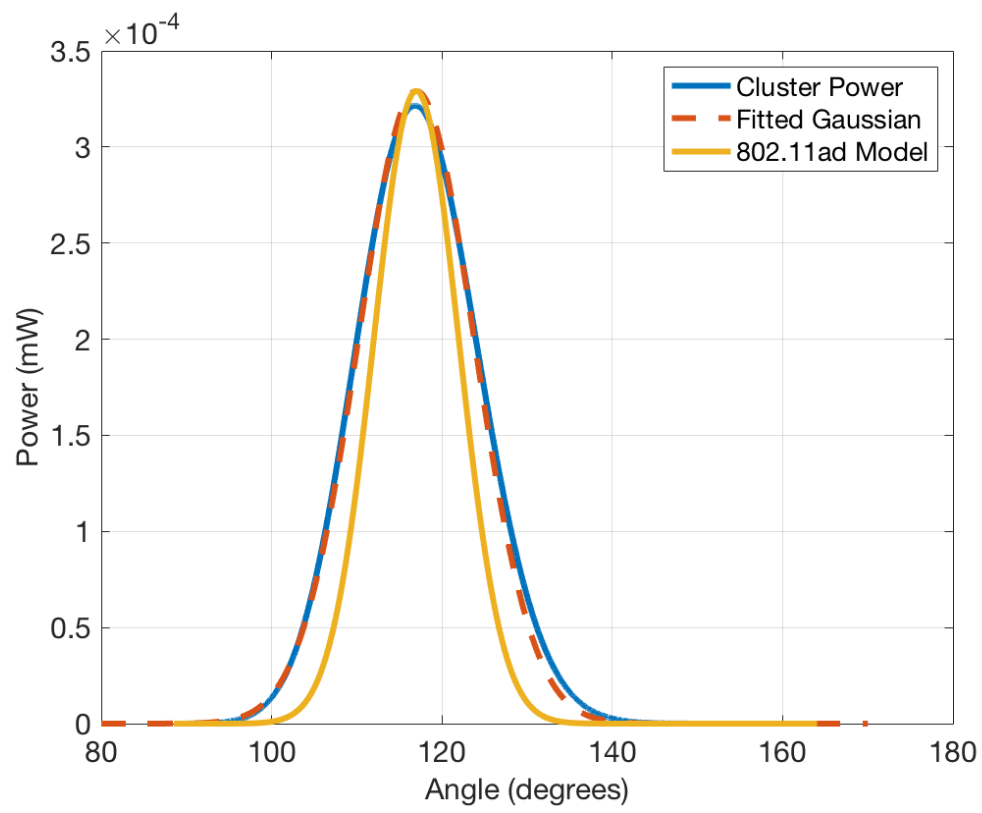


Figure 3.13: PAP comparison with IEEE 802.11ad/ay for the blackboard reflection when the receiver is at the center

Chapter 4

Extension of RT-ICM - Blockage Support

Due to the sparsity and site-specific nature of mm-wave channels, statistical channel models can easily deviate from a particular real world scenario. On the other hand, to overcome high path loss, high gain beams steered toward clusters are employed. To increase the spatial filtering efficiency due to beamforming, we model the intra-cluster behavior of mm-wave channels in the previous chapters with ray tracing by considering scattering and first-order reflections only. In this chapter, a hybrid model is presented which is an advancement of the said ray tracing based intra-cluster model (RT-ICM) by incorporating a probabilistic blockage model. This addresses the effects of an environmental object within the angular range of the cluster on the received power angular profile. We show that an additional cluster can emerge in the receiver power angle profile due to the reflection and scattering from the object's surface, subject to its location. While we address the blockage attenuation using the statistical blockage model, the additional cluster is modeled as a geometric update to the RT-ICM. To demonstrate this, we provide an IEEE 802.11ad indoor conference room based case study implementation of the model. The results show that an environmental object can significantly affect the received power depending on its location. Further, it is observed that the contribution to the received power by the object may exceed the loss it causes.

4.1 Introduction

Characterization of mm-wave channels are substantially different than that of the microwave channels as the propagation impairment mechanisms effect the mm-wave channels differently [9]. Due to the high path loss at mm-wave frequencies, diffraction contribution is negligible [34]. On the other hand, diffuse scattering is seen as a non-negligible effect as typical materials becomes rough at mm-waves [25, 26]. To combat the severe attenuation, beamforming is utilized, this however makes the communication link more sensitive to shadowing due to environmental objects. Specifically, blockage effect at 60 GHz for the indoor communications is of interest in the recent years.

In IEEE 802.11ad [71], a dynamic human blockage model at 60 GHz for indoor applications is proposed using the combination of ray tracing, random walk and a diffraction model. Detailed analyses to improve the IEEE 802.11ad standardization are published by employing different diffraction models [43], investigating presence of multiple blockages [44] and their shapes [45]. A deeper temporal attenuation due to human body is analyzed with several type of measurements in [46] and reported -18 dB to -36 dB attenuation range. [47] studies the best shape using phantoms that replicates the similar blockage results of a human body via measurements. Finally, authors in [60] conduct measurements and discuss the optimal beamwidth in case of the beam is blocked. While the mentioned works focus on the blockage attenuation, however, none of them addresses the blockage *contribution* due to the reflective surface of the human body.

In Chap. 2, we introduced an intra-cluster model, RT-ICM, for stationary mm-wave channels based on ray tracing which also takes the diffuse scattering into account. It outputs the power angle profile (PAP) and power delay profile (PDP) of the cluster. We further provided a MIMO channel model that consists of nonoverlapping clusters. The novelty of the proposed model is that it gives the angular and temporal characteristics of the mm-wave cluster with an extremely simplified geometry-based approach. It can be used for indoor and outdoor environments such as living, conference and office rooms, rural areas, etc. However, the model is applicable to only stationary channels where

neither the communicating devices nor the objects within the channel move.

In addition to a greater path loss, another issue concerning mm-wave propagation is the *blockage* phenomenon. This is owing to the susceptibility of mm-waves to penetration losses due to commonly found environmental objects such as vehicles, humans, and foliage [26]. For example, clear glass in an indoor environment can result in upto 3 dB/cm loss at 28 GHz [48]. Nevertheless, objects composed of lossy dielectric materials essentially absorb, propagate, and reflect the energy incident on their surface [25]. These reflections can also contribute to the NLOS received signal. It is clear that evaluating and understanding this interaction is crucial to the algorithm design of mm-wave systems.

To accomplish this, in this work, we employ a blockage model detailed in [49] to RT-ICM that provides a soft metric for the signal attenuation in the presence of blockages. After embedding the statistical blockage loss to the geometry-based RT-ICM, we provide the effect of a blocker as another first-order reflector in the environment by introducing the basic geometry update. In the implementation section, we give a case study of a typical IEEE 802.11ad indoor conference room and show with numerical results that a blocker can significantly change the received power depending on its location, proving the site-specific nature of mm-wave channels. Furthermore, we show that if the blocker object has higher reflectivity than the main reflector in the cluster, the reflected energy from the object can even tolerate the loss that it caused in some cases.

This chapter is organized as follows. A summary of the techniques used to model the behavior of a blocking object in the assumed indoor setting is provided in Section 4.2. The impact of the blocker location on the received power is assessed using ray tracing simulations for an IEEE 802.11ad based setup in Section 4.4. Section 4.5 concludes the description of this work.

4.2 Background

The impact of surrounding objects in the vicinity of the receiver for an indoor environment is evaluated using two component models which are summarized in this section.

4.2.1 Ray Tracing Intra-Cluster Model (RT-ICM)

In the previous chapters, we introduce a mm-wave intra-cluster model based on ray tracing (RT-ICM) that takes only first-order reflections into account. In these chapters, we calculate the total power at the front of the receiver antenna and after the receiver processing, i.e. after resolution is applied. In this chapter, however, we only calculate and compare the former. Let $P_{T,C}$, the *total coherent power*, denote the coherently-calculated total cluster power at the receiver antenna and let $P_{T,I}$, the *total incoherent power*, denote the incoherently-calculated total cluster power at the receiver antenna. Then,

$$P_{T,C} = (a_s)^2 + \frac{S_\Omega}{N_r} \sum_{k=0}^{N_r-1} (a_k)^2 \quad (4.1)$$

$$P_{T,I} = (a_s)^2 e^{j\varphi_s} + \frac{S_\Omega}{N_r} \sum_{k=0}^{N_r-1} (a_k)^2 e^{j\varphi_k} \quad (4.2)$$

Note that the coherent power is obtained if the receiver has the ability of resolving all the rays. On the other hand, the incoherent incident power is what an omnidirectional antenna would receive. In fact, a beam that covers the supported angle spread (SAS), $S_\Omega = \alpha_{N_r-1} - \alpha_0$, would have the same incoherent power. In the equations, S_Ω/N_r term is inserted for the integral approximation.

4.2.2 Blockage Model

To model blockages in the indoor office scenario considered in this work, we assume that the blockers are randomly placed around the receiver. Owing to this nature of the blocker presence, we can leverage the result in [49] by adapting it to an indoor setting. This model is summarized as follows. Fig. 4.1 shows the azimuth plane geometry of the environment for which the attenuation due to blockages is modeled. A mm-wave link

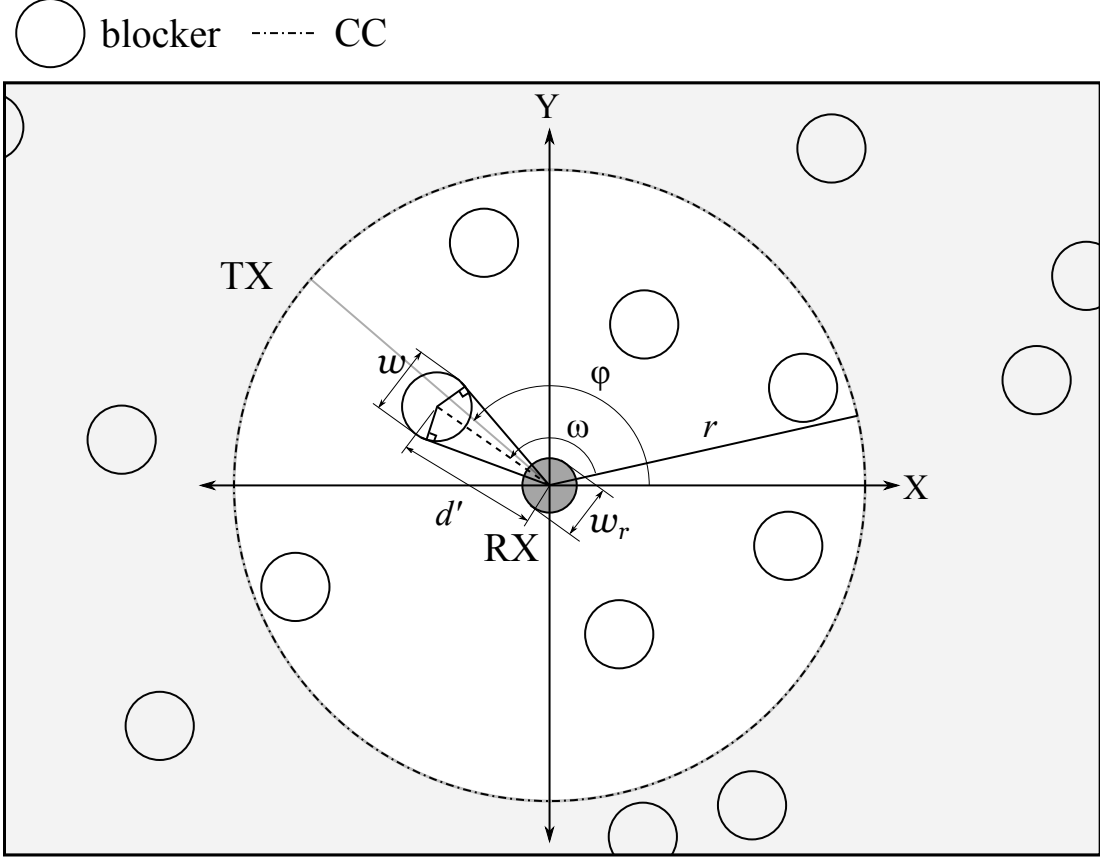


Figure 4.1: Azimuth plane geometry of the assumed scenario used to model the attenuation due to blockages.

comprising of a transmitter (TX) and a receiver (RX) is considered. To measure the impact of blockages we consider only those objects in the environment that can block the received signal in any direction. Such objects are termed as *blockers*.

Assumption 1. The size of the geometry under consideration is defined by the communication range of the receiver. This can be expressed by a circle of radius r referred to as the communication circle (CC). As shown in Fig. 4.1, the receiver is at the center of the CC and the transmitter at its edge.

Note that once the receiver is blocked in an arbitrary direction, it is assumed that it is fully blocked in the zenith. Blockers are modeled as cylinders of diameter w . Let w_r denote the diameter of the cylindrical receiver and $s \geq \frac{w+w_r}{2}$ denote the distance of the nearest blocker from the receiver. The location of a blocker is defined by the polar coordinates $(d', \omega) \in [s, r] \times (0, 2\pi]$. Blockers are placed around the receiver as per

$$g(r) = \frac{w^2}{8\pi(r^2 - s^2)} \left[\frac{2 \arcsin(w/2r)}{(w/2r)^2} + 2 \left(\frac{1}{(w/2r)^2} - 1 \right)^{1/2} - \frac{2 \arcsin(w/2s)}{(w/2s)^2} - 2 \left(\frac{1}{(w/2s)^2} - 1 \right)^{1/2} \right]. \quad (4.3)$$

a two-dimensional homogeneous Poisson point process (PPP) [50], [51]. Whereas the blocker population is modeled with the intensity of the PPP ρ which is the expected number of blockers per unit area. Thus, the average number of blockers within the CC is $\bar{\rho}(r) = \rho \times \pi r^2$. Then the attenuation $A(r)$ of the received signal along an arbitrary direction ϕ is given by the theorem from [49] stated below.

Theorem 1 (Expected Attenuation). *Let the receiver be placed at the center of the CC of radius r . Let cylindrical blockers of diameter w be placed around the receiver according to a two-dimensional homogeneous PPP with a sufficiently large intensity ρ . Then, the expected attenuation of a received signal arriving from the direction $\phi \in (0, 2\pi]$ is given as*

$$\bar{A}(r) \approx e^{-\bar{\rho}(r)(1-e^{-g(r)(1-\zeta)})}$$

where, $\bar{\rho}(r) = \rho \times \pi r^2$ is the expected number of blockers inside the CC, ζ is the penetration loss due to a blocker, and $g(r)$ is the probability of a blocker causing a cover in the direction ϕ .

Note that, $g(r)$ given by (4.3). The above result is validated by means of a 10^5 Monte Carlo simulation per ρ value. The average attenuation for various geometry sizes (r) per blocker density is shown in Fig. 4.2. It is observed that the theoretical approximation closely follows the simulation. As expected, the attenuation worsens as the blocker population increases.

4.3 Blockage Model Support to RT-ICM

To assess the effect of surrounding objects on the received power, we assume the setup shown in Fig. 4.3. Here, a general geometry for an indoor environment that describes

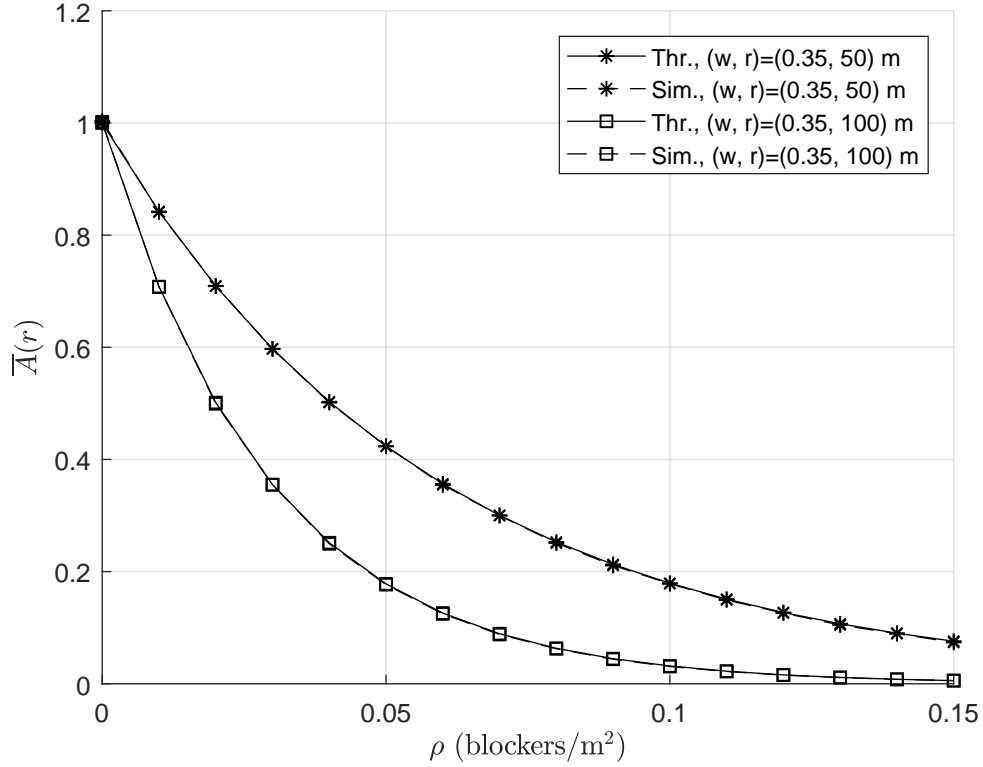


Figure 4.2: Comparison of the theoretical and simulated attenuation for various geometry sizes with $\zeta = -20$ dB.

the mode of blockage attenuation and reflection due to the object is depicted. Based on the location of the object in question, the space is divided into two regions. The region where the energy reflected (first-order reflection) from the object cannot be received is termed as region B. Whereas, in region A, the reflected energy from the blocker can reach the receiver. Note that, we do not consider the contribution by means of diffraction around the object. The attenuation due to blockage is solely due to the penetration loss caused by the object. Considering this assumption, our model is approximative in nature.

In particular, when an object is present in region B, we assume that the only effect to the cluster is additional loss due to the blockage. However, if an object falls into region A, two channel mechanisms affect the cluster: (1) attenuation due to blockage, (2) gain due to reflection from the object. Attenuation loss is estimated with the given model in subsection 4.2.2. On the other hand, the gain due to the reflection is modeled

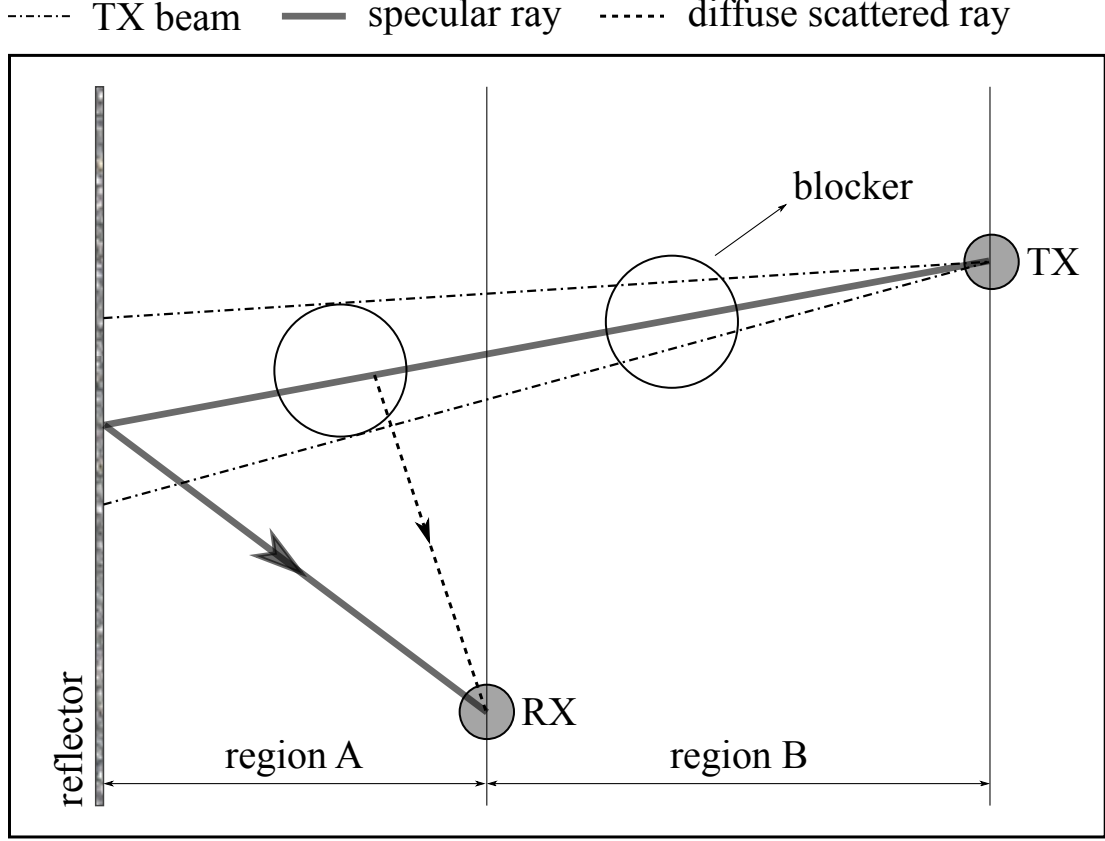


Figure 4.3: Schematic contrasting the effect an environmental object at two different locations. The location (and the subsequent impact) of the object divides the space under consideration into two regions. The region where reflection (along with blockage) to the receiver occurs is termed as Region A whereas the one where only blockage occurs is termed as Region B.

as an update to BGM of RT-ICM. The schematic of the updated model is given in Fig. 4.4 where the model parameters are self-explanatory. Here, we assume that the blocker sits (and slides) on the specular ray of the main cluster and blocks the entire cluster. Note that we implicitly assume that the blocker is always on the incident ray. However, if it is present on the reflected ray, there doesn't exist reflections reach to the receiver and hence the scenario will be assumed as the blocker is in region B. While the blocker slides along the specular ray, d_h takes values depending on the geometry of the link. If $h_t > h_r$, as shown in Fig. 4.4, $d_h = [0, h_r]$, otherwise $d_h = [0, h_t]$. With the given assumptions, RT-ICM algorithm directly applicable such that each ray hits to a unique point on the blocker and reaches to the receiver; thereby creating a new SAS, hence a new cluster. Respectively, we call them *blocker SAS* and *blocker cluster*,

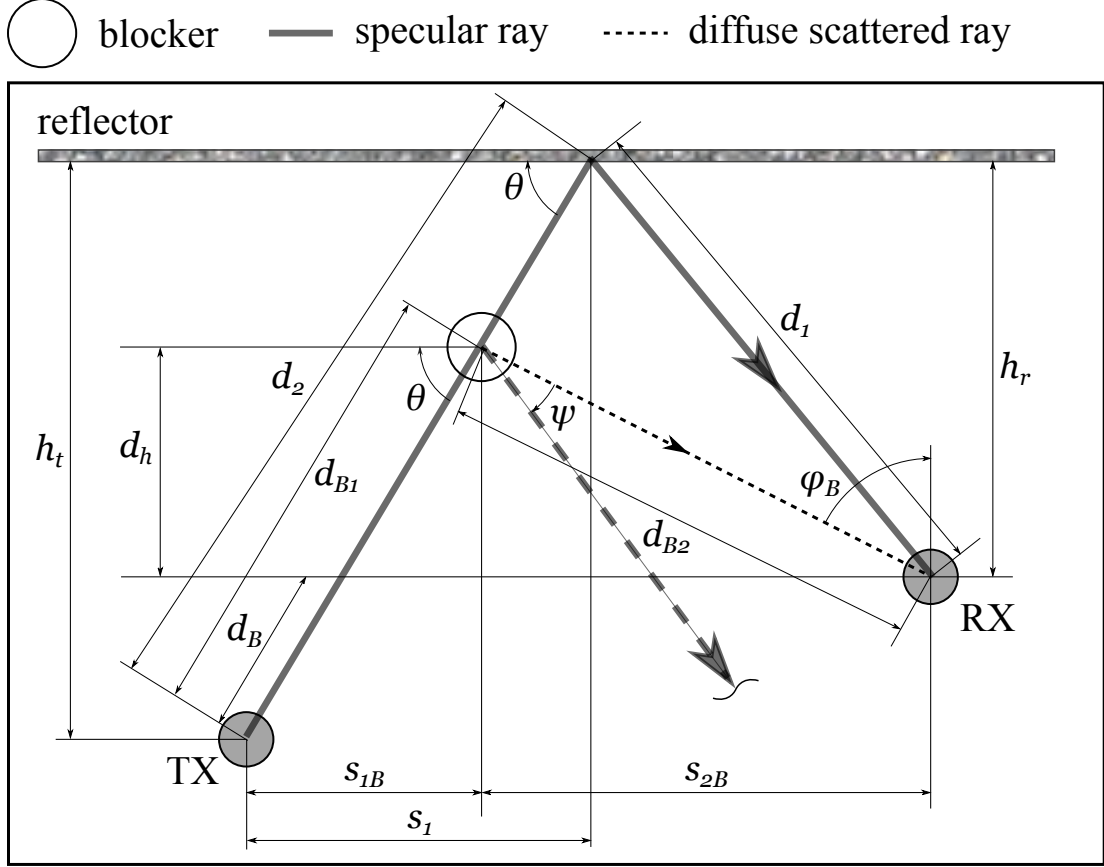


Figure 4.4: Blockage model update of BGM given in RT-ICM when the object is in region A.

hereinafter. In Fig. 4.4, only the diffuse component of the specular ray is shown as well as its specularly reflected component. Scanning the blocker SAS, power angle profile for blocker cluster is generated.

While blocker approaches to the main reflector, there is a *critical point* for d_h where the blocker cluster PAP overlaps with the main cluster PAP. Before the blocker reach to critical point, to obtain the total incoherent power, we calculate the each cluster incoherent power, separately. In this scenario, the reference phases for the clusters are the first ray within the clusters arrives the receiver. After finding two incoherent power values for each clusters, we simply sum them coherently as the receiver is assumed to resolve them. However, if the blocker exceeds the critical point, then the cluster PAPs overlap and the total incoherent power is calculated by treating the obtained PAP as a single cluster. In this case, reference phase for all rays is the specular ray of the main

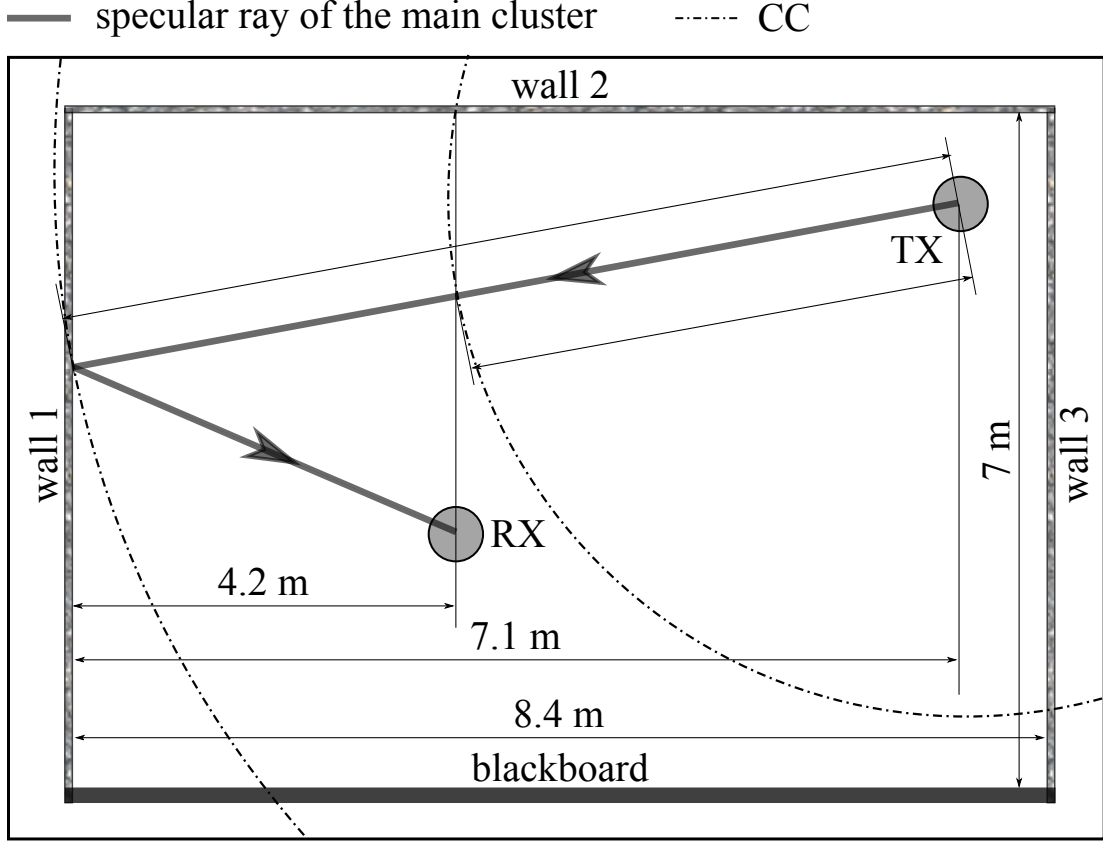


Figure 4.5: An IEEE 802.11ad based indoor office scenario with a transmitter and receiver pair. The CC boundaries are shown to indicate how the attenuation due to blockage is calculated (Section 4.2.2).

cluster. In the next section, we implement the given model to a case study.

4.4 Case Study: An IEEE 802.11ad based Indoor Conference Room

An object composed of lossy dielectric material can take away as well as contribute to the received power depending on its location in the indoor environment described in the previous section. In this section we provide a case study to demonstrate this using ray tracing simulations.

4.4.1 Setup

For our experiment we assume an indoor office environment such as the one specified in the IEEE 802.11ad standard [10]. An instance of this environment is illustrated in Fig. 4.5. To assess the attenuation due to a blockage caused by an object along the

Table 4.1: Input Parameters of the Simulation (d , h_t , h_r [meters], σ_h [mm]) P_T [dBm], G_T , G_R [dB], P: polarization, V:vertical, H: horizontal)

Cluster Parameters (P)	d	h_t	h_r	ε_r	σ_h	P_T	G_T	G_R
Main Cluster (H)	3.8	7.1	4.2	2.9	0.3	25	6.7	29
Blockage Cluster (H)	3.8	d_{B1}	d_{B2}	5	0.5	25	6.7	29
Blockage Parameters	w [m]	s [m]	r [m]	d' [m]	ζ			
Human Body	0.25	0.12	d_2	d_B	0.1			

specular path, CC boundaries are shown. Note that, each region (A and B) as depicted in the general model (Fig. 4.3) has a CC in it. For this setup, we use the parameters shown in Table 4.1.

4.4.2 Numerical Results

Before we present the results for the case study (Fig. 4.5) we perform ray tracing simulation to assess the power contribution by a blocker as a function of its location from the reflecting surface. This is as per the setup shown in Fig. 4.3. The contribution to the received power due to reflection from the blocking object (in region A in Fig. 4.5) is shown in Fig. 4.6. As expected, coherent power contribution (eq. 4.1) is higher than the incoherent contribution (eq. 4.2). Also, the rayleigh fading is noticeable due to the multipath for very short displacements. The contribution of power due to a blockage as a function of the angle of arrival is shown in Fig. 4.7. Note that, the central angle of the main cluster corresponds to the blocker situated at the reflector surface i.e. when the blocker is at wall 1 in Fig. 4.5. It is observed that, an arbitrary blocker situated closer to the reflector contributes more to the received power than that situated far from it.

Finally, the total received power as a function of the blocker location from the reflector is shown in Fig. 4.8. Note that, this is for the parameters depicted in Fig. 4.5. It is observed that, in the case of both incoherently and coherently received power, the attenuation due to blockages causes a loss of over 4 dB. The results clearly show that a distance threshold exists beyond which the blocking object begins to contribute to the received power owing to its reflective properties. In fact, the Rayleigh fading power exceeds the power contribution without a blockage when the blocker is situated closer

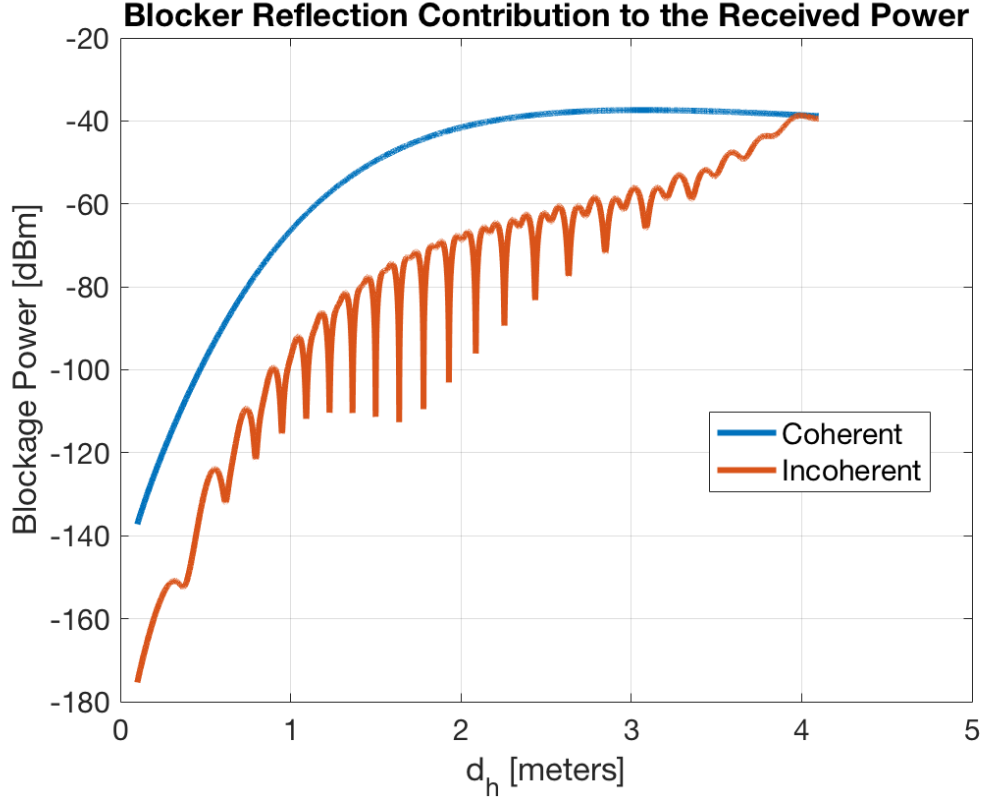


Figure 4.6: Received power contribution by means of reflection due to the blocking object as a function of the location of the object with respect to the reflector surface.

to the reflector, i.e. d_h is larger.

4.5 Conclusion and Discussion

In this chapter, we improve our ray tracing based intra-cluster model (RT-ICM) that takes the diffuse scattering into account by employing a hybrid (geometrical & probabilistic) blockage model to address the effects of an object within the spatial footprint of the cluster. We show that depending on the location of the blocker, an additional cluster can emerge at the receiver power angle profile due to the reflection and scattering from the blocker surface. While we address the blockage attenuation using the statistical blockage model, the additional cluster is modeled as a geometric update to RT-ICM. In the implementation, we give a case study of a typical IEEE 802.11ad indoor conference room and show with numerical results that a blocker can significantly change the received power depending on its location, due to the site-specific nature of

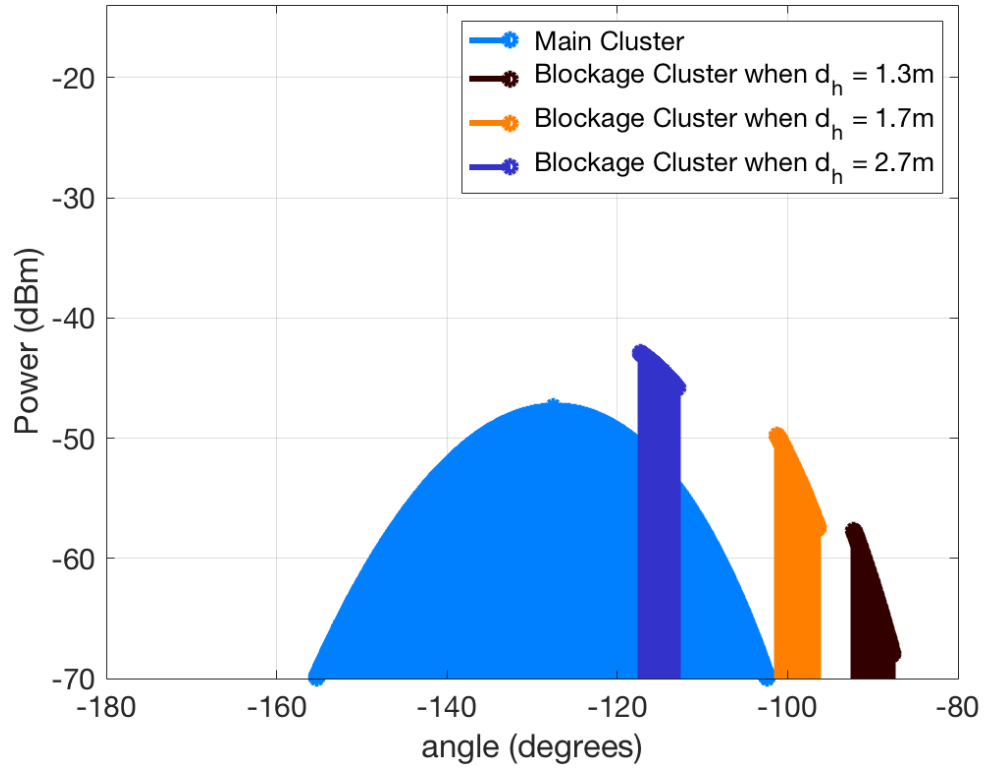


Figure 4.7: The PAP as a result of attenuation and reflection contribution due to the blocking object.

mm-wave channels. Further, it is shown that the blockage contribution to the received power even can exceed the blockage loss, in some cases. Results in this chapter shows that the blockages impact the indoor mm-wave communications, critically.

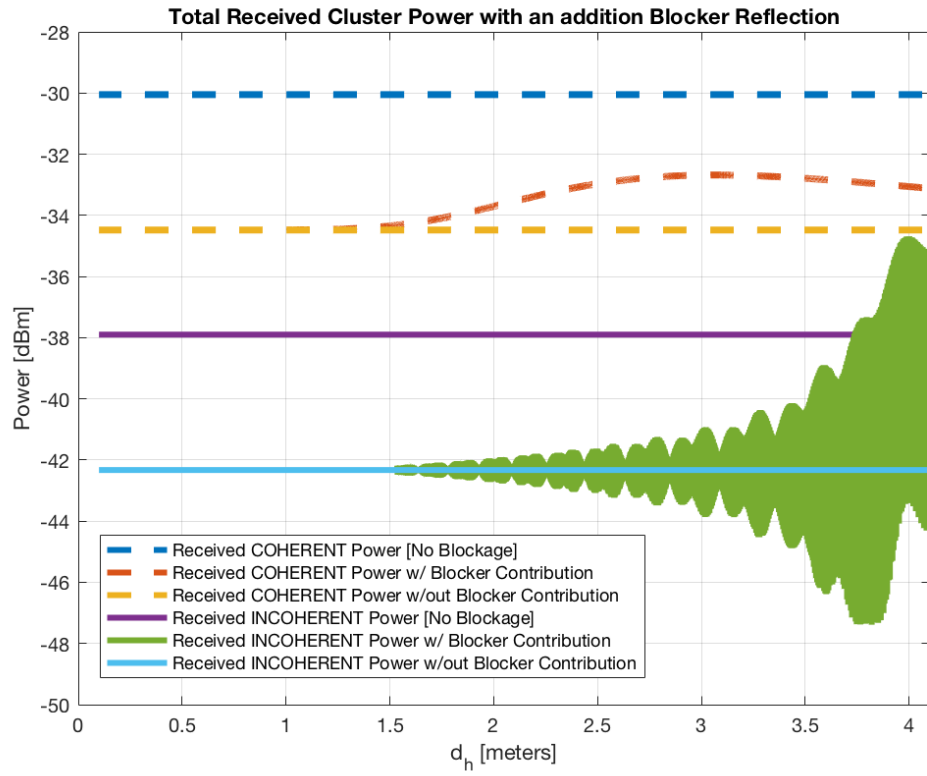


Figure 4.8: Total received power as a function of the location of the object (distance d_h) with respect to the reflector surface i.e. wall 1 in Fig. 4.5.

Part II

Beamwidth Optimization

Chapter 5

Analytical Framework of Optimum Beamwidth Selection

Beamforming for millimeter-wave (mmWave) communications is well-studied in the physical layer (PHY) based on the channel parameters to develop optimum receiver processing techniques. However, even before signal processing, antenna structure and radiation parameters affect the beamforming performance primarily. For example, in contrast to common belief, narrow beamwidth may result in degraded beamforming performance. In order to address the impairments such as beam misalignments, outage loss, tracking inability, blockage, etc., an optimum value of the beamwidth must be determined. In this chapter, assuming a communication system that creates a beam per cluster, we theoretically investigate the beamwidth and received power relation in the cluster level mmWave channels. We adopt uniform linear array (ULA) antenna structure and formulate its antenna gain with respect to the beamwidth. Two beam models are considered for the main lobe of the array pattern, rectangular and triangular, to approximate the best and worst scenarios, respectively. For the channel, we derive beamwidth-dependent extracted power expressions for two intra-cluster channel models, IEEE 802.11ad and our previous work based on ray-tracing (RT-ICM). Combining antenna and channel gains, in case of a beam misalignment, we find that the optimum beamwidth that maximizes the received power is larger than the alignment error when the error itself is larger than the standard deviation of the cluster power-angle spectrum. Once the alignment error is smaller than the standard deviation, we confirm that the optimum beamwidth converges zero. Performing asymptotic analysis of the received power, we give the formulation and insights that the practical nonzero beamwidth values can be achieved although sacrificing subtle from the maximum received power. Our analysis shows that to reach 95% of the maximum power for an indoor mmWave

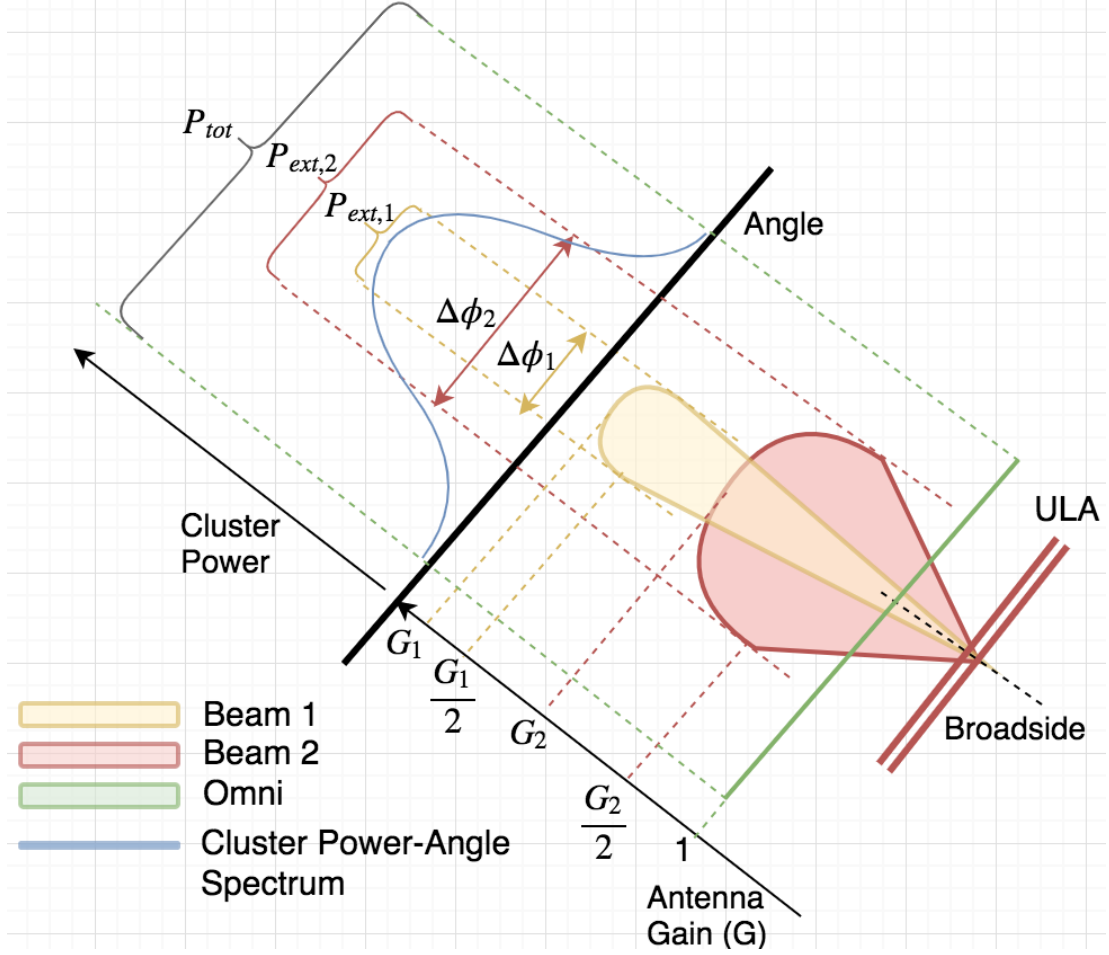


Figure 5.1: Visualization of the optimum beamwidth problem at the receiver

cluster, a practical beamwidth of $7^\circ - 10^\circ$ is enough, which can be created with 18 – 20 antenna elements. In the simulation section, we show that the expressions given by the analysis match to the simulated results.

5.1 System and Channel Model

The optimum beamwidth problem has two sides; while decreasing beamwidth and increasing directivity of an array beam, (1) antenna gain increases, (2) captured energy from the cluster channel decreases. Hence, received power on the antenna terminals directly depends on the beamwidth.

Received power on the antenna terminals is given in [27] as

$$P_R = \mathcal{P}_{inc} \frac{G\lambda^2}{4\pi} \quad (5.1)$$

where \mathcal{P}_{inc} is the power density per *area* front of the antenna; G is the receiver antenna gain at maximum direction and λ is the wavelength. Note that when an omnidirectional antenna is employed at the receiver, whose gain is 1 at all directions, received power equals the available total cluster power. Then, the available power in front of the antenna can be given as

$$P_{tot} = \mathcal{P}_{inc} \frac{\lambda^2}{4\pi} \quad (5.2)$$

Let $P_{ext} \leq P_{tot}$ is the extracted power from the cluster by a directional antenna. The equality holds whenever the beamwidth of the antenna covers entire cluster spatially¹. Then, the received power given in Eq. (5.1) can be represented as a function of half-power beamwidth ($\Delta\phi$) and can be updated as

$$P_R(\Delta\phi) = G(\Delta\phi)P_{ext}(\Delta\phi) \quad (5.3)$$

In Fig. 5.1, an example diagram of the discussion is illustrated with a comparison of two beams created by a ULA and steered towards a cluster AoA.

Analysis of the problem requires the knowledge of spatial representation of the intra-cluster channel. However, while phased array antennas are well-studied in the literature and allow us to derive antenna gain-beamwidth relation, on the other hand, intra-cluster angular behavior of the mmWave channels is still not understood very well. In 3GPP channel model [6], angular distribution of cluster power is simply modeled with a fixed number of rays with equal power levels. In 60 GHz WLAN standards IEEE 802.11ad [10] and IEEE 802.11ay [11], a more intuitive model is adopted based on the measurements such that the power angular spectrum is distributed normally with $N(0, \sigma)$ where $\sigma = 5$ for conference room and cubicle environments and $\sigma = 10$ for living room channel models. Considering the site-specific nature of the mmWave channels, these models are likely to fail for different type of environments.

In the previous part, we introduce a mmWave intra-cluster model based on ray-tracing (RT-ICM) that takes only first-order reflections into account. It outputs the

¹In this dissertation, we assume antenna beam models whose gain is 0 outside the beamwidth. That structure is discussed in Sec. 5.2.

power distribution both in angle and time domain within the cluster and can be used for both indoor and outdoor mmWave systems in any type of stationary environments. Basic Geometric Model (BGM) part of the model takes first-order reflection cluster environment parameters as inputs and generates the supported angle spread (SAS), $S_\Omega = \alpha_{N_r-1} - \alpha_0$, at the receiver. Then, running the BGM for each infinitely large number of rays that are within the supported angle spread; angle, time, power and phase of the rays are calculated; thereby generating the theoretical cluster impulse response. The output theoretical baseband cluster impulse response (TC-CIR) is given in Eq. (2.7) as

$$c(t, \omega) = a_s e^{j\varphi_s} \delta(t - t_s) \delta(\omega - \Omega_s) + \sum_{k=0}^{N_r-1} a_k e^{j\varphi_k} \delta(t - t_s - \tau_k) \delta(\omega - \Omega_s - \alpha_k) \quad (5.4)$$

where, t and ω are the reference ToA and AoA variables; a_s , φ_s , t_s , and Ω_s are the amplitude, phase, ToA and the AoA of the specular ray; a_k , φ_k , τ_k , α_k are amplitude, phase, delay, offset AoA of the k -th ray, respectively. $\delta(\cdot)$ is Dirac delta function and N_r is the number of diffuse rays.

Finally, the theoretical impulse response is binned in the angle and time domain according to the bandwidth and angle resolution of the communication system. Basically, the binned version is the impulse response that the receiver *sees*. Note that, since we are interested in estimating the received power at the antenna terminals in this chapter, i.e. before receiver signal processing, we will use the theoretical impulse response given in Eq. (2.7) as the cluster power angle profile. Then, the total power in the cluster is given as

$$P_{tot} = a_s^2 + \frac{S_\Omega}{N_r} \sum_{k=0}^{N_r} a_k^2 \quad (5.5)$$

where S_Ω/N_r term is inserted for the integral approximation.

5.2 Antenna Structure and Gain

As Eq. (5.3) suggests, antenna gain is the counterpart of the captured cluster power in the equation for a certain beamwidth. Finding an expression for antenna gain as a function beamwidth for an arbitrary array design is not easy and out-of-scope of

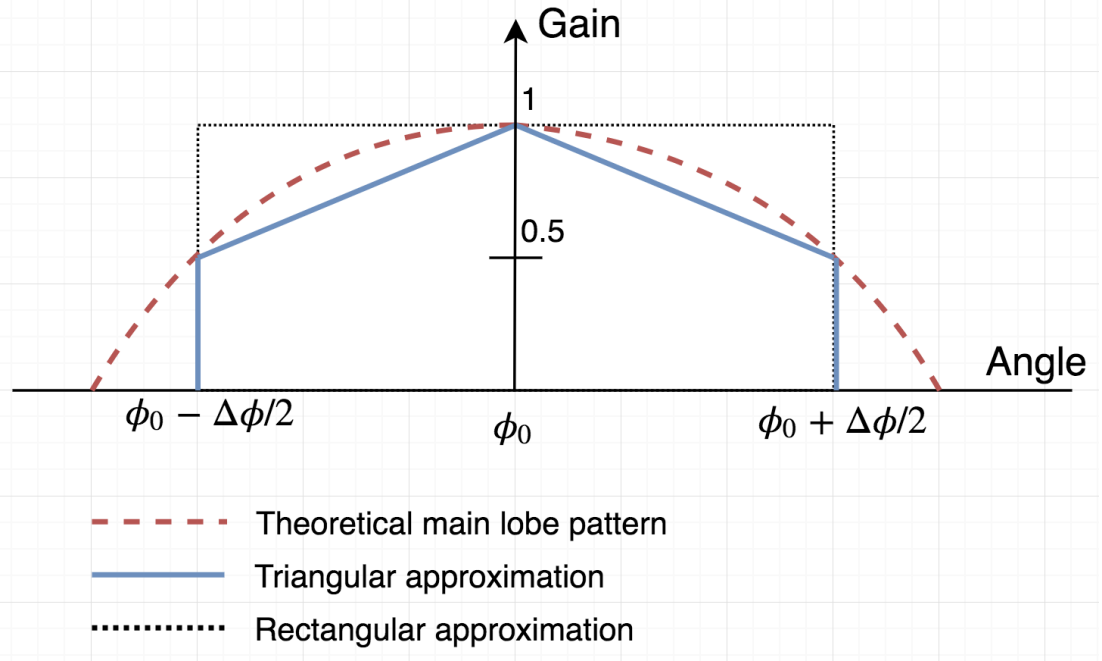


Figure 5.2: Antenna pattern models considered in the chapter.

the dissertation. Instead, we adopt the well-known uniform linear array (ULA) design where the spacings between the elements are equal and we seek to find the relationships between antenna gain, beamwidth, number of elements and scan angle for a ULA.

5.2.1 Beam Pattern Model

In our study, we use two models for the beam pattern; a rectangular window and a triangular window, both are seen in Fig. 5.2 for a steering (scan) angle of ϕ_0 . Both approximations ignore the sidelobes; thereby modeling only the main lobe. Expressions of the shown functions for rectangular and triangular model, respectively, are,

$$W_R = \begin{cases} 1, & \phi_0 - \Delta\phi/2 > \phi > \phi_0 + \Delta\phi/2 \\ 0, & \text{otherwise} \end{cases} \quad (5.6)$$

$$W_T = \begin{cases} 1 - \frac{|\phi - \phi_0|}{\Delta\phi}, & \phi_0 - \Delta\phi/2 > \phi > \phi_0 + \Delta\phi/2 \\ 0, & \text{otherwise} \end{cases} \quad (5.7)$$

It can be seen that the rectangular model amplifies the signal at the beam edges while the triangular model attenuates. From that perspective, one can consider the

rectangular model as the upper bound whereas the triangular model as the lower bound.

5.2.2 Antenna Gain vs. Beamwidth

Since the efficiency of phased array antennas are almost perfect [29], we use antenna gain and directivity interchangeably, i.e. $G = D$. Then, for uniform excitation of the elements², antenna gain at an arbitrary scan angle $0^\circ < \phi_0 < 180^\circ$ for ULA, with an inter-element spacing of $d = \lambda/2$, is given as [29]

$$G = N \quad (5.8)$$

where N is the number of antenna elements. Eq. (5.8) simply states that the antenna gain equals the number of elements and is independent of scan angle for a fixed number of array elements. However, the beamwidth changes with scan angle and is given in degrees for $d = \lambda/2$ as [27, 28]

$$\Delta\phi = \frac{101.5^\circ}{N \sin \phi_0} \quad (5.9)$$

for $0^\circ < \phi_0 < 180^\circ$. At exactly endfire, i.e. $\phi_0 = 0^\circ, 180^\circ$, $\Delta\phi = 152.53^\circ/\sqrt{N}$.

Combining Eq. (5.8) and (5.9), the ULA antenna gain as a function of beamwidth, with uniform weighting, for $d = \lambda/2$, can be given as

$$G = \frac{101.5}{\Delta\phi \sin \phi_0} \quad (5.10)$$

for $0^\circ < \phi_0 < 180^\circ$ and the endfire gain is given as $G = (152.53^\circ/\Delta\phi)^2$.

5.3 Angular Distribution of Total Power and Extracted Power

In this section, we give expressions for the extracted power by a $\Delta\phi$ -beamwidth antenna ($P_{ext}(\Delta\phi)$) using the power-angle spectrum of two cluster channel models, IEEE 802.11ad and RT-ICM. To be comparable, we use the same total power, P_{tot} , obtained from RT-ICM in Eq. (5.5) for both cluster models.

²Or rectangular window tapering for window-based array designs

5.3.1 Extracted Power for IEEE 802.11ad Cluster Model

Letting ϕ_{cl} is the cluster AoA, p.d.f. of the angular distribution of a cluster is given in [10] as $f(\phi) = 1/(\sqrt{2\pi\sigma^2})e^{-(\phi-\phi_{cl})^2/(2\sigma^2)}$. Normalized power that is captured by the beam that is steered to ϕ_0 with a beamwidth $\Delta\phi$ can be obtained by

$$\rho = \int_{\phi_0-\Delta\phi/2}^{\phi_0+\Delta\phi/2} W(\phi)f(\phi)d\phi \quad (5.11)$$

where $W(\phi)$ is the beam shape defined in Sec. 5.2.1, $W(\phi) = W_R$ for rectangular and $W(\phi) = W_T$ for triangular model.

Then the *average* extracted power from the cluster for IEEE standard model becomes

$$P_{ext}^{st} = P_{tot}\rho \quad (5.12)$$

5.3.2 Extracted Power for RT-ICM

In RT-ICM, a cluster is generated totally by a single-order reflection and a reflector creates only one cluster. With this assumption, the strongest component in a cluster is the specular reflection which yields that the specular ray AoA can be set as the cluster AoA, i.e. $\phi_{sp} = \phi_{cl}$.

In RT-ICM, rays within the angle spread are equally-separated with a fixed spacing, $\Delta\alpha$. Then, the number of rays that drops within $\Delta\phi$ is $N_b = \lfloor \Delta\phi/\Delta\alpha \rfloor$. Then, the extracted power for RT-ICM can be given in the same discrete angle domain as

$$P_{ext}^{rt} = a_{sp}^2 + \frac{\Delta\phi}{N_b} \sum_{k=m}^{m+N_b-1} a_k^2 \quad (5.13)$$

where $m = \arg\{a_k | a_k = \phi_0 - \Delta\phi/2 + d\phi, k = 0, 1, \dots, N_r^d\}$ and $d\phi \geq 0$ is the minimum continuous angle that requires to select the first ray within the beamwidth.

The optimization of the beamwidth requires to take the derivation of Eq. (5.13) with respect to $\Delta\phi$. However, $\Delta\phi$ is in the argument which makes the derivation hard. Instead, we give an alternative approach via approximation.

Gaussian Approximation

In RT-ICM, the diffuse scattering loss is modeled with a raised cosine function which results in a *Gaussian-like* received power spectrum in the spatial domain in the linear scale. Hence, we seek to fit a Gaussian function to the power angle profile output of RT-ICM. The Gaussian function is of the form $g(\phi) = ue^{(\phi-x)^2/v^2}$ where the parameters u , v and x control the peak, the width and the mean of the function, respectively. We select these parameters such that the resultant function fits best to the data. An algorithm is proposed for Gaussian fitting in [61]. Then, the extracted power with a beamwidth $\Delta\phi$ is obtained by

$$P_{ext}^{rt} = \int_{\phi_0 - \Delta\phi/2}^{\phi_0 + \Delta\phi/2} W(\phi)g(\phi)d\phi \quad (5.14)$$

5.4 Problem Formulation

In case of an imperfect channel knowledge, cluster angle of arrival, ϕ_{cl} , is estimated with an error. Additionally, a quantization error is introduced at the receiver when a codebook is implemented for beamforming. Then the total misalignment error at the receiver can be defined as³ $\delta = |\phi_0 - \phi_{cl}|$. We first set up the problem formulation with $W(\phi) = W_R$.

5.4.1 IEEE 802.11ad

Plugging antenna gain and extracted power equations in Eq. (5.10) and (5.12), respectively, into Eq. (5.3),

$$P_R(\Delta\phi) = \frac{101.5^\circ}{\Delta\phi \sin \phi_0} P_{tot} \rho \quad (5.15)$$

³Absolute value is inserted to keep the error positive as all the functions used in the analysis are symmetric.

where ρ is integral given in Eq. (5.11). From [62], the integration of a Gaussian can be defined with the error function (erf). Then,

$$\begin{aligned}\rho &= \int_{\phi_{cl}+\delta-\Delta\phi/2}^{\phi_{cl}+\delta+\Delta\phi/2} W_R(\phi) \frac{1}{\sqrt{2\pi\sigma^2}} e^{-\frac{(\phi-\phi_{cl})^2}{2\sigma^2}} d\phi \\ &= \frac{1}{2} \left(\operatorname{erf} \left(\frac{\Delta\phi + 2\delta}{2\sqrt{2}\sigma} \right) + \operatorname{erf} \left(\frac{\Delta\phi - 2\delta}{2\sqrt{2}\sigma} \right) \right)\end{aligned}\quad (5.16)$$

where $erf(z) = 1/\sqrt{2\pi} \int_0^z e^{-y^2/2} dy$. Plugging into Eq. (5.15), the received power can be given as following:

$$P_R(\Delta\phi) = \frac{50.75P_{tot}}{\Delta\phi \sin \phi_0} \left(\operatorname{erf} \left(\frac{\Delta\phi + 2\delta}{2\sqrt{2}\sigma} \right) + \operatorname{erf} \left(\frac{\Delta\phi - 2\delta}{2\sqrt{2}\sigma} \right) \right) \quad (5.17)$$

such that $0 < \Delta\phi$.

Maximization of P_R

We seek to find the optimum $\Delta\phi = \Delta\phi_{opt}$ that maximizes the Eq. (5.17). Since P_{tot} and $\sin \phi_0$ are positive and scaling doesn't affect the optimization, the problem can be reduced to the following:

$$\max \frac{\operatorname{erf} \left(\frac{\Delta\phi + 2\delta}{2\sqrt{2}\sigma} \right) + \operatorname{erf} \left(\frac{\Delta\phi - 2\delta}{2\sqrt{2}\sigma} \right)}{\Delta\phi} \quad (5.18)$$

Making an argument whether the Eq. (5.18) is concave is not straightforward. To investigate the concavity of the function, we apply Second Derivative Test which is summarized as follows. If $q'(z_0) = 0$ and $q''(z_0) < 0$, then z_0 is the local maximum of the function $q(z)$. The simplified conditions derived from the first and the second derivatives of the Eq. (5.18) are given in Eq. (5.19) and (5.20) below, respectively. The details are placed in Appendix B.1.

$$\Delta\phi \left(e^{-(\Delta\phi+2\delta)^2/8\sigma^2} + e^{-(\Delta\phi-2\delta)^2/8\sigma^2} \right) - \sigma\sqrt{2\pi} \left(\operatorname{erf} \left(\frac{\Delta\phi+2\delta}{2\sqrt{2}\sigma} \right) + \operatorname{erf} \left(\frac{\Delta\phi-2\delta}{2\sqrt{2}\sigma} \right) \right) = 0 \quad (5.19)$$

$$\frac{\Delta\phi(\Delta\phi(\Delta\phi+2\delta)+8\sigma^2)}{e^{(\Delta\phi+2\delta)^2/8\sigma^2}} + \frac{\Delta\phi(\Delta\phi(\Delta\phi-2\delta)+8\sigma^2)}{e^{(\Delta\phi-2\delta)^2/8\sigma^2}} > \left(\operatorname{erf} \left(\frac{\Delta\phi+2\delta}{2\sqrt{2}\sigma} \right) + \operatorname{erf} \left(\frac{\Delta\phi-2\delta}{2\sqrt{2}\sigma} \right) \right) \quad (5.20)$$

Due to the erf function, no closed-form is available for Eq. (5.19), thus, solving it for $\Delta\phi > 0$ is performed numerically, for fixed δ and σ . The function has always 2 roots, one at the infinity. Plugging the roots to Eq. (5.20), it can be seen that the

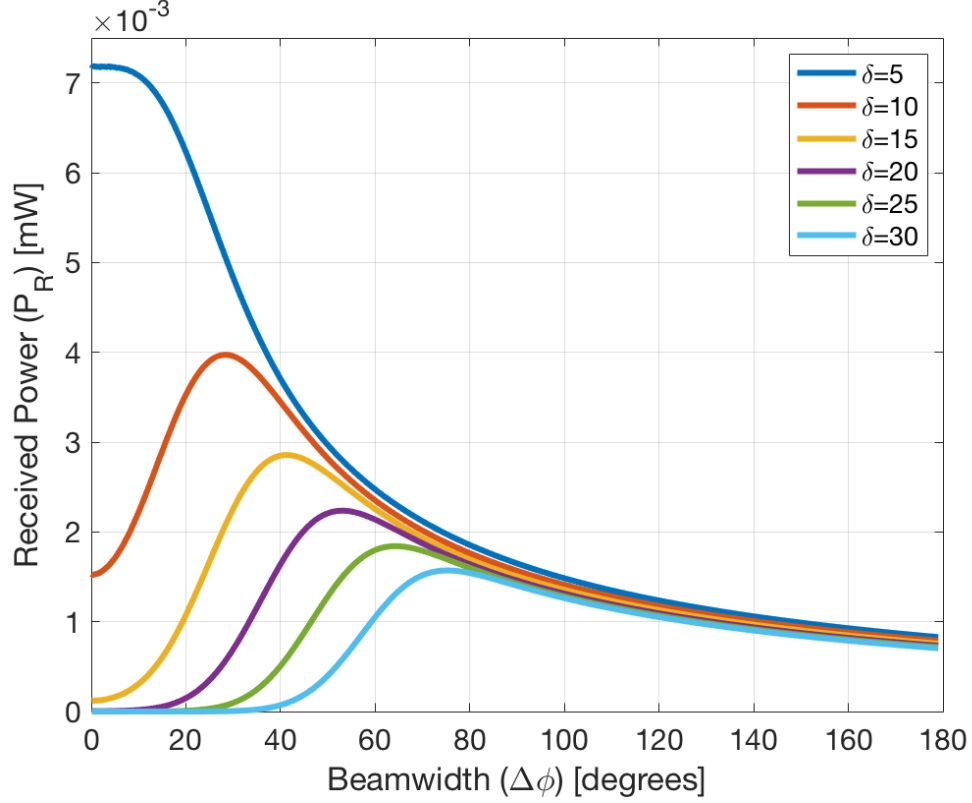


Figure 5.3: Received power in case of misalignment for $\sigma = 5$ and $P_{tot} = 1.2\mu W$.

condition fails for the infinity root. Furthermore, it is counter-intuitive to have the infinitely large $\Delta\phi_{opt}$ for the maximized received power. In fact, this root is the local minimum of the function which *minimizes* the received power.

An example simulation of the P_R in linear scale with respect to $\Delta\phi$ for different δ values are given in Fig. 5.3 where $P_{tot} = 1.2\mu W$, $\sigma = 5^\circ$ and $\phi_0 = 53^\circ$. It can be seen that the second derivative test would result in the single local maximum, i.e., global maximum. This leads to the following remark.

Remark 1. There exists a unique $\Delta\phi > 0$ that satisfies the both conditions in Eq. (5.19) and (5.20) for the given δ and σ such that $\delta > \sigma$. This unique value is the optimum beamwidth, $\Delta\phi_{opt}$, that maximizes the received power for the given δ and σ .

Also, to be proven in the simulation results in Sec. 6.4, we propose another important remark:

Remark 2. The following statements are always true. (1) When $\delta > \sqrt{2}\sigma$, $\Delta\phi_{opt} > 2\delta$,

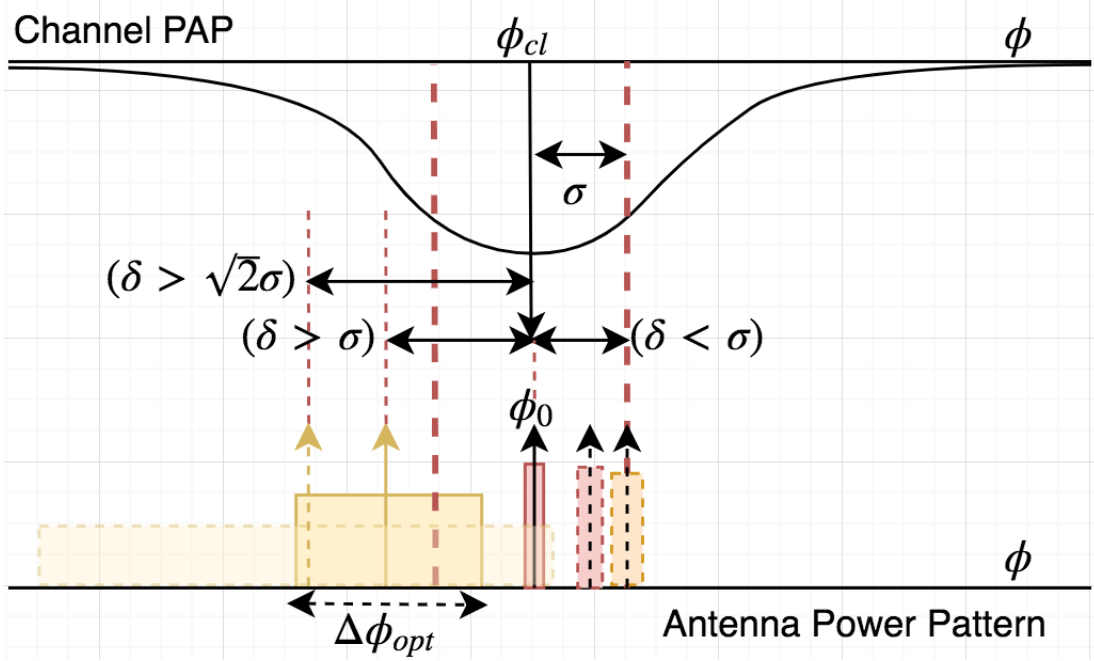


Figure 5.4: Optimum beamwidth in case of misalignment.

(2) When $\delta \leq \sigma$, $\Delta\phi_{opt} = 0$.

To get the insight of the results, consider the diagram given in Fig. 5.4. The relation between δ and σ has a significant effect on the value of $\Delta\phi_{opt}$. As long as $\delta \leq \sigma$, it is enough for the antenna to capture a little from the first σ region of the channel spectrum and antenna gain dominates the maximum received power. However, once $\delta > \sigma$, channel gain that is captured from the tail is considerably small such that even the antenna gain cannot tolerate. Hence, regardless of δ , the maximum received power is achieved only when the beam captures from the first σ region of the channel spectrum. Furthermore, if $\delta > \sqrt{2}\sigma$, beam should cover the center of the cluster. That is, $\Delta\phi_{opt}/2 > \delta$, or $\Delta\phi_{opt} > 2\delta$.

Finally, once optimum beamwidth is determined, maximum received power can be obtained by plugging $\Delta\phi_{opt}$ into Eq. (5.17),

$$P_{max} = P_R(\Delta\phi_{opt}) \quad (5.21)$$

5.4.2 RT-ICM

Apparently, the equations, given in Eq. (5.12) and (5.14), are equal with different notations. Hence, skipping the intermediate steps, received power for RT-ICM is given as

$$P_R^{rt}(\Delta\phi) = \frac{50.75uv\sqrt{\pi}}{\Delta\phi \sin \phi_0} \left(\operatorname{erf}\left(\frac{\Delta\phi + 2\delta}{2v}\right) + \operatorname{erf}\left(\frac{\Delta\phi - 2\delta}{2v}\right) \right) \quad (5.22)$$

Maximization procedure of $P_R^{rt}(\Delta\phi)$ is analogous to the 802.11ad case. In fact, setting $\sigma = v/\sqrt{2}$ in Eq. (5.19) and (5.20), conditions for RT-ICM can be provided.

Note that the IEEE 802.11ad standard sets σ to a fixed value for specific environments whereas RT-ICM generates different v for each cluster. In any way, after getting v , one can convert it to σ and use the same notation with 802.11ad.

5.4.3 Asymptotic Analysis of Perfect Alignment

It is already shown that $\Delta\phi_{opt} = 0$ when $\delta \leq \sigma$. Note that infinitely many elements ($N = \infty$) are required to achieve $\Delta\phi_{opt} = 0$, which is impractical. In this section, we perform an asymptotic analysis of the maximum achievable received power while $\Delta\phi_{opt} \rightarrow 0$ and provide an expression that results in practical beamwidth values that captures a percentile of the maximum achievable power. We perform the analysis with the 802.11ad model but give the counterpart expressions for RT-ICM at the end of the section as well.

To simplify the analysis and create a generic expression for any σ , let us assume $\delta = 0$, i.e. $\phi_0 = \phi_{cl}$. Then from Eq. (5.11), for $W(\phi) = W_R$, ρ becomes⁴,

$$\rho = \operatorname{erf}\left(\frac{\Delta\phi}{2\sqrt{2}\sigma}\right) \quad (5.23)$$

Plugging into Eq. (5.15), received power equation simplifies to,

$$P_R(\Delta\phi) = \frac{101.5P_{tot}}{\Delta\phi \sin \phi_0} \operatorname{erf}\left(\frac{\Delta\phi}{2\sqrt{2}\sigma}\right) \quad (5.24)$$

⁴It can also be verified by plugging $\delta = 0$ in Eq. (5.16).

Maximum Received Power

We now seek to find the maximum received power as the limit $\Delta\phi \rightarrow 0$. Eq. (5.24) is in the 0/0 indeterminate form for $\Delta\phi = 0$. Applying L'Hopital rule, the maximum achievable received power is

$$P_{max}^t = P_R(0) = \frac{40.5P_{tot}}{\sigma \sin \phi_0} \quad (5.25)$$

Intermediate steps are given in the Appendix B.2.

Optimum Practical Beamwidth

Note that the maximum received power given in the Eq. (5.25) is theoretical. Achieving very small beamwidth requires impractically high number of antenna elements as the relation given in Eq. (5.9) suggests. However, we can keep the beamwidth in practical ranges while sacrificing subtle from the received power.

Let $0 < \eta \leq 1$ be the coefficient such that

$$P_{\eta}^t = \eta P_{max}^t \quad (5.26)$$

where P_{η}^t is the η -percentile power of the P_{max}^t . Then, from Eq. (5.24),

$$\frac{101.5P_{tot}}{\Delta\phi \sin \phi_0} \operatorname{erf}\left(\frac{\Delta\phi}{2\sqrt{2}\sigma}\right) = P_{\eta}^{st} = \eta \frac{40.5P_{tot}}{\sigma \sin \phi_0} \quad (5.27)$$

Simplifying the equation and setting $\Delta\phi = \Delta\phi_{\eta}$, i.e. practical η -percentile beamwidth,

$$\frac{\Delta\phi_{\eta}}{\operatorname{erf}\left(\frac{\Delta\phi_{\eta}}{2\sqrt{2}\sigma}\right)} = \frac{2.5\sigma}{\eta} \quad (5.28)$$

Similar to the imperfect alignment case in Eq. (5.18), Eq. (5.28) shows that the optimum beamwidth depends only on the angle spread of the cluster while total cluster power and the scan angle has no effect at all. However, different from the imperfect alignment, an approximate solution can be provided for Eq. (5.28). Expanding the $\operatorname{erf}(z)$ function to Taylor series such that $\operatorname{erf}(z) = 2(z - z^3/3 + z^5/10 - z^7/42 + \dots) / \sqrt{\pi}$ where $z = \Delta\phi/\sqrt{8}\sigma$, we can approximate it ignoring the high order terms when $\Delta\phi/\sqrt{8}\sigma < 1$. Referring to Appendix B.2 for the derivation, the η -percentile beamwidth

can be given, approximately,

$$\Delta\phi_\eta \approx 4.89 \sigma \sqrt{1-\eta} \quad (5.29)$$

As shown in the simulation results section, Eq. (5.29) provides a strong yet simple tool to determine the optimum beamwidth within the practical limits. However, once $\Delta\phi > \sqrt{8}\sigma$, approximation of the error function starts getting apart from the real value. Setting $\Delta\phi \leq \sqrt{8}\sigma$ as the support region of $\Delta\phi$, from Eq. (5.29),

$$\begin{aligned} 4.89 \sigma \sqrt{1-\eta} &\leq \sqrt{8}\sigma \\ \eta &\geq 0.667 \end{aligned} \quad (5.30)$$

which provides the lower bound accuracy limit of the Eq. (5.29). Finally, to prove that Eq. (5.29) results in practical beamwidth values for conference room environments, from Eq. (5.30) and (5.33), beamwidth is given in the support range of $\Delta\phi_\eta \leq 14.10$ which can be achieved at the broadside using $N \geq 8$ antenna elements.

Plugging the given standard deviation for conference room environments [10] $\sigma = 5$, Eq. (5.25), (5.28) and (5.29) becomes

$$P_{max}^{st} = \frac{8.1 P_{tot}}{\sin \phi_0} \quad (5.31)$$

$$\frac{\Delta\phi^{st}}{\text{erf}\left(\frac{\Delta\phi^{st}}{10\sqrt{2}}\right)} = \frac{12.5}{\eta} \quad (5.32)$$

$$\Delta\phi^{st} = 24.45 \sqrt{1-\eta} \quad (5.33)$$

Due to the similar discussion made in Sec. 5.4.2, we just give the RT-ICM counterpart expressions here. With notation changes, received power equation becomes

$$P_R^{rt}(\Delta\phi) = \frac{101.5 uv \sqrt{\pi}}{\Delta\phi \sin \phi_0} \text{erf}\left(\frac{\Delta\phi}{2v}\right) \quad (5.34)$$

The maximum received power for the RT-ICM is

$$P_{max}^{rt} = \frac{101.5u}{\sin \phi_0} \quad (5.35)$$

Exact equation for the practical η -percentile beamwidth, $\Delta\phi_\eta$, for the RT-ICM,

Table 5.1: Asymptotic Analysis of P_{max} and Performance Comparison of 802.11ad and RT-ICM

η -percentile	$\Delta\phi^{st}$	N^{st}	$\Delta\phi^{rt}$	N^{rt}
0.999	0.8°	166	1.0°	126
0.99	2.5°	52	3.2°	40
0.95	5.6°	23	7.3°	18
0.9	8.1°	16	10.6°	12
0.75	14.0°	10	18.3°	7
0.5	24.7°	6	32.3°	4

$$\frac{\Delta\phi^{rt}}{\text{erf}\left(\frac{\Delta\phi^{rt}}{2v}\right)} = \frac{v\sqrt{\pi}}{\eta} \quad (5.36)$$

and its approximation for $\Delta\phi \leq 2v$,

$$\Delta\phi^{rt} \approx 3.46 v \sqrt{1 - \eta} \quad (5.37)$$

Table 5.1 shows a case study with a cluster in a typical indoor environment. The total power, P_{tot} in dBm is calculated via RT-ICM to be -29.09 . Scan angle is, $\phi_0 = 53^\circ$ and SAS is $S_\Omega = 72.2^\circ$. Corresponding Gaussian fitting parameters for RT-ICM are $u = 6.43 \times 10^{-5}$ and $v = 9.23$ (or $\sigma = 9.23/\sqrt{2} = 6.52$). Then, from Eq. (5.31) and (5.35), and converting to dBm, $P_{max}^{st} = -19.15$ and $P_{max}^{rt} = -20.87$ both in dBm. In Table 5.1, we calculate $\Delta\phi^{st}$ and $\Delta\phi^{rt}$ numerically using Eq. (5.32) and (5.36), respectively. Associated required number of elements to create the beamwidths, N^{st} and N^{rt} are computed using Eq. (5.9). While infinite number of antenna elements are required to achieve asymptotic values of the received power, Table 5.1 shows that high percentile powers can be obtained via practical values of N . On the other hand, it can be seen that for $\eta \geq 0.95$, in spite of the beamwidth difference between 802.11ad and RT-ICM is subtle, the difference in the required number of elements is increasing significantly. That proves that the hardware complexity to achieve optimum beamwidth value is directly related (and sensitive) to the correct estimation of the cluster parameters such as angle spread.

5.4.4 Triangular Beam Model

Throughout the chapter, we used the rectangular beam model given in Eq. (5.6) so far for all the analysis. In this section, we update the main equations for triangular beam model given in Eq. (5.7) and provide the difference with respect to the rectangular beam model.

Remark 3. Following statements are true for both perfect and imperfect alignments:

- (1) $\Delta\phi_{opt}$ doesn't depend on the main lobe beam model. (2) The difference in maximum achievable power is 1.23 dB.

Starting from the perfect alignment, Eq. (5.11) is calculated as following:

$$\begin{aligned}\rho &= \int_{\phi_{cl}-\Delta\phi/2}^{\phi_{cl}+\Delta\phi/2} W_T f(\phi) d\phi \\ &= \text{erf}\left(\frac{\Delta\phi}{2\sqrt{2}\sigma}\right) - \frac{\sqrt{2}(1 - e^{-\Delta\phi^2/8\sigma^2})}{\sqrt{\pi}\Delta\phi}\end{aligned}\quad (5.38)$$

Plugging into Eq. (5.12), skipping intermediate steps, received power is obtained as

$$P_R(\Delta\phi) = \frac{101.5P_{tot}}{\Delta\phi \sin \phi_0} \text{erf}\left(\frac{\Delta\phi}{2\sqrt{2}\sigma}\right) - \frac{81P_{tot}\sigma(1 - e^{-\Delta\phi^2/8\sigma^2})}{\sin \phi_0 \Delta\phi^2} \quad (5.39)$$

Note that the first term is the $P_R(\Delta\phi)$ for the rectangular beam model given in Eq. (5.24) which is maximum at $\Delta\phi = 0$. On the other hand, the second term is always positive and minimized at $\Delta\phi = 0$. This proves that the P_{max} is at $\Delta\phi = 0$. Taking the limit while $\Delta\phi \rightarrow 0$, theoretical maximum power with the triangular model is

$$P_{T,max}^t = P_R(0) = \frac{30.5P_{tot}}{\sigma \sin \phi_0} \quad (5.40)$$

Comparing with the rectangular model in Eq. (5.25), the difference is

$$10 \log (P_{max}^t / P_{T,max}^t) = 1.23 \text{ dB} \quad (5.41)$$

Since the result doesn't depend on any parameter, it is also true for the RT-ICM case.

The proof for the imperfect alignment is performed via simulation as the difference equation is computed numerically due to the *erf*.

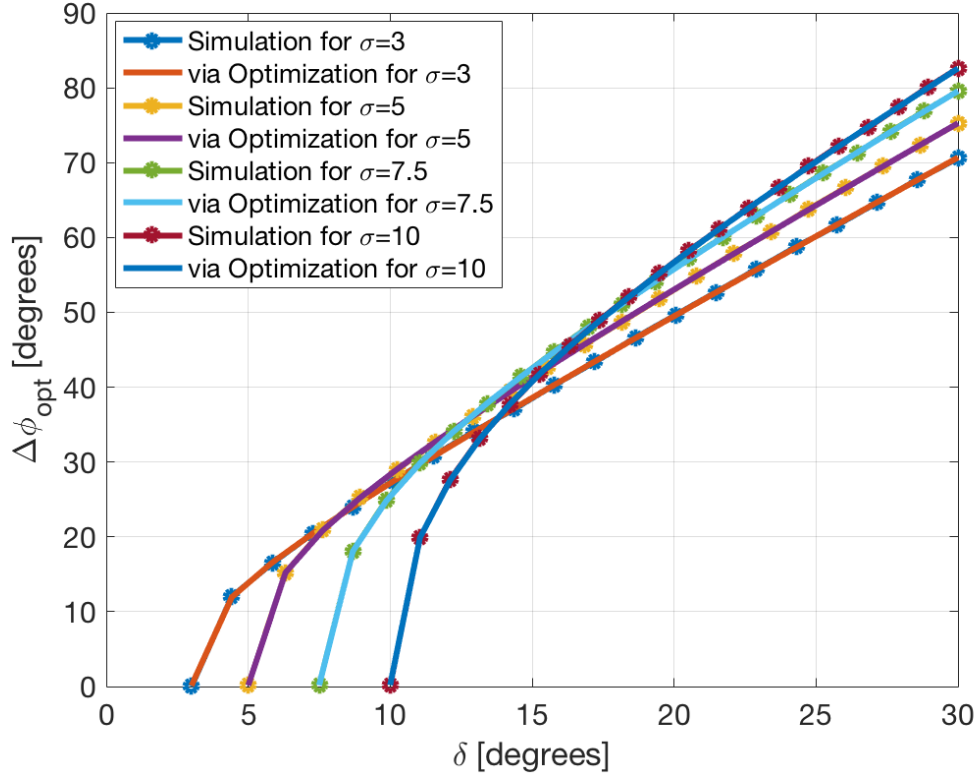


Figure 5.5: Accuracy of second derivative test method in case of misalignment and $\delta - \sigma$ relation effect on $\Delta\phi_{opt}$.

5.5 Performance Evaluation

In this section, we give the plots that illustrate the performance of the given analytical expressions by comparing with the simulations. We use the 802.11ad Gaussian notation for the performance results, but, to show the difference between fixed versus exact σ , we refer 802.11ad for fixed, RT-ICM for the true value. As both models agree for indoor mmWave clusters, we scan a range of 3° to 10° for σ .

In the first plot, we measure the accuracy of the method that uses the Second Derivative Test when finding the $\Delta\phi_{opt}$ in case of misalignment, given in Sec. 5.4.1. As seen from Fig. 5.5, optimization results for $\Delta\phi_{opt}$ perfectly match to simulation results for different values of σ and δ , as stated in *Remark 1*. On the other hand, note that $\Delta\phi_{opt} \rightarrow 0$ rapidly while $\delta \approx \sigma$. Also, it can be seen that $\Delta\phi_{opt} > 2\delta$ once $\delta \geq \sqrt{2}\sigma$. This concludes the proof of *Remark 2*.

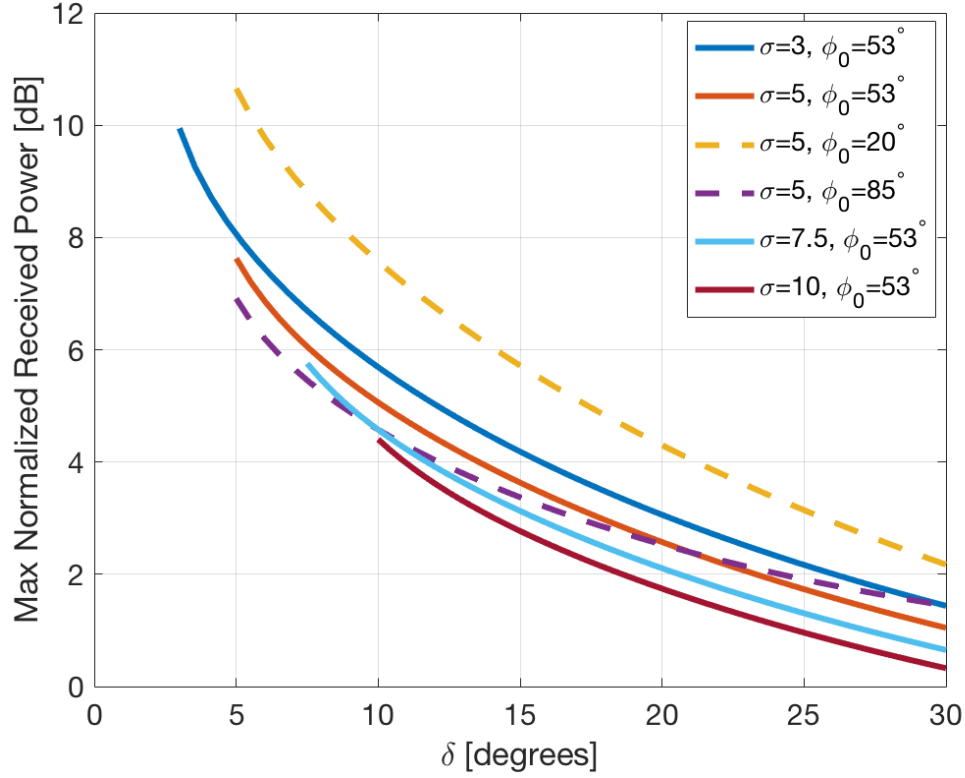


Figure 5.6: Variation on the maximum achievable received power with respect to δ for different σ and ϕ_0 .

Fig. 5.6 shows how the maximum received power given in Eq. (5.21) changes in dB scale with variation in δ for four different σ s. In the figure, the received power is normalized with P_{tot} . As seen, once $\delta > \sigma$, P_{max} drops exponentially and becomes the dominant degradation factor. However, even with a large δ , using a ULA has still advantages over an omnidirectional antenna. On the other hand, as $\delta \approx \sigma$, P_{max} reaches to its max level. Although not shown here, for $\delta < \sigma$, it saturates rapidly, which can be concluded from Fig. 5.3. That results in the following important conclusion: As long as $\delta < \sigma$, the misalignment error is tolerable thanks to the antenna gain and maximum power can be still achieved.

Fig. 5.6 also shows the effect of the steering angle ϕ_0 to P_{max} for $\sigma = 5$. As seen, P_{max} strictly depends on ϕ_0 due to the \sin factor in the denominator. However, recall that since ϕ_0 depends on the channel parameter ϕ_{cl} , user has limited control over it.

To illustrate the performance of the analysis in the case of perfect alignment (or

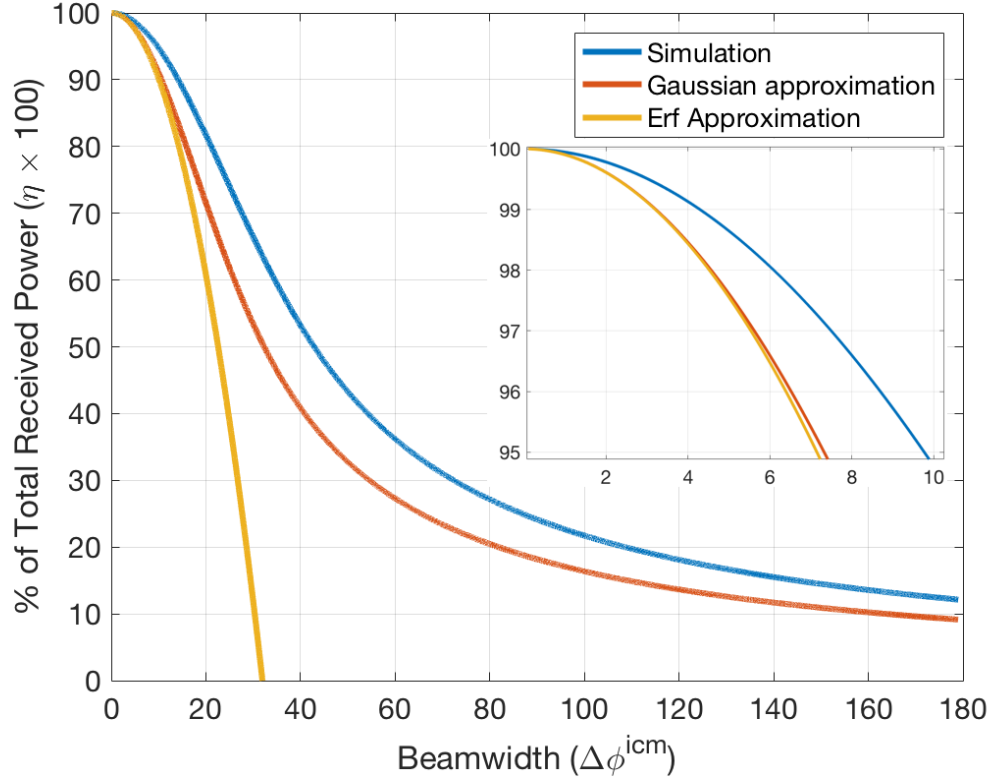


Figure 5.7: Practical beamwidth analysis performance of RT-ICM for $v = 9.23$ (or $\sigma = 6.52$).

$\delta < \sigma$), in Fig. 5.7, we demonstrate the performance of RT-ICM expressions given in Eq. (5.36) and (5.37) with respect to the percentile power in percentage, for $v = 9.23$. We use Eq. (5.13) to simulate the model without any approximation, shown with a blue line in the figure. The red curve is the resulted relation of Gaussian approximation given in Eq. (5.36), also some values are given in Table 5.1. Finally, the orange line is for the error function approximation given in Eq. (5.37) for the given condition that $\Delta\phi \leq 2v = 18.46$. Note that the approximation of the *erf* is in an almost perfect agreement with its numeric solution within the supported range. On the other hand, Gaussian fitting yields a result with a little error compared to simulation. However, for example, for $\eta = 0.99$, the beamwidth error is only 1° .

In Fig. 5.8, beamwidth error due to the fixed $\sigma = 5^\circ$ assumption in IEEE 802.11ad model is plotted for different percentile values. For ease of illustration, $\sigma = 5^\circ$ line is also stressed. It is seen that the optimum beamwidth sensitivity to σ increases if

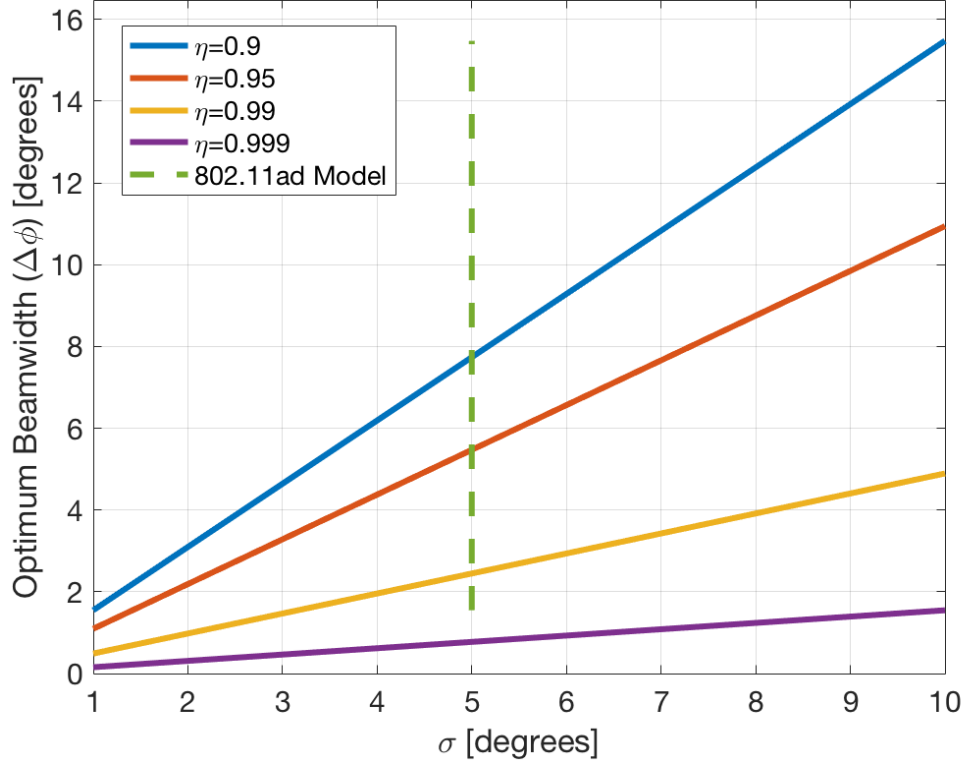


Figure 5.8: Beamwidth Error in IEEE 802.11ad model due to fixed $\sigma = 5^\circ$ in the perfect alignment case.

a low η is selected. For interference-limited systems where high power and directed beams are needed, the 802.11ad model works with subtle beamwidth errors, whereas for hardware-limited systems with a limited number of antenna elements, the 802.11ad model may estimate the optimum beamwidth with significant errors. Also, it is worthy to note that the increase (or decrease) rate at the required number of antenna elements (N) in case of an error is the same for all η values.

Fig. 5.9 demonstrates the total received power performance of both models with respect to the number of antenna elements that is required to create the optimum beamwidth. We plot the simulation for two models along with their corresponding received power equations given in (5.24) and (5.34), respectively. The same case study, given in Sec. 5.4.3, is used here. For the abscissa, we use the Eq. (5.9) for the transformation from $\Delta\phi$ to N . In the figure, $\eta = 0.95$ percentile points are also denoted

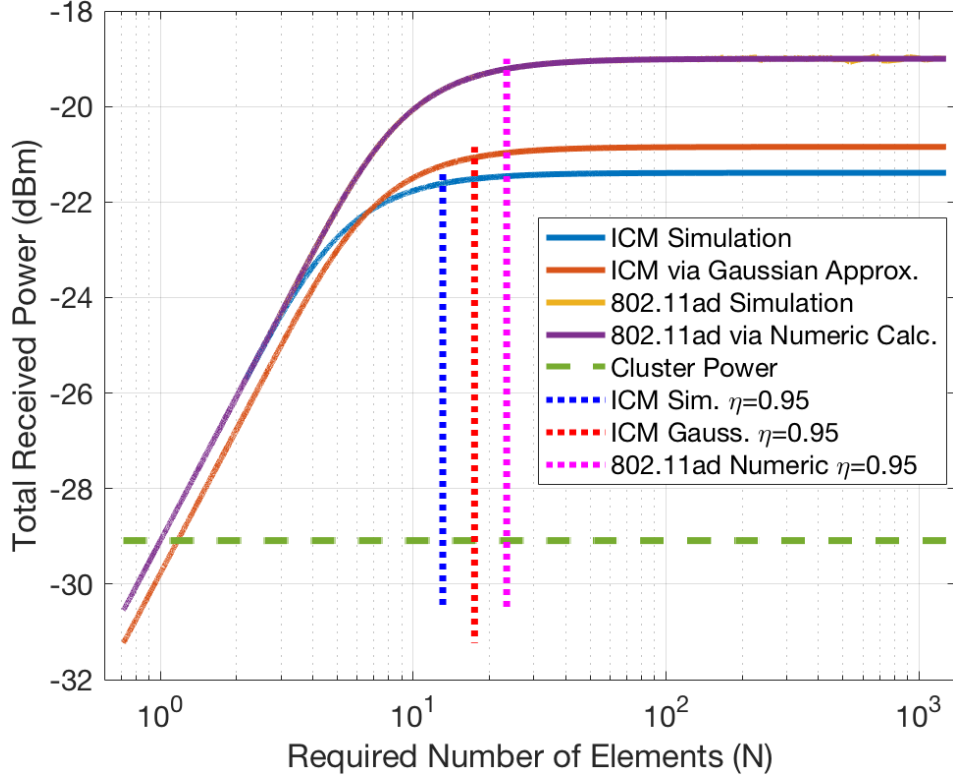


Figure 5.9: Models performance comparison in terms of required antenna elements for perfect alignment

with dotted lines. Recalling the high accuracy of the RT-ICM, we accept the RT-ICM simulation as the most accurate curve and compare the other realizations with it. As seen from the figure, 802.11ad model yields ~ 2 dB more total power both with simulation and analytical expression, for this case study. This effect is due to the smaller angle spread measurements of 802.11ad. It can also be confirmed from Eq. (5.25) where angle spread standard deviation is inverse relation with maximum received power. While $\sigma = 5$, fitting Gaussian function of RT-ICM angle spread standard deviation is estimated to be $v/\sqrt{2} = 6.52$ for this case study.

On the other hand, Fig. 5.9 shows that the required number of elements (N) to create a beamwidth that would achieve 95% of the maximum total power is 13, as shown with the blue dotted line. The Gaussian approximation of RT-ICM yields $N = 18$ whereas the 802.11ad model requires 23 elements to reach its 95% of maximum received power.

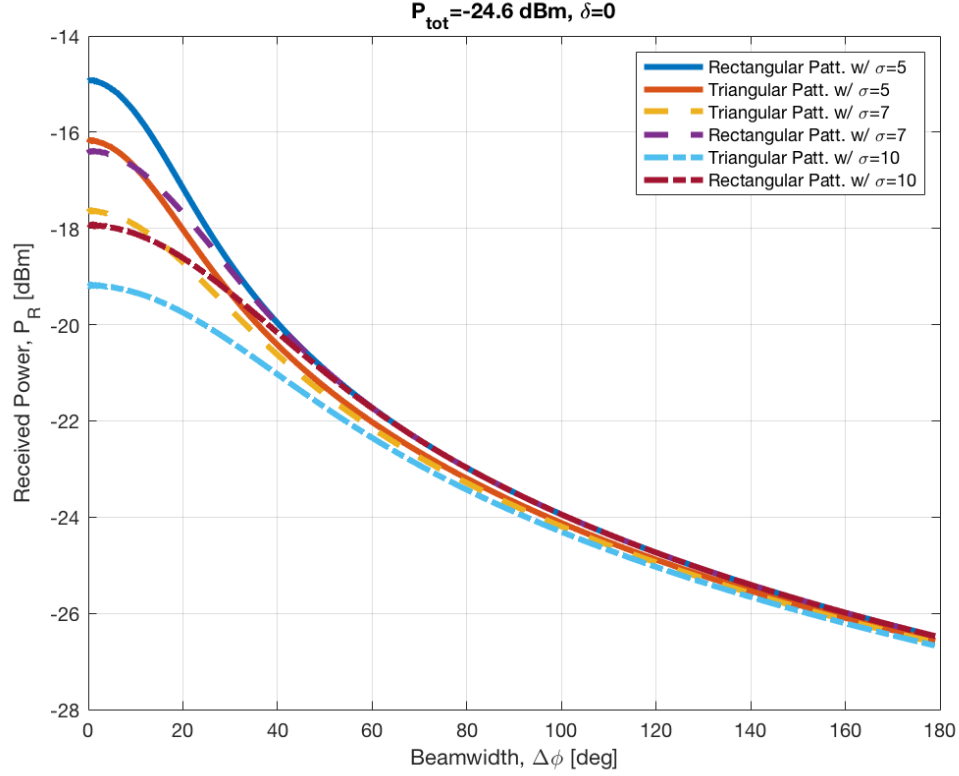


Figure 5.10: Beamwidth Error in IEEE 802.11ad model due to fixed $\sigma = 5^\circ$ in the perfect alignment case.

Finally, Fig. 5.10 and 5.11 show the triangular and the rectangular beam model comparison, for perfect and imperfect alignment, respectively. As derived in Sec. 5.4.4, while $\Delta\phi_{opt}$ is unchanged, P_{max} reduces 1.23 dB for the triangular model. Note the true shape of the main lobe is more like Gaussian, and its P_{max} should reside between rectangular and triangular model as shown in Fig. 5.2. Hence, using the rectangular model for the main lobe doesn't create significant errors while complexity in the derivation gets extremely simple.

5.6 Summary

In this chapter, we provide an analytical framework for the optimum beamwidth that maximizes the received power for indoor mmWave clusters. In the analysis, we consider the uniform linear array (ULA) antenna type for the antenna gain, and two beam

models to approximate the main lobe array pattern; rectangular and triangular. Expressions that relate the beamwidth and captured cluster channel gain is provided for two intra-cluster model, IEEE 802.11ad and Ray Tracing based Intra-Cluster Model (RT-ICM) and the optimization problem is introduced by combining the antenna gain. Both perfect and imperfect alignment scenarios are studied. For misalignment cases, the optimum beamwidth is found to be larger than the 2 times of the alignment error when the error is larger than the $\sqrt{2}$ of the standard deviation of the cluster channel. For perfect alignment, we show that the theoretical maximum received power converges to a constant while optimum beamwidth approaches to zero. We then provide equations that would result in practical beamwidth values while sacrificing from the maximum received power in the order of tenths percentage. Finally, we evaluate the performance of the analysis by comparing the analytical results with simulations for an indoor mmWave cluster. The work we propose in this chapter will give insights to the optimum antenna array design in both MIMO and massive MIMO applications for future mmWave systems.

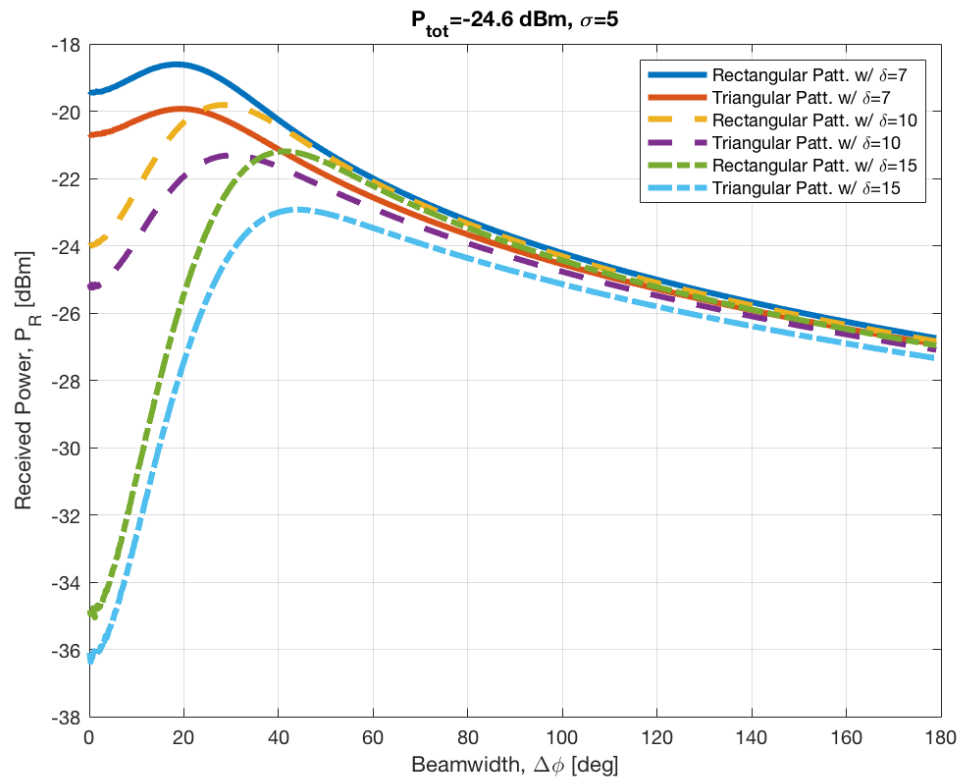


Figure 5.11: Models performance comparison in terms of required antenna elements for perfect alignment

Chapter 6

Optimum Beamwidth Analysis for Uniform Planar Arrays (UPAs)

In the previous chapter, we optimize the beamwidth for an indoor mmWave cluster which has a Gaussian angular pattern. In that study, we assumed that the device is employed with a uniform linear array (ULA) antenna and the optimization is performed based on that specific antenna type gain-beamwidth relation. In practice, although ULAs are also being planned to install to user equipment (UE) devices for some mmWave applications, the common approach is to use uniform planar array (UPA) antennas to exploit from both elevation and azimuth domains. To complete the research study, in this chapter, we give the derivations of the UPA counterpart of the beamwidth optimization problem for the indoor mmWave clusters. We show that once the antenna gain increases due to the UPA usage, channel angular pattern becomes less critical in the optimization.

6.1 System and Channel Model

We adopt the same system and channel model that are described in the previous chapter used in ULA case. In Fig. 6.1, an example diagram of the discussion is illustrated with a comparison of two beams created by a UPA and steered towards a cluster AoA.

6.2 Antenna Structure and Gain

As Eq. (5.3) suggests, antenna gain is the counterpart of the captured cluster power in the equation for a certain beamwidth. In the previous chapter, we simply assumed a well-known uniform linear array (ULA) design where the spacings between the elements are equal and provided the relationships between antenna gain, beamwidth, number of

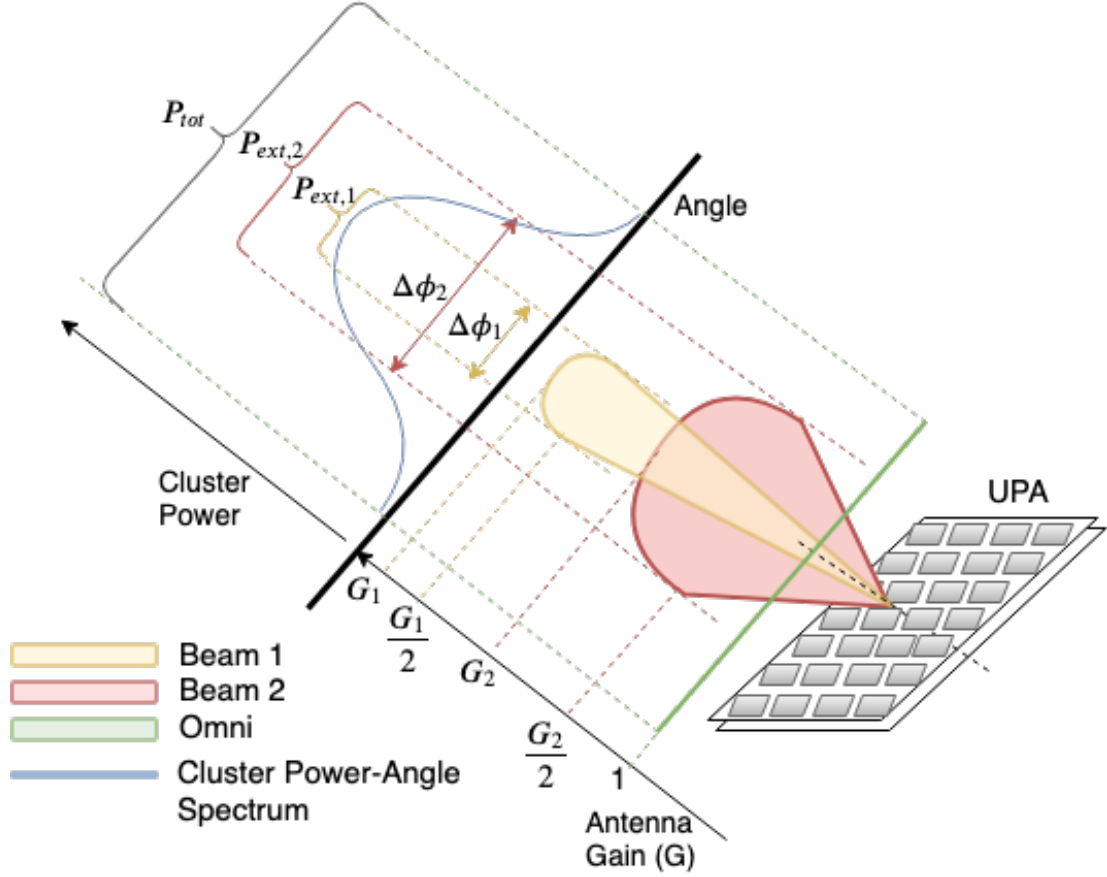


Figure 6.1: Visualization of the optimum beamwidth problem at the receiver

elements and scan angle for a ULA. In this chapter, we adopt the rectangular uniform planar array (R-UPA) antenna model as it is a more realistic and practical design in mmWave devices. In that aspect, we first derive the relation between the antenna gain and beamwidth¹, and then use the result to analyze the maximum received power by combining the extracted power from the cluster.

6.2.1 Beam Pattern Model

Two models for the beam pattern; a rectangular window and a triangular window were introduced in the previous chapter. In this chapter, we perform the analysis only for rectangular window as the effect of the triangular window doesn't depend on the antenna type and remains same.

¹both the azimuth and the elevation beamwidth

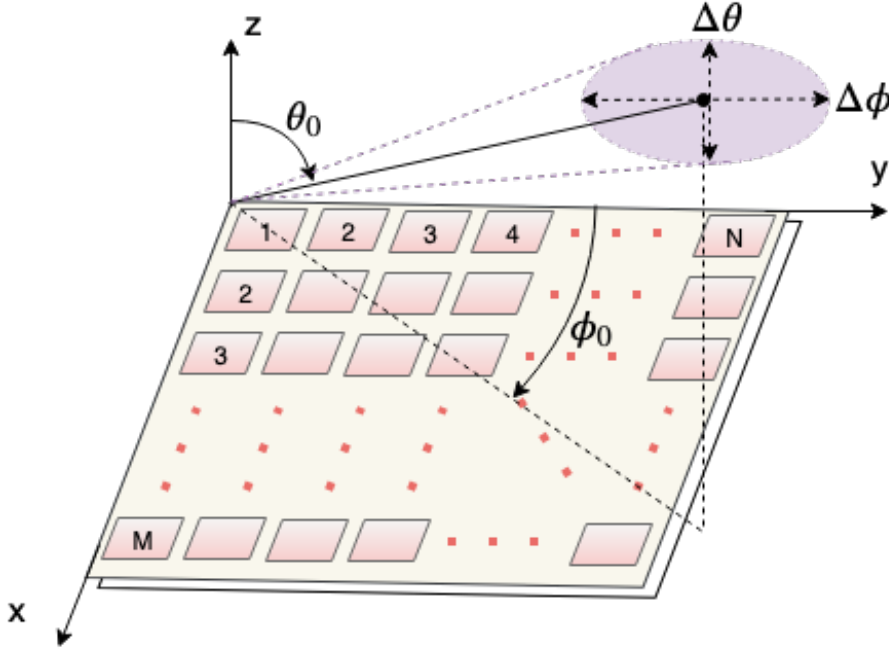


Figure 6.2: $(N \times M)$ -element rectangular UPA diagram with the scan angles and beamwidths illustration.

6.2.2 Directivity of RUPA

A diagram of a $M \times N$ -element rectangular UPA is given in Fig. 6.2. (θ_0, ϕ_0) and $(\Delta\theta, \Delta\phi)$ pairs are the elevation and azimuth scan angles and the beamwidths of the beam, respectively. The goal in this subsection is to find an expression for the array directivity in terms of the azimuth beamwidth. To simplify the analysis, we assume that the x and y direction inter-element spacings are both set to $\lambda/2$.

For large N and M , the directivity of a rectangular UPA is given in [28] as $D = \pi \cos \theta_0 D_x D_y$ where D_x and D_y are the directivities of the x-axis and the y-axis ULAs, respectively. Assuming the uniform excitation of all antenna elements, directivity of the x- and y-axis ULAs at broadside equals the number of elements on the corresponding axes, i.e. $D_x = M$ and $D_y = N$ [29]. Then, the UPA directivity becomes

$$D = \pi \cos \theta_0 NM \quad (6.1)$$

Further, using the beamwidth and the number of elements relation of a uniformly excited ULA with $\lambda/2$ spacing [27–29] where $\Delta\phi_x = 101.5/M$ and $\Delta\phi_y = 101.5/N$ are

the beamwidths of the x- and the y-axis ULAs, respectively, Eq. (6.1) is updated as

$$D = \pi \cos \theta_0 \frac{101.5^2}{\Delta \phi_x \Delta \phi_y} \quad (6.2)$$

On the other hand, the azimuth and the elevation beamwidths of a large rectangular UPA for arbitrary θ_0 and ϕ_0 are given in [28], respectively, as,

$$\Delta \theta = \sqrt{\frac{1}{\cos^2 \theta_0 (\Delta \phi_x^{-2} \cos^2 \phi_0 + \Delta \phi_y^{-2} \sin^2 \phi_0)}} \quad (6.3)$$

$$\Delta \phi = \sqrt{\frac{1}{\Delta \phi_x^{-2} \sin^2 \phi_0 + \Delta \phi_y^{-2} \cos^2 \phi_0}} \quad (6.4)$$

After combination of Eq. (6.3) and (6.4) and solving for $\Delta \phi_x$, we get

$$\Delta \phi_x = \frac{\Delta \theta \cos \theta_0 \Delta \phi_y \Delta \phi}{\sqrt{\Delta \phi^2 (\Delta \phi_y^2 - \Delta \theta^2 \cos^2 \theta_0) + \Delta \theta^2 \cos^2 \theta_0 \Delta \phi_y^2}} \quad (6.5)$$

Plugging $\Delta \phi_x$ into Eq. (6.2),

$$D = \frac{101.5^2 \pi \sqrt{\Delta \phi^2 (\Delta \phi_y^2 - \Delta \theta^2 \cos^2 \theta_0) + \Delta \theta^2 \cos^2 \theta_0 \Delta \phi_y^2}}{\Delta \theta \Delta \phi \Delta \phi_y^2} \quad (6.6)$$

As expected, directivity depends also on elevation scan angle (θ_0) and beamwidth ($\Delta \theta$) as well as y-axis ULA beamwidth at broadside ($\Delta \phi_y$). In order to be able to work with the channel side power angle spectrum where only the azimuth domain information is available, in the next subsection, we will pick reasonable selections for those parameters by discussing the theoretical constraints.

6.2.3 Selection of Angular Parameters

Constraint 1

Immediate first constraint is already imposed within the formulation of the UPA directivity. The large array assumption puts a limitation on $\Delta \phi_y$. Considering the large array limitation as $N \geq 7$ [28], the first constraint is setup as: $\Delta \phi_y \leq 101.5/7 = 14.5^\circ$.

Table 6.1: Some candidate selections of the parameters

Set ID	$\Delta\phi_y$	$\Delta\theta$	θ_0	Directivity (D)
1	14.5°	30°	75°	$\frac{20\pi\sqrt{84.68+\Delta\phi^2}}{\Delta\phi}$
2	14.5°	40°	70°	$\frac{5.91\pi\sqrt{1703+\Delta\phi^2}}{\Delta\phi}$
3	10.15°	40°	70°	$\frac{22.93\pi\sqrt{229-\Delta\phi^2}}{\Delta\phi}$
4	10.15°	30°	60°	$\frac{45.9\pi\sqrt{190-\Delta\phi^2}}{\Delta\phi}$

Constraint 2

Apparently, all beamwidth and scan angle values should be positive and real. From Eq. (6.5), to provide a real beamwidth value, the square root term should be real. To simplify the analysis further, we tighten the limitation and set the constraint as: $\Delta\phi_y^2 - \Delta\theta^2 \cos^2 \theta_0 \geq 0$.

Constraint 3

Finally, to ensure the aligned communication between two devices located at approximately the same height, we consider another constraint as: $\theta_0 + \Delta\theta/2 \approx 90^\circ$. The meaning of this constraint can be visually inspected from Fig. 6.2.

Based on these constraints, we derive the directivity expressions for a few different selections of the three parameters, $\theta_0, \Delta\theta, \Delta\phi_y$. In Table 6.1, 4 set of candidate parameter values are listed with their derived directivity formulas by plugging them into Eq. (6.6). Set 1 and 2 don't violate any constraint, however, constraint 2 doesn't hold for Set 3. Set 4 violates constraints 2 and 3.

Directivity and the azimuth beamwidth relation for these sets are plotted in Fig. 6.3. The effect of the violation of constraint 2 can be seen for Set 3 and 4 where the azimuth beamwidth is supported for a limited range.

Since the efficiency of phased array antennas are almost perfect [29], we use antenna gain and directivity interchangeably, i.e. $G = D$.

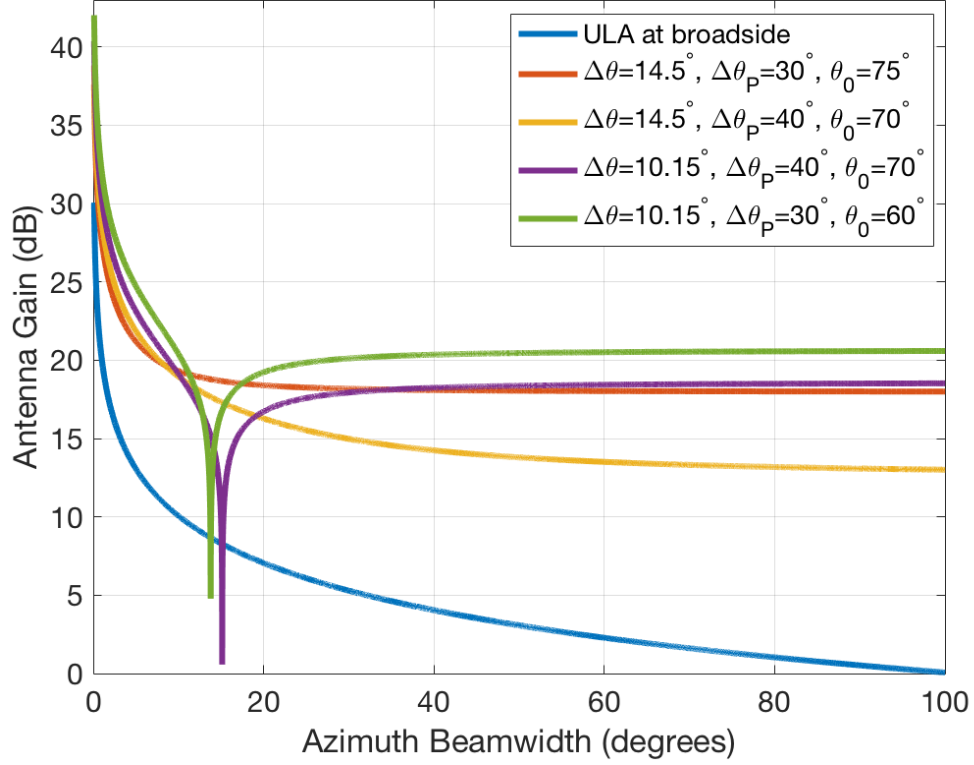


Figure 6.3: Directivities of the selected parameter sets and the effect of the constraints.

6.3 Problem Formulation

6.3.1 Extracted Power from Channel

For a perfect beam alignment to the channel, extracted power from IEEE 802.11ad intra-cluster Gaussian channel model was formulated in the previous chapter as

$$P_{ext}^{st} = P_{tot} \int_{\phi_{cl}-\Delta\phi/2}^{\phi_{cl}+\Delta\phi/2} W_R(\phi) \frac{1}{\sqrt{2\pi\sigma^2}} e^{-\frac{(\phi-\phi_{cl})^2}{2\sigma^2}} d\phi \quad (6.7)$$

where ϕ_{cl} is the cluster AoA. In the equation, we used rectangular beam shape given in Eq. (5.6).

For RT-ICM, we showed that the Gaussian approximation of the resultant power angle profile fits almost perfectly to the data. Then, the extracted power from RT-ICM is obtained by

$$P_{ext}^{rt} = \int_{x-\Delta\phi/2}^{x+\Delta\phi/2} W_R(\phi)g(\phi)d\phi \quad (6.8)$$

where $g(\phi) = ue^{(\phi-x)^2/v^2}$ is the Gaussian function that fits the data with the calculated variables u , x and v [61].

6.3.2 Received Power Problem Formulation

As Eq. (5.3) suggests, the received power from a cluster is the product of the antenna gain and the extracted power by the antenna for a given direction. At this point, for antenna gain ($G = D$), we will pick a scenario from the Table 6.1 and derive the received power according to the picked scenario. In fact, as we showed, since the optimized beamwidth falls into the region below $10^\circ - 15^\circ$, any of the candidate sets in the table could be used due to their similar performance which can be seen from Fig. 6.3. Here, we select the Set 4 and use the provided directivity equation to formulate the received power.

On the other hand, the integration of a Gaussian can be defined with the error function (*erf*) [62]. Then, the extracted power for 802.11ad given in Eq. (6.7) becomes

$$P_{ext}^{st} = P_{tot}\text{erf}\left(\frac{\Delta\phi}{2\sqrt{2}\sigma}\right) \quad (6.9)$$

Plugging the Set 4 antenna gain in Table 6.1 and P_{ext}^{st} into Eq. (5.3), received power as a function of beamwidth can be given as

$$P_R = \frac{45.9P_{tot}\pi\sqrt{190 - \Delta\phi'^2}}{\Delta\phi}\text{erf}\left(\frac{\Delta\phi}{2\sqrt{2}\sigma}\right) \quad (6.10)$$

Maximum Received Power

As the analysis shows in the previous chapter, optimum beamwidth that maximizes the received power in the case of perfect alignment converges to zero, i.e. $\Delta\phi_{opt} \rightarrow 0$. Hence, we perform an asymptotic analysis to get the theoretical maximum received power. Eq. (6.10) is in the 0/0 indeterminate form for $\Delta\phi = 0$. Applying L'Hopital

rule, the maximum achievable received power is

$$P_{max}^t = P_R(0) = \frac{793P_{tot}}{\sigma} \quad (6.11)$$

Optimum Practical Beamwidth

With a similar approach in the previous analysis, let $0 < \eta \leq 1$ be the coefficient such that

$$P_\eta^t = \eta P_{max}^t \quad (6.12)$$

where P_η^t is the η -percentile power of the P_{max}^t . Then, from Eq. (6.10),

$$\frac{144.2P_{tot}\sqrt{190 - \Delta\phi^2}}{\Delta\phi} \operatorname{erf}\left(\frac{\Delta\phi}{2\sqrt{2}\sigma}\right) = P_\eta^{st} = \eta \frac{793P_{tot}}{\sigma} \quad (6.13)$$

Simplifying the equation and setting $\Delta\phi = \Delta\phi_\eta$, i.e. practical η -percentile beamwidth,

$$\frac{\Delta\phi_\eta}{\operatorname{erf}\left(\frac{\Delta\phi_\eta}{2\sqrt{2}\sigma}\right)\sqrt{190 - \Delta\phi_\eta^2}} = \frac{\sigma}{5.5\eta} \quad (6.14)$$

Compared to ULA case, for $\sigma = 5^\circ$, Eq. (6.11) produces ≈ 13 dB more power. It is basically due to the higher antenna gain in UPA.

For completeness, we give the RT-ICM counterpart expressions of Eq. (6.11) and Eq. (6.14), respectively, as

$$P_{max}^r = 632.7\pi u \quad (6.15)$$

$$\frac{\Delta\phi_\eta}{\operatorname{erf}\left(\frac{\Delta\phi_\eta}{2v}\right)\sqrt{190 - \Delta\phi_\eta^2}} = \frac{v}{7.8\eta} \quad (6.16)$$

6.4 Performance Evaluation

In this section, we plot the performance of the derived expressions. In the first plot, we simulate the required beamwidth to obtain a percentile of the total achievable power and compare it with Eq. (6.14) for $\sigma = 5^\circ$. As seen from Fig. 6.4, the numerical plot of Eq. (6.14) perfectly agrees with the simulation, as expected. The most important result of the plot is that while an impractical 0° beamwidth is required to achieve maximum received power, a practical $\approx 3.5^\circ$ beamwidth value captures 95% of it.

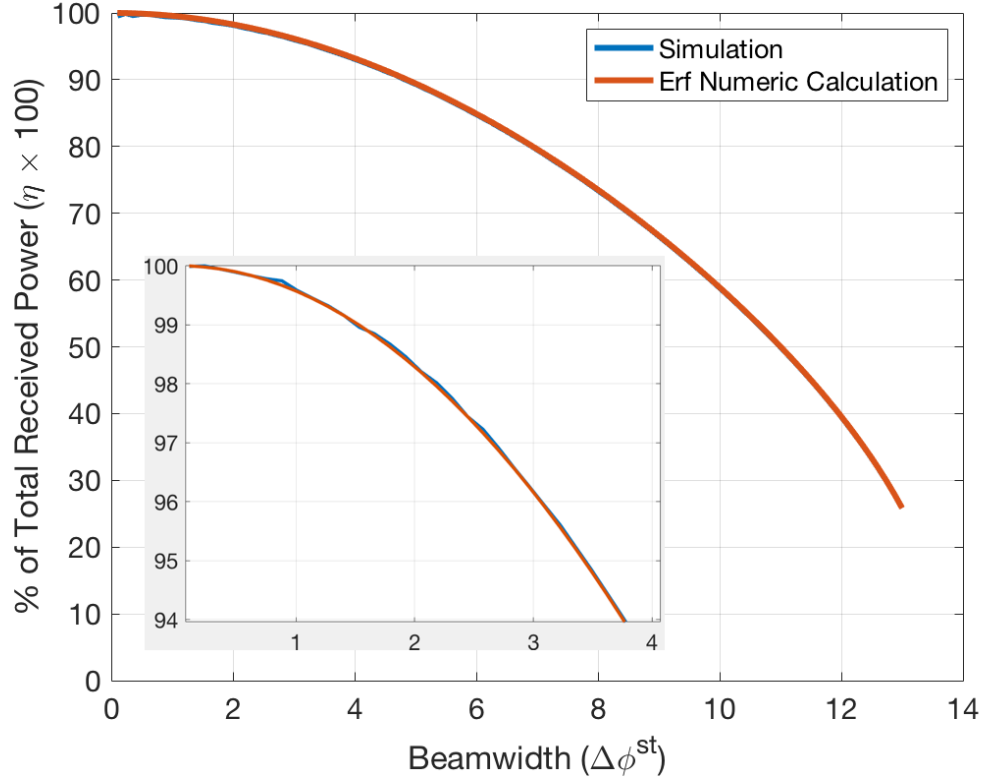


Figure 6.4: Percentage of received power versus beamwidth when $\sigma = 5$.

Next, in order to understand the channel effects, we run RT-ICM for the conference cluster given in Chapter 3 and obtain the followings: $P_{tot} = -29.09$ dBm, $\phi_{cl} = 90^\circ$ and $S_\Omega = 72.2^\circ$. After fitting to the Gaussian function, $u = 6.434e - 5$ and $v = 9.23$, which translates into $\sigma_r = \sqrt{2}v = 6.53^\circ$ in terms of Gaussian distribution. This corresponds to 1.53° difference compared to IEEE 802.11ad model with $\sigma = 5^\circ$. In Fig. 6.5, we investigate the effect of the σ difference by comparing IEEE 802.11ad and RT-ICM models as well as their 95%-percentile powers in terms of the beamwidth $\Delta\phi$. As seen, the difference in azimuth beamwidth can be assumed negligible ($< 1^\circ$). In Fig. 6.6, we also illustrate the required number of elements (N) counterpart of the comparison. Although the difference in N also seems subtle between the models and/or their approximations due to the logarithmic display, it can reach 30 – 50 elements difference which can be critical in the hardware-limited applications. However, when compared to ULA analysis, difference in the channel side (σ) doesn't affect UPA systems as critical as it affects the ULAs. That suggests that the UPA antenna gain becomes

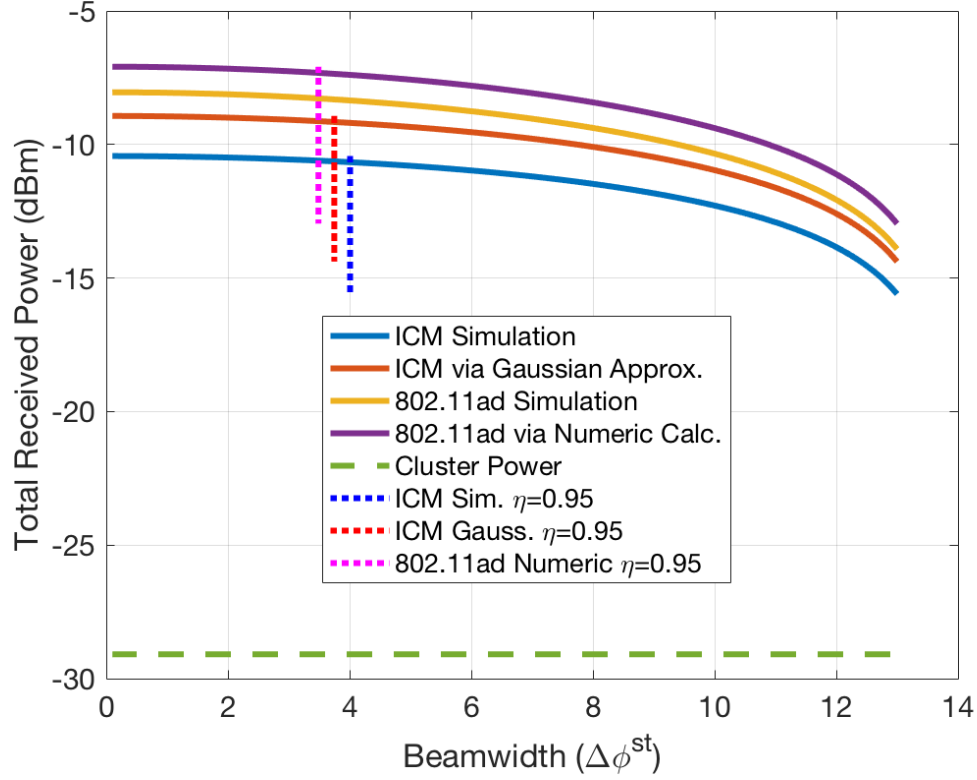


Figure 6.5: Total received power versus beamwidth.

dominant in the received power and the angular shape of the channel can be less of concern in the system designs.

Finally, we compare the ULA vs UPA for the same cluster. As discussed in the previous section, approximately 13 dB difference is visible which basically comes from the antenna gain. Note that to reach 95% of the ULA's maximum power, one needs $\Delta\phi = 5.6^\circ$ which can be generated using $N = 19$ elements in ULA. However, 95%-percentile power of UPA case can be obtained by $\Delta\phi = 3.4^\circ$ which translates into $N = 290$ elements. On the other hand, even for 50%-percentile in UPA case, the received power is still 10 times larger (10.2 dB) than ULA usage. That power can be obtained in UPA with 11° with using $N = 60$ elements. A typical practical UPA implementation can be 8×8 array structure.

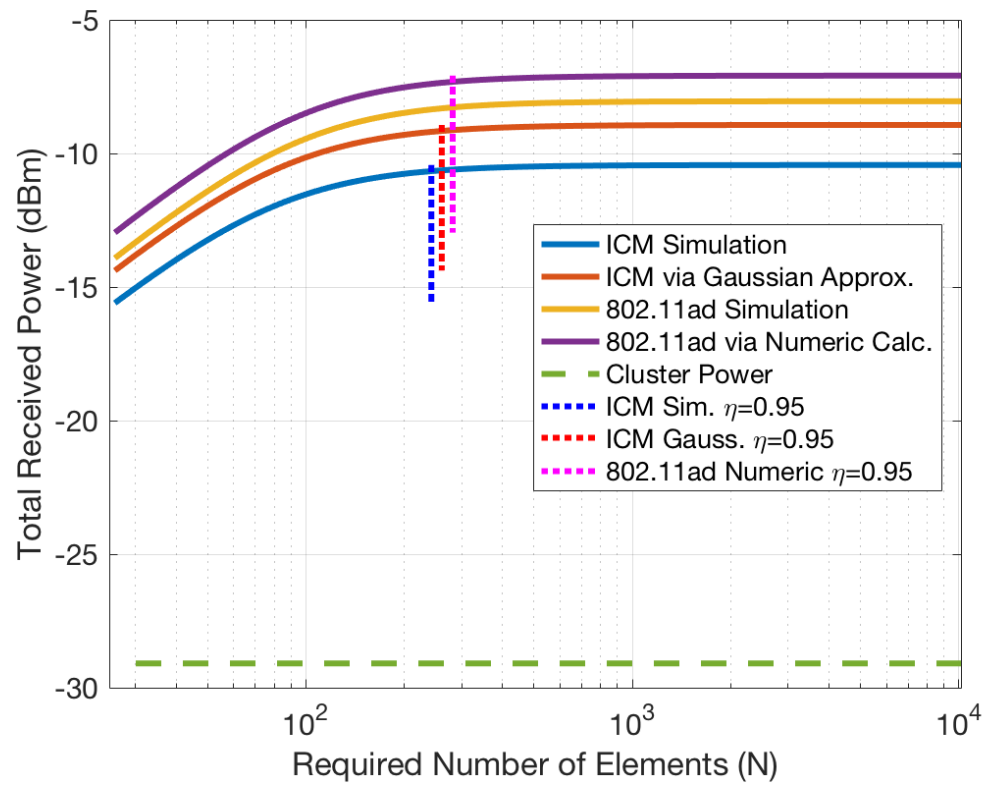


Figure 6.6: Total received power versus number of elements.

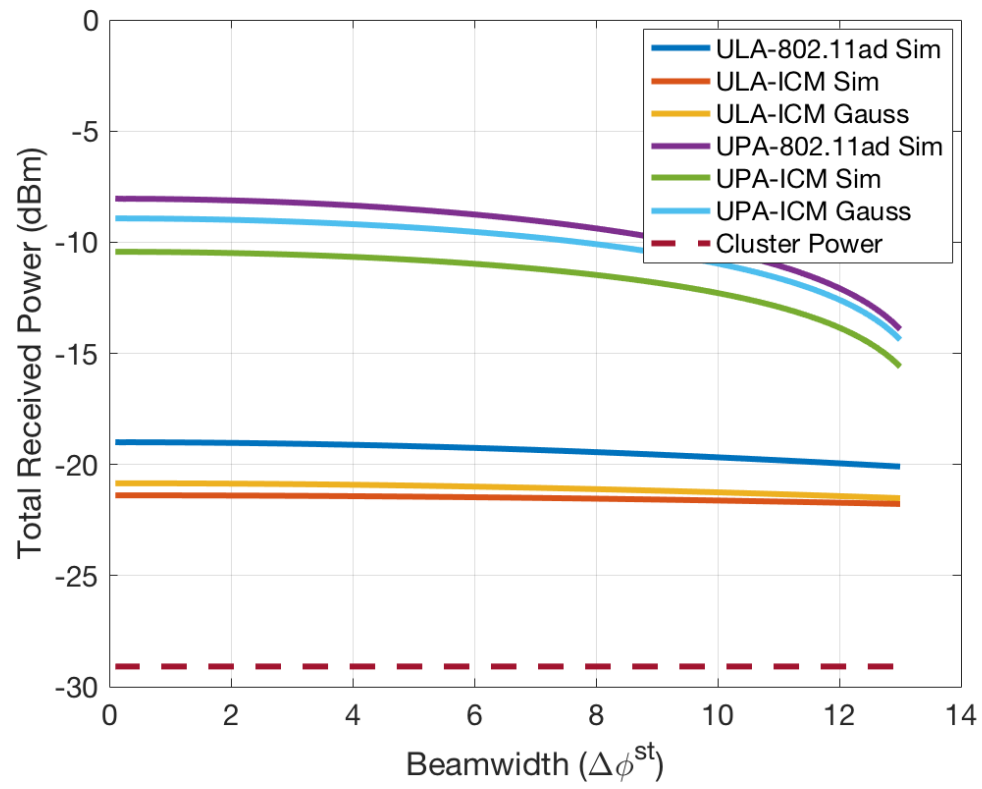


Figure 6.7: ULA and UPA comparison for the same case study.

Chapter 7

Varying the Beamwidth of Hybrid Beamforming

In the previous two chapters, we optimized the beamwidth with respect to the channel power angle profile such that the received power is maximized. However, an arbitrary beamwidth value cannot be achieved in the practical world due to the several limitations such as finite and fixed number of phase shifters, complexity in the receiver, etc. In this chapter, we discuss beamwidth variation flexibilities in a hybrid beamforming structure where hybrid beamforming is used both for channel estimation and beamforming.

Availability of large array usage in millimeter wave communications gives the opportunity to create narrow beams that yield to high antenna gains. However, in some cases, wider beams are of interest (as we have seen in the previous chapters) in order to increase the coverage area or reduce the outages caused by the channel variations. To address this need, beam broadening approaches with no increase in the hardware complexity have been described without studying the implementation difficulties. This chapter proposes a simplified broadening model while adopting a strategy in which neighbor beams are concatenated to create a wider beam dividing the antenna into subarrays. The beamwidth and power loss analysis along with the beam broadening bounds in the design parameters are expressed in detail. Next, introduced broadening model is integrated to the hybrid beamforming system without changing its hardware structure. Simulation results that verify the analytical expressions for both broadening system and its hybrid beamforming implementation are provided.

7.1 Motivation

Thanks to the usage availability of large arrays, mm-Wave communication promises gigabit-per-second data rates and increased spectral efficiency as benefiting from multi-input-multi-output (MIMO) structure. The most significant downside of increased path loss at higher frequencies is expected to be tolerated with increasing antenna gains by performing beamforming (BF) both at the receiver and the transmitter. Although BF can be utilized with several types of antennas, primary selection in mm-Wave is the array antennas due to the opportunity of their very low-size packaging. To increase the antenna gain and reduce the interference, researchers aim to accomplish narrower beams with small half-power beam width (HPBW) which is inversely proportional to the array size, i.e. the number of antenna elements in the array. However, measurements show for some scenarios that wider beams are of interest for a beamformed link [38]. In fact, an optimum beamwidth analysis is proposed in the previous chapters but the challenges in the implementation are still an open research area.

On the other hand, hybrid beamforming has been proposed in [63] that addresses critical mmWave constraints by dividing the beamforming process at the transmitter into two level, namely, baseband and RF precoding. While RF precoding accomplishes a coarse projection to the estimated direction using analog phase shifters, baseband precoding fine-tunes the direction and allows the multi-stream transmission using conventional digital MIMO precoding. The design of these two operation matrices are studied as an optimization problem, and the results showed that the method almost catches the theoretical spectral efficiency limits [4]. Taking one step further, [64] realizes an analytical approach to use the same hybrid BF mechanism, first, to estimate the channel in an iterative way using a codebook and then perform a beamforming approximation based on the estimated channel. However, none of the studies discuss any effect of the beamwidth constraint of hybrid systems that strictly depends on the number of antennas.

There exist solutions to provide wider beams for control and broadcast communications [65, 66, 71, 75] but their focus is on creating efficient codebooks that are used in

the initial beamforming stage. [67, 68] proposed phase-only beam broadening without giving a systematic approach that takes mm-Wave BF systems into account. [69] gives a clear beam broadening application for mm-Wave systems but it doesn't discuss the implementation challenges. Furthermore, the proposed method is hard to replicate in practice as it omits elaborating some theoretical assumptions. To the best knowledge of the authors, beamwidth flexibility problem of a hybrid mmWave beamforming system without changing the number of antenna elements is never studied although its apparent necessity.

In this chapter, we create a simple broadening method with a detailed analysis and propose an implementation algorithm of the method to a mmWave hybrid beamforming system which is used for both channel estimation and beam training. We will first elaborate the implementation challenges of the method proposed in [69] although generic approach suits well for any type of phased array antenna systems. And then, instead of handling the difficulties to develop its method, a simpler broadening system is proposed. Finally, that approach is implemented directly to the hybrid BF without changing the structure. We show in the simulation results that the proposed method doesn't degrade the channel estimation performance of the hybrid system while releasing the fixed beamwidth constraint in the beamforming stage. The method we proposed gives insights to the adaptive beamwidth approach during the data transmission for independent different beams within the same MIMO channel.

The chapter is organized as follows. Section 7.2 gives the challenges of varying the beamwidth for hybrid systems. Section 7.3 gives the antenna system setup and the problem formulation for beam broadening. Section 7.4 analyzes the resultant beamwidth and power loss. Section 7.5 discusses the implementation of formulated beam broadening to the hybrid BF. Finally, the simulation results are given in Section 7.6.

7.2 Challenges for Beamwidth Flexibility

While hybrid beamforming removes several practical constraints providing a low-complexity design, the system still comes with limitations due to the dependency of limited/perfect

channel knowledge at the receiver. The algorithm given in [4] requires initial optimum RF precoding vectors as an input in order to project the quantized beams onto the desired direction. In [4, 63, 64, 70], left eigenvectors of the channel matrix are used to initialize the precoding algorithm. In particular, [64, 70] uses the same hybrid BF design to both estimate the channel and perform beam training. The adopted approach in those systems is to narrow the beams as much as possible in the channel estimation stage to increase the resolution. Since, they use the same array for beamforming, resultant beam in the beamformed link will have a narrow beamwidth which may be not desired for some scenarios such as rapidly changing channels. Clearly, this creates a conflict in the design.

As the beamwidth is inversely proportional to the array size, turning some part of the array off can be an option to create wider beams in the beamforming stage but it requires a new singular vector set for beam tracking¹ as the size of the vectors would change. Apparently, changing the number of antennas degrades the performance of the channel estimation. As a result, an algorithm is needed to provide a broadening in the radiated beam during data transmission but without changing the structure of the system so that not affecting the channel estimation performance.

One way to overcome the mentioned problem, instead of using the eigenvectors of the estimated channel, a new set of initialization vectors can be constructed based on the estimated angle of arrival/departure (AoA/AoD). Since the initialization vector can be considered basically as the ideal weights of the RF precoding array, a broadening algorithm may run to construct a new set of ideal weights before beamforming approximation performs.

The approach in [69] fits well to that need. However, it focuses on the resultant array factor rather than discussing the parameters such as the antenna weights, corresponding array response vectors, power loss caused by broadening, etc. Further, an important effect regarding the steering is neglected which has to be elaborated. As a result, since the implementation of the algorithm that [69] proposes is complex, a simplified design

¹For most of the applications, beam tracking is accomplished during the data transmission. It is basically a channel estimation.

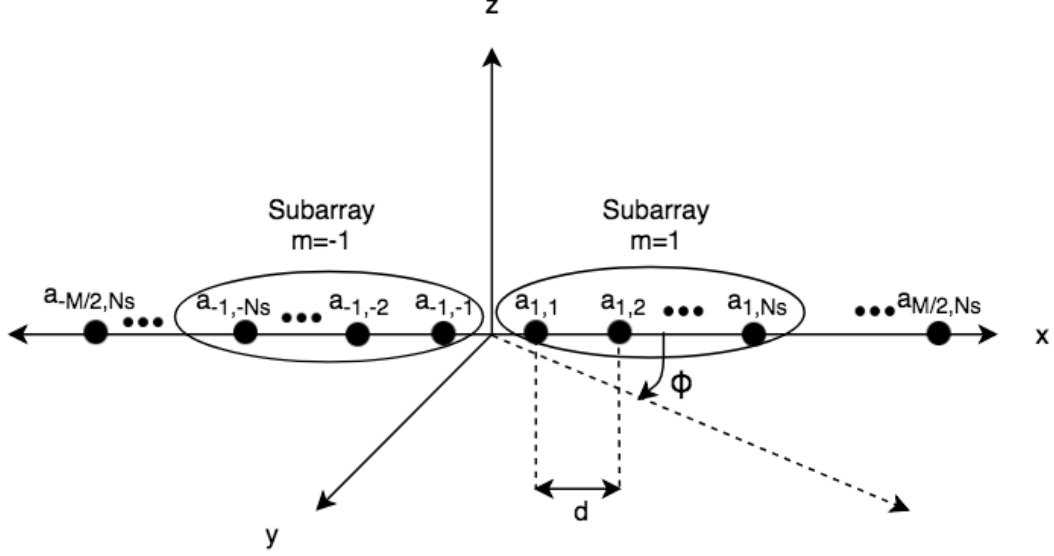


Figure 7.1: Symmetric array design for the simplified model.

with an improved and detailed analysis is introduced in this chapter while adopting the same phase-only beam broadening approach.

7.3 Beam Broadening

7.3.1 Signal Model

For a simplified modeling, proposed array design is given in Fig. 7.1. We consider a uniform linear array (ULA) on the x -axis with $N = MxN_s$ isotropic elements, where M is the number of subarrays and N_s is the number of elements in each subarray. While we adopt the same notation in [69], note that the antenna array model is changed to the symmetric design to remove the phase shift residual that occurs in the resultant array factor. We force N to be even for now. For this system, array response vector (at 90° elevation angle) and the corresponding array weights are given as following [27]:

$$\mathbf{a}_{ULA}(\psi) = \frac{1}{\sqrt{N}} [e^{-j(\frac{N-1}{2})\psi}, e^{-j(\frac{N-1}{2}-1)\psi}, \dots, e^{-j\frac{1}{2}\psi},$$

$$e^{j\frac{1}{2}\psi}, \dots, e^{j(\frac{N-1}{2}-1)\psi}, e^{j(\frac{N-1}{2})\psi}], \quad (7.1)$$

$$\mathbf{a}_w = [a_{\frac{-M}{2}, -N_s}, a_{\frac{-M}{2}, -(N_s-1)}, \dots, a_{-1, -1}, \\ a_{1, 1}, \dots, a_{\frac{M}{2}, N_s}], \quad (7.2)$$

where $\psi = kd \cos(\phi)$ is the digital wavenumber of the angle space in radians. Here $0^\circ < \phi < 180^\circ$ is the azimuthal angle that the array can steer over, $k = 2\pi/\lambda$ and d is the element spacing. We assume $d = \lambda/2$ throughout the chapter where λ is the wavelength. With that set of definition, the visible region in ψ -space is $-\pi < \psi < \pi$.

The resultant array factor can be written as:

$$A(\psi) = \frac{1}{\sqrt{N}} \sum_{m=1}^{M/2} \sum_{n=1}^{N_s} [a_{m,n} e^{j((m-1)N_s + n - \frac{1}{2})\psi} + \\ a_{-m, -n} e^{-j((m-1)N_s + n - \frac{1}{2})\psi}]. \quad (7.3)$$

Note that the total array factor is the composition of individual subarray factors, namely, $A(\psi) = A_1(\psi) + A_2(\psi) + \dots + A_{M/2}$ where each subarray factor is given as:

$$A_m(\psi) = \frac{1}{\sqrt{N}} \sum_{n=1}^{N_s} [a_{m,n} e^{j((m-1)N_s + n - \frac{1}{2})\psi} + \\ a_{-m, -n} e^{-j((m-1)N_s + n - \frac{1}{2})\psi}].$$

7.3.2 Beam Broadening at Broadside

In this subsection, we briefly explain the beam broadening approach given in [69]. Additionally, we provide the required weights to create the desired array factor at broadside.

Let $a_{m,n} = a_{-m, -n}$ and plug into the Eq. (7.3),

$$A(\psi) = \frac{2}{\sqrt{N}} \sum_{m=1}^{M/2} \sum_{n=1}^{N_s} a_{m,n} \cos(((m-1)N_s + n - 1/2)\psi). \quad (7.4)$$

Apparently, no matter what the weights are set to, summation of cosines in Eq. (7.4) implies that the resultant array factor is always symmetric. Moreover, recalling

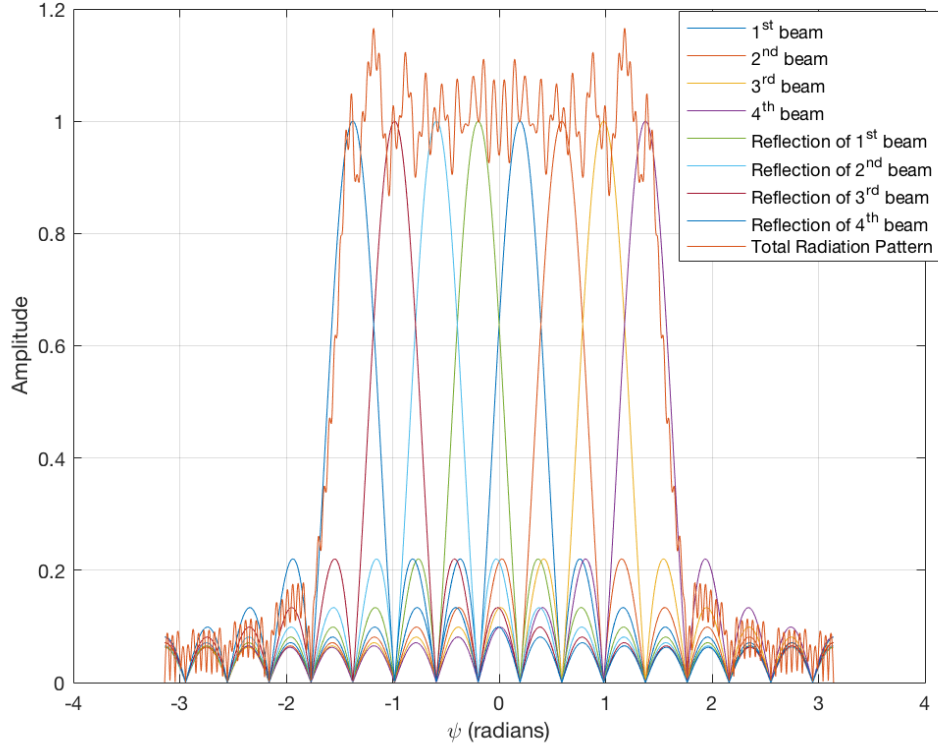


Figure 7.2: Resultant subarray and total radiation pattern for $N=128$, $M=8$.

that $-\pi < \psi < \pi$, nulls of the radiation pattern of Eq. (7.4) for equal weights are at $2b\pi/N$ where $b = 1, 2, \dots, N-1$ [27]. Placing each subarray beam direction, say ψ_m , to the nulls of each other will result an almost flat broadened beam. To do so, as [69] proposes, we place the subarray beams to the following directions in ψ -space:

$$\psi_m = \frac{(2(m-1) + 1)\pi}{N_s}, \quad m = 1, 2, \dots, M/2, \quad (7.5)$$

which corresponds to setting the antenna weights as:

$$a_{m,n} = e^{-j\psi_m((m-1)N_s + n - 1/2)}. \quad (7.6)$$

Notice that the Eq. (7.4) is the simpler form of Eq. (10) in [69] while providing a symmetric array response for any set of weights. More importantly, Eq. (7.6) suggests direct computation of weights, whereas [69] only provides the array factor which requires

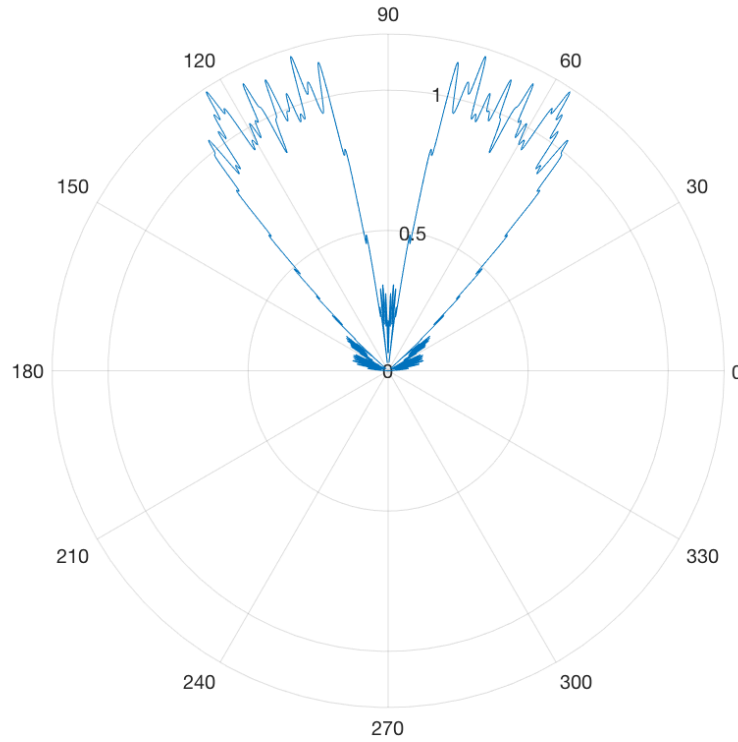


Figure 7.3: Split effect of keeping the weights flipped on steering for $N=128$, $M=8$.

another step to calculate the weights using an additional digital processing unit. To make an intuitive approach, while the right-side elements, $a_{m,n}$, create beams at ψ_m , the left-side elements, $a_{-m,-n}$, will be symmetric of that (i.e. $-\psi_m$) because of the reverse rotation effect comes from the array response vector in Eq. (7.1). The resultant array factor along with the separate subarray beams and the rotation effect of the array response vector can be seen in Fig. 7.2 for $N = 128$, $M = 8$.

7.3.3 Steering the Broadened Beam

To steer the broadened beam to a desired direction ψ_{des} , we need to approach carefully to the weights as the system works now as a multibeam array. Assume we want to steer the array to $\phi_0 = 80^\circ$, that is $\psi_{des} = kd \cos \phi_0$. For a conventional phase translation, new right-side antenna weights are defined as following:

$$a'_{m,n} = a_{m,n} e^{-j\psi_{des}((m-1)N_s+n-1/2)}, \quad (7.7)$$

where $a_{m,n}$ are given in Eq. (7.6). Since the left-side elements just mirror the radiation pattern that right-side elements create, multiplying the whole array progressively with a simple phase shift would result the broadened beam split into two half-broadened beams. This effect is shown in Fig. 7.3 in angle space (ϕ) with the same configuration in Fig. 7.2. Note that Eq. (7.7) creates only the 10° clock-wise shifted half-broadened beam while $a'_{-m,-n} = a'_{m,n}$ creates the other half. This important effect was omitted in [69].

In order to steer the broadened beam at broadside without changing the antenna design given in Fig. 7.1, flipping convenience should be sacrificed. That is, the flipped weights on broadside $a_{-m,-n}$ must be multiplied with the negative phase-shift that steers the beam clock-wise. Then the new left-side antenna weights are:

$$a'_{-m,-n} = a_{-m,-n} e^{j\psi_{des}((m-1)N_s+n-1/2)}. \quad (7.8)$$

Replacing the weights in Eq. (7.3) with (7.7) and (7.8), array factor for steered broadened beam is defined as:

$$\begin{aligned} A'(\psi) &= \frac{2}{\sqrt{N}} \sum_{m=1}^{M/2} \sum_{n=1}^{N_s} a_{m,n} \cos(((m-1)N_s + n - 1/2)(\psi - \psi_{des})) \\ &= A(\psi - \psi_{des}). \end{aligned} \quad (7.9)$$

The resultant array response in ϕ -space is given in Fig. 7.4. Keeping the array response vector given in Eq. (7.1) same, the new weights are:

$$\mathbf{a}'_w = [flip(a'_{-m,-n}), a'_{m,n}], \quad (7.10)$$

where $flip(\cdot)$ function flips the vector to ensure the symmetry.

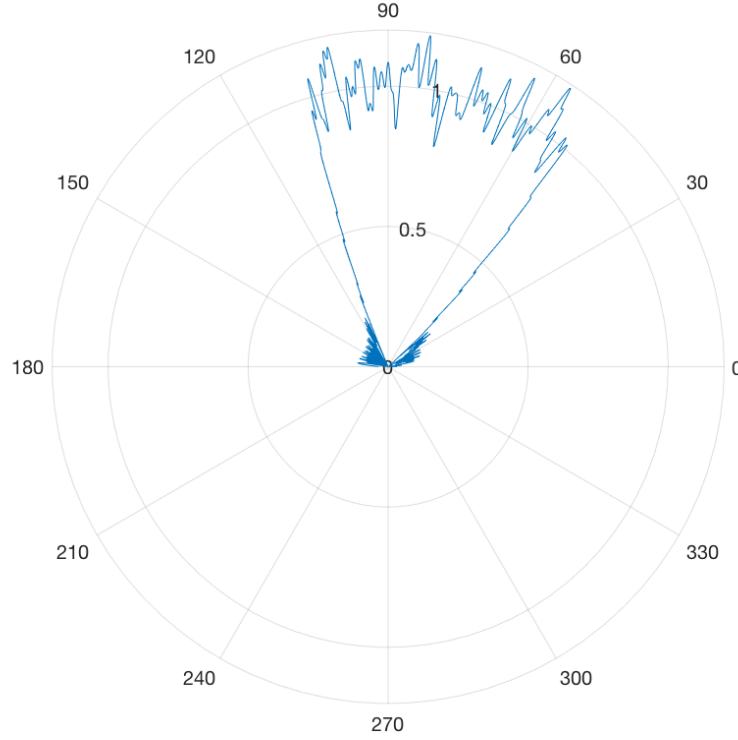


Figure 7.4: Broadened and steered beam (to $\phi_0 = 80^\circ$) for $N=128$, $M=8$.

7.4 Beamwidth and Power Loss Analysis

In this section, we give the expressions for the beamwidth and the gain of the broadened beam under some design assumptions with respect to the narrowest beam that the array can create. While the broadened beamwidth is provided in [69], we give the derivation of the power loss here.

7.4.1 Beamwidth

From [27], HPBW (in degrees) can be expressed for N -elements array as:

$$\Delta\phi_{3dB} = \frac{50.76^\circ}{\sin \phi_0} \frac{\lambda}{Nd}. \quad (7.11)$$

Since each subarray beam enlarges the beamwidth by M , and there are M of those subarray beams as seen in Fig.7.2, HPBW of the broadened beam for M is [69]:

$$\Delta\phi_{3dB}^B = M^2\Delta\phi_{3dB}. \quad (7.12)$$

7.4.2 Power Loss

Under the total power constraint of the array, power loss is the trade-off that comes with broadening the beam. The general assumption for power constraints at phase shifters in hybrid BF systems is [4, 64]:

$$(\mathbf{F}_{RF}^{(i)}\mathbf{F}_{RF}^{(i)*})_{\ell,\ell} = N^{-1}, \quad (7.13)$$

where $\mathbf{F}_{RF}^{(i)}$ is the i -th column vector of the \mathbf{F}_{RF} , RF precoding matrix. The sub-index (ℓ, ℓ) represents the diagonal elements of the resultant matrix. Eq. (7.13) states that the power on each weight in the array kept as $1/N$ so that the transmit power (P) doesn't change. For convenience, let us assume $P = 1$.

In spatial domain, one should integrate the square of the resultant array factor (Eq. (7.9)) to be able to get the true directivity (or gain) of the broadened beam. Due to our limited space, we leave this as a future work and consider the rough computation of the area under the beamwidth as following. The total power under the main lobe is $P_T = P\Delta\phi_{3dB} = \Delta\phi_{3dB}$. Since the total power, P_T , doesn't change, peak power level for broadened beam is defined as

$$P^B = P_T/\Delta\phi_{3dB}^B = 1/M^2, \quad (7.14)$$

$$P_{dB}^B = -20\log_{10} M, \quad (7.15)$$

where Eq. (7.14) results from Eq. (7.12) and Eq. (7.15) shows the relation in dB-scale.

7.4.3 Broadening Bounds

Although a beam broadening mechanism is given in previous sections, the amount of broadening and its scale are dependent on the M and N values. That is, broadening can

be utilized for only multiples of the narrowest beam that the whole array can reach, as seen in Eq. (7.12). That quantization constraint limits the number of possible broadened beams and the maximum broadening amount which is not addressed in [69]. For our specific design ($d = \lambda/2$), Eq. (7.11) states that a whole array can reach to the following HPBW at broadside ($\phi_0 = 90^\circ$):

$$\Delta\phi_{3dB} = \frac{101.52^\circ}{N}. \quad (7.16)$$

Recalling that $0^\circ < \phi < 180^\circ$, broadened beamwidth can be 180° at maximum. From Eq. (7.12),

$$M^2 \frac{101.52^\circ}{N} \leq 180^\circ, \quad (7.17)$$

$$M^2/N \leq 1.77.$$

On the other hand, since the broadening system uses all the elements, M must divide N , i.e., $N \bmod M = 0$. Finally, M must be multiples of 2 to ensure the symmetricity.

7.5 Implementation to Hybrid BF Systems

Hybrid BF can be used both to estimate the channel parameters and to beamform [64, 70]. However, since estimating the channel is a separate process that uses the same hybrid beamforming algorithm, implementation of broadening becomes a challenge. Although the algorithm given in [64] doesn't depend on the type of array response vector, we use Eq. (7.1) (symmetric ULA design) for the beamforming process as the broadening weights are calculated correspondingly.

We keep the same geometric channel model. Assuming that both receiver and transmitter have the same number of antenna elements, N , the channel matrix is defined as

$$\mathbf{H} = \frac{N}{\sqrt{\rho}} \sum_{\ell=1}^L \alpha_\ell \mathbf{a}_{MS}(\theta_\ell) \mathbf{a}_{BS}^H(\phi_\ell), \quad (7.18)$$

where ρ is the average path loss. $|\alpha_\ell|$ is the Rayleigh distributed gain of the ℓ -th path where $\ell = 1, 2, \dots, L$. Finally, $\theta_\ell, \phi_\ell \in [0, \pi]$ are the angle-of-arrival/departure (AoA/AoD) for the ℓ -th path and the $\mathbf{a}_{MS}(\theta_\ell), \mathbf{a}_{BS}(\phi_\ell)$ are array response vectors given in Eq. (7.1) for mobile station (MS) and base station (BS), respectively.

7.5.1 Challenge with Channel Estimation

Algorithm in [64] works as follows for a MIMO system: (i) Using the codebook that the paper proposes, hybrid system estimates the $\hat{\alpha}_\ell$ and $\hat{\phi}_\ell$ iteratively while narrowing its beamwidth further in every iteration, similar to [75]. (ii) Estimated channel matrix, $\hat{\mathbf{H}}$, is constructed using the defined geometric channel model while approximating array response vector too as quantizing ϕ_ℓ . (iii) Taking the singular-value-decomposition (SVD) of $\hat{\mathbf{H}}$, left and right eigenvector matrices, $\hat{\mathbf{U}}$ and $\hat{\mathbf{V}}$, are used to initialize the beamforming process at receiver and transmitter. Hence the approximation of the estimated direction is performed by the hybrid BF system based on the SVD of the estimated channel. However, the ideal weights that $\hat{\mathbf{V}}$ imposes force the antenna steer to a certain direction. Reducing the number of antennas to widen the HPBW creates the dimension incompatibility problem with $\hat{\mathbf{V}}$. On the other hand, manipulation of $\hat{\mathbf{V}}$ changes the channel structure.

One must be careful while changing the structure of the hybrid design to add the broadening feature to the beam approximation operation. Considering the fact that the perfect channel estimation requires the beams to be as narrow as possible which conflicts the nature of beam broadening, changing the hybrid design parameters such as the number of RF chains, the number of antennas in usage, etc. are highly limited.

7.5.2 Updated Algorithm

Instead of using the estimated channel $\hat{\mathbf{H}}$ to obtain input optimum weights ($\hat{\mathbf{V}}$) to the hybrid BF algorithm, we propose to run the broadening algorithm on the estimated AoDs, i.e. setting $\psi_{des}^\ell = kd \cos \hat{\phi}_\ell$.

Then the new algorithm is: (i) Estimate $\hat{\alpha}_\ell$ and $\hat{\phi}_\ell$. (ii) Run the broadening algorithm using $\hat{\phi}_\ell$ and output the optimum weights, \mathbf{a}'_w , given in Eq.(7.10). (iii) Using

Table 7.1: Simulation Parameters

Parameter	Description
Frequency	28 GHz
Distance	10-30 meters
Path loss component (n)	2 (LOS)
SNR	-20 dB
Number of paths (L)	1
Resolution for Channel Estimation (CE)	512
Number of Measurements for CE	2

the weights as input, initialize the hybrid BF algorithm.

Note that this approach doesn't require any change in hardware design. What the method proposes is just to alter the input optimum weights (\mathbf{F}_{opt} , or $\hat{\mathbf{V}}$) that was estimated by the channel estimation algorithm. The only limitation comes with the subarray modeling is to keep M lower than the number of RF chains (i.e. $M < N_{RF}$) in order to allow controlling the phase-shifts of every subarray individually.

7.6 Simulation Results

In this section, we simulate the integration of proposed beam broadening model defined in Section 7.3 to the hybrid precoding system based on the updated algorithm in Section 7.5. We use MATLAB to realize the simulations.

Fig. 7.5 displays the narrowest beam that a hybrid precoder with $N = 128$ elements array creates along with its broadened beams for $M = 2, 4, 8$. From Eq. (7.11) and (7.12), $\Delta\phi_{3dB} = 0.79^\circ$, $\Delta\phi_{3dB}^{B=2} = 3.17^\circ$, $\Delta\phi_{3dB}^{B=4} = 12.69^\circ$ and $\Delta\phi_{3dB}^{B=8} = 50.79^\circ$. In ψ -space, those values convert to 0.04, 0.17, 0.70 and 2.78 radians [27], respectively, as seen in Fig. 7.5. Note that, while the HPBW increases, the ripples at the main lobes are still within 3 dB, and the relative side lobe levels are approximately same for all, i.e. ≈ -13 dB. Assuming the maximum array gain is normalized to 0 dBi, power levels are calculated from Eq. (7.15) as -6.02 dBi for $M = 2$, -12.04 dBi for $M = 4$ and -18.06 dBi for $M = 8$ which can be verified also from Fig. 7.5.

In order to demonstrate that the broadening system doesn't degrade the channel

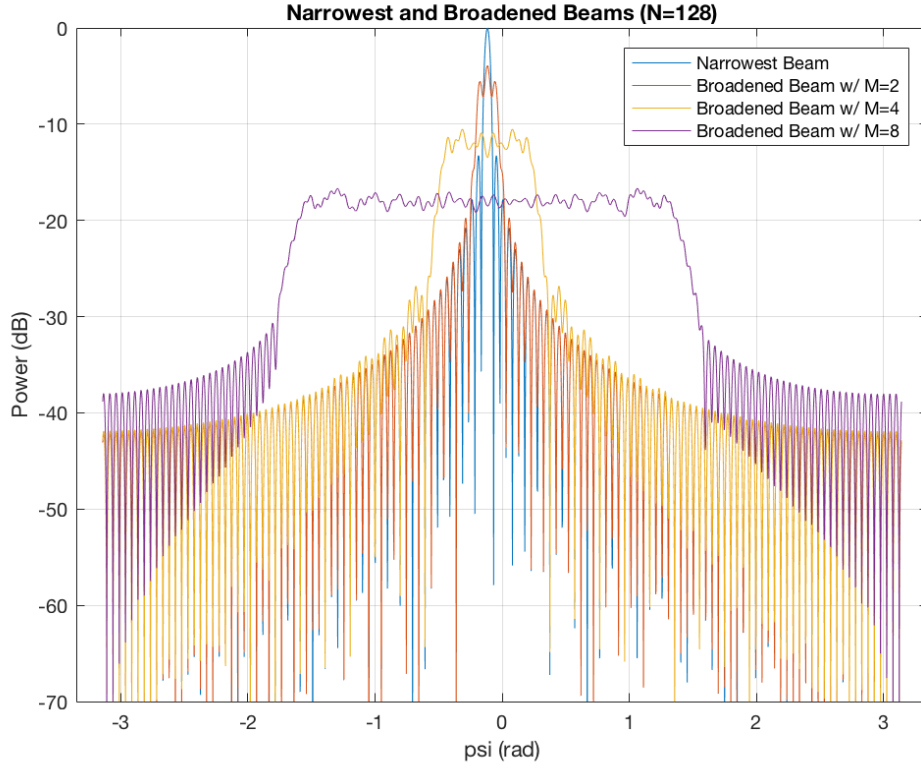


Figure 7.5: Narrowest and broadened beams for $N=128$, $M=2, 4, 8$ at $\phi_0 = 92^\circ$.

estimation performance, we set up a complete downlink including a receiver with an isotropic antenna using the similar channel estimation parameters in [64]. Table 7.1 summarizes the important parameters in the estimation stage. These are selected as such to replicate a typical cellular communication link.

In Fig. 7.6, we demonstrate that the channel estimation performance is not affected due to the antenna subarray modeling. The optimum beam is displayed based on the real AoD whereas the estimated beam is on estimated AoD. After estimation, hybrid precoding runs for broadening the beam by $M = 8$. Fig. 7.6 verifies that the integration of subarray modeling and the broadening algorithm don't affect the estimation process. In fact, in case of even a little AoD estimation error, narrower beams resulted from the hybrid precoding would cause outage whereas it can be tolerated with the flexibility in the beamwidth at precoding stage. It turns out that it is desirable to have N as large as possible at channel estimation process where very narrow beams are required to resolve the channel spatially. On the other hand, beamwidth flexibility at precoding

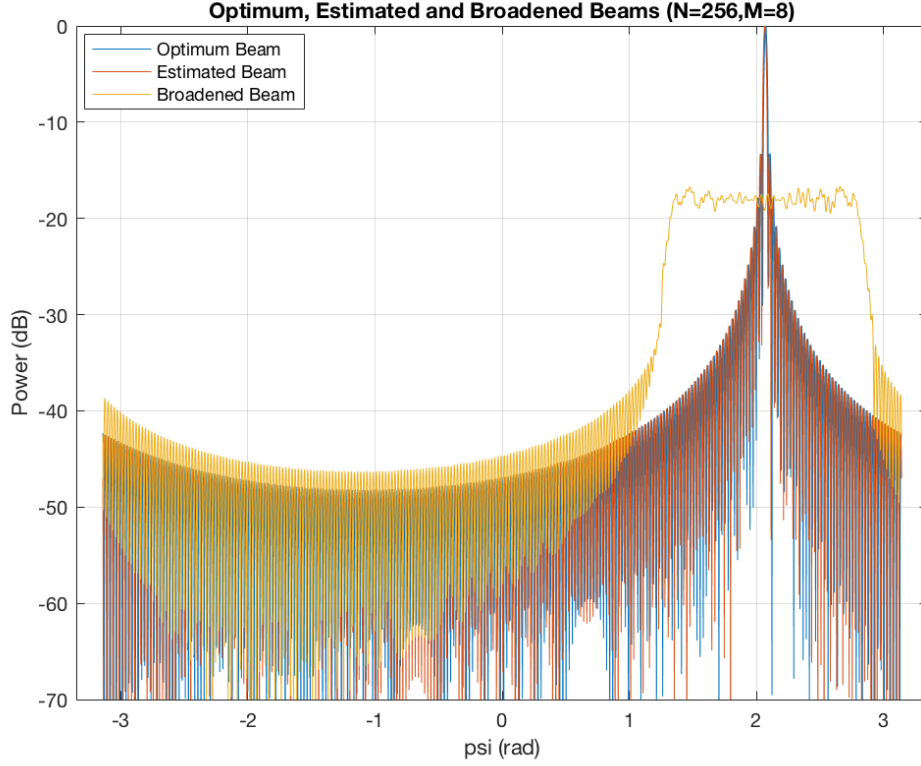


Figure 7.6: Estimated optimum and broadened beam for $N=256$, $M=8$ at $\phi_0 = 47^\circ$.

stage increases the capacity of the channel. To see that, let us consider the case in Fig. 7.6 where the beamwidth of the optimum beam is 0.54° degrees. Defining that an outage happens when user drops out of the HPBW of the main lobe, this result suggests that if at least 0.27° estimation error occurs, user becomes out of coverage. It, further, gets more sensitive when user is in the broadside, because the HPBW reduces to 0.39° due to the $\sin \phi$ term in the denominator in Eq.(7.11).

It is worthy to note that $N = 256$ in Fig. 7.6 have the same main lobe power (0 dBi) with the case of $N = 128$ in Fig. 7.5 due to the normalization of the maximum array gain. In fact, beamforming gain (BG) is calculated roughly to be 24 dBi for the former, while 21 dBi for the latter based on $BG = 10 \log_{10} N$ [27]. Also, notice that the HPBW of broadened beams for $M = 8$ are significantly different which suggests that the algorithm is not performed based on the desired amount of broadening rather it broadens with the multiples of the narrowest beam.

Finally, Fig. 7.7 shows the throughput change comparison with respect to drift for

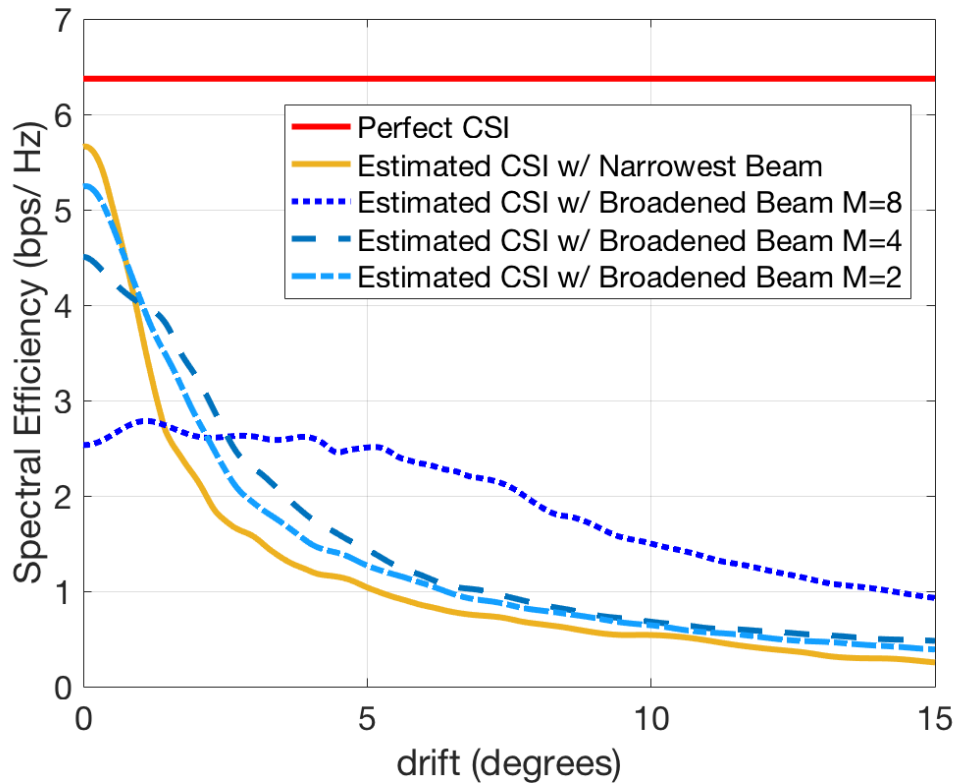


Figure 7.7: Spectral efficiency comparison while drift occurs after channel estimation.

several cases. Here, drift is defined as the cluster angle difference that occurs after channel estimation. In practice, this may occur when (1) either receiver or transmitter moves after the channel estimation, (2) imperfection in channel estimation, (3) imperfection in beamforming. Thus, drift can also be thought as the amount of misalignment at beamforming. As figure shows, while beams with narrow beamwidth are too sensitive to the drift, throughput becomes more durable to it once beams are getting wider.

7.7 Conclusion

In this chapter, we design a detailed broadening algorithm to be integrated into hybrid beamforming systems. We show that symmetric antenna modeling simplifies the broadening approach and fits well to the hybrid beamforming as well. Beamwidth and power loss analysis of the method are described and then bounds on the model parameters are elaborated. Further, the proposed approach is shown to not degrade the

system performance where hybrid precoding is used to estimate the channel and then to beamform. For future work, based on the channel variations, an algorithm can be created to track the required HPBW as broadening the beam adaptively.

Part III

Efficient Beamforming Algorithms

Chapter 8

Binary Search and Linear Search

In the previous chapters, we inquire the optimum receiver front-end design parameters for PHY layer efficiency of beamforming (BF) at mmWave channels including the effects of propagation mechanisms within the channel. In this chapter, we study the key parameters of beamforming that affect MAC performance. Specifically, beamforming protocols introduced in IEEE 802.11ad and IEEE 802.15.3c for 60 GHz communications perform exhaustive sector/beam search to setup a beamformed link between stations/devices. In this chapter, we propose two BF methods, Binary Search Beamforming (BSB) and Linear Search Beamforming (LSB) [2], to improve the BF setup time of adopted algorithms in IEEE 802.11ad and IEEE 802.15.3c.

8.1 Motivation

In [73], two-level BF training which is also used in IEEE 802.11ad has been described. It basically consists sector-level training and refinement stages. On the other hand, the protocol proposed by Wang [74] and adopted with slight changes in IEEE 802.15.3c pairs the optimal beams in a 3-level training process, namely; quasi-omni level, sector-level and beam-level training. Both BF algorithms are MAC level protocols and are using stage system in order to reduce exhaustive search BF setup time as a primary goal. However, despite stage system adoption, practically exhaustive searching mechanisms are still performed for each level-training in both standard BF protocols. For example, for sector-level transmit training in IEEE 802.11ad, transmitter station needs to send frames from its each sector to let the receiver station determine the optimal one in terms of received highest SNR. That means, for a transmitter antenna with 64 sectors, there should be a remarkable length waiting period for 64 frames transmitted from each

sector.

This chapter proposes adaptations of two fundamental fast searching algorithms used in data structures, binary search and linear search, to BF systems introduced in IEEE 802.11ad and IEEE 802.15.3c. Relying on the fact that 60GHz communication is efficient mostly for LOS environments [10] and assuming first and second order reflections from walls reach receiver always with less SNR than of the LOS ray (because distance will be always greater in the NLOS environment), proposed methods suggest ignoring the "far" sectors directly without sending a frame by applying searching algorithms. Suggested searching methods can be directly applied as Sector Sweep Level (SLS) phase in IEEE 802.11ad and as sector-level training phase (as well as beam-level training phase) in IEEE 802.15.3c. Proposed algorithms reduce the steps in training and, hence, the BF setup time. In addition, they save power by reducing the number of frames to be sent. For BSB, the advantages are gained at the expense of an increase in the error probability due to false sector pairing, in certain cases.

8.2 Current Beamforming Protocols

In this section, we explain the general mechanism of BF protocols introduced in the IEEE 802.11ad and the IEEE 802.15.3c standards. Briefly, only one phase for each standard is discussed in detail.

8.2.1 Beamforming in the IEEE 802.11ad

BF is completed in two main phases in IEEE 802.11ad. While sector based pairing is performed in mandatory SLS phase, optional beam level fine-tuning operation follows in Beam Refinement Protocol (BRP) phase. Protocol in the SLS phase proceeds as following.

Two stations intended to communicate each other decide beamforming either their transmitting or receiving sectors. IEEE 802.11ad defines two new terms, initiator, and responder, to identify the stations initiates the beamforming and responds to it, respectively. Assuming stations agree to train their transmit sectors, in the first step of

SLS, initiator station transmits unique frames from its each sector as tagging each frame with corresponding sector ID. This sub-phase is called Initiator Sector Sweep (ISS). During ISS, responder keeps its receiver in the quasi-omni antenna pattern and measures the SNR of each received frame. In the next sub-phase of SLS, called Responder Sector Sweep (RSS), now responder transmits frames from its each sector by assigning an FB information to each frame. Specifically, that FB is the best sector ID of initiator in terms of SNR. During the RSS, initiator listens in the quasi-omni antenna pattern. In the next sub-phase, Sector Sweep Feedback (SSW-F), initiator sends just one frame as the FB of best sector of responder transmitter. Initiator transmits this frame from its best sector determined in the RSS phase. Lastly, an acknowledgement frame is sent by the responder from its best sector which forms the SSW Acknowledgement (SSW-ACK) sub-phase.

At the end of SLS phase, both initiator and responder stations know their best transmitting sectors for their future communications. If they decide to train their receiving sectors as well and fine-tune the determined transmit sectors in the beam level, they simply initiate BRP phase.

8.2.2 Beamforming in the IEEE 802.15.3c

IEEE 802.15.3c introduces a different BF protocol, although both standards agree with the two level training system. It is worthy to note that although three level searching mechanism is proposed in [74], IEEE 802.15.3c ignores the first stage of device-to-device linking (quasi-omni pattern pairing) in the beamforming clause.

In sector level searching, Device (DEV) 1 and DEV2 pair their best (in terms of SINR) transmitting and receiving sectors within four sub-phases; i.e. sector training, sector feedback, sector to beam mapping, acknowledgement. In the first part of sector training sub-phase, DEV1 transmits training sequences to DEV2 from its each sector. The significant difference from IEEE 802.11ad is here DEV1 sends a number of sequences from its each sector rather than just one frame. Each sequence is received by a different receive sector of DEV2, so the number of sequences is equal to the number of receiving sectors of DEV2. That process is called *cycle* in the standard. The number

of cycles during DEV1 to DEV2 sector training is equal to the number of transmitting sectors of DEV1. In the second part of sector training, DEVs exchange the roles and DEV2 to DEV1 sector training takes place. Since both DEVs know their best receiving sector and other DEV's best transmitting sector at the end of this sub-phase, they simply share this information with each other in the sector feedback sub-phase. In the first part of this sub-phase, DEV1 transmits the FB information from its each transmitting sectors, since DEV1 still doesn't know its best transmitting sector. DEV2 receives each frame from its best receiving sector. In the second part, DEV2 sends only a unique frame from its best transmitting sector and DEV1 receives it by its best receiving sector.

At the end of sector feedback training stage, both DEVs know their optimal transmit and receive sectors. In the mapping and acknowledgement stages, DEVs acknowledge their updated situation and share the information regarding the further beam-level searching. After that, they initiate the beam level searching phase by zooming the selected sectors.

Comparing the IEEE 802.11ad and the IEEE 802.15.3c BF algorithms, the most important difference is, while only transmit (or receive) sectors of both stations are beamformed at the end of the protocol in the former; in the latter, both DEVs are beamformed on their both receive and transmit sectors. It should also be emphasized that in IEEE 802.15.3c, BF is optional. On the other hand, it is mandatory in IEEE 802.11ad.

8.3 Proposed Algorithms

As described in the previous section, in the first phase of beamforming, both stations/devices exchange frames/sequences using their *all* sectors. However, considering the path loss is the dominant power degradation factor in 60GHz band communication, it has been shown [10] for LOS case that path loss can be characterized by only LOS ray ignoring the deviations, meaning almost all received power is conveyed in the LOS ray. That means, by sector selection approach, first and second order reflections from

walls and ceiling contribute less power than the LOS ray. In fact, this is intuitive, because, besides the free space attenuation is higher due to higher distance, there is an additional reflection loss as well for reflected clusters [33]. This yields a high probable result that the best sector should be the one in the direction of receiver, that is, in the LOS ray direction. Hence, once the rough direction of the station is determined, several sectors can be directly eliminated in the searching process.

Two searching methods are proposed in this section. Methods are discussed for the first part of SLS phase in IEEE 802.11ad BF, i.e. ISS sub-phase. Same algorithms can be used for the RSS part as well. Customization for IEEE 802.15.3c is given briefly at the end of each method. We assume each DEV/station has just one transmitter and one receiver antenna. N and M denote the number of sectors in transmit antenna of initiator and responder stations, respectively. For convenience, we assume both are powers of 2 and have the minimum value of 4, the maximum value of 64. So, they can have one of the following values: $\{4, 8, 16, 32, 64\}$.

8.3.1 Binary Searching

The method divides the ISS section into further stages by selecting the sectors that will be used to send frames according to the FB received at the end of every stage.

Stage 1: Initiator transmits from its four cross sectors, specifically from $ID = 1$, $ID = (1 + N/4)$, $ID = (1 + 2N/4)$ and $ID = (1 + 3N/4)$; that is, takes $N/4$ steps for each consecutive frame. Right after the fourth frame, it switches to listening (receiving) mode in quasi-omni pattern. Responder listens in quasi-omni pattern during frame transmission. After the fourth frame, it selects the frame (and corresponding sector) with highest received SNR and sends an FB of best sector ID and its received SNR value by using its quasi-omni transmitter pattern.

Stage 2: Initiator signs the best sector and keeps its SNR value in memory. It transmits two new frames from $N/8$ steps back and forward of the best sector, i.e. from $ID = (bestsector + N/8)$ and $ID = (bestsector - N/8)$. And then it immediately switches to receiving quasi-omni mode. Responder compares two frames and transmits an FB of the best of two sectors and its received SNR value again.

Stage 3: Initiator picks the incoming sector ID, compares its SNR value with the one's which it has already been keeping in its memory and updates the best sector. Replacing the SNR value in memory with the updated one, it transmits two new frames from $N/16$ steps back and forward of updated best sector, i.e. from $ID = (bestsector + N/16)$ and $ID = (bestsector - N/16)$. And then it immediately switches to receiving quasi-omni mode. Responder compares two frames and transmits the FB of best of two sector ID and its received SNR value again.

Stage 4 and 5: The same procedure with Stage 3 is performed in Stage 4 and Stage 5 except that the initiator now transmits two frames from $N/32$ and $N/64$ steps back and forward of updated best sector, respectively..

ACK Stage: Initiator updates the best sector and acknowledges it to responder. Indeed, responder doesn't need to know the best transmit sector of initiator, but ACK frame will be a good reference for responder to begin RSS sub-phase. Furthermore, a BRP phase information can be exchanged between stations by using ACK frames.

Apparently, the algorithm tries to narrow its coverage area in each stage and eliminates the sectors outside the focused area. Since this elimination process resembles binary searching in data structure algorithms, we call the whole procedure as *Binary Search Beamforming* (BSB) algorithm. Immediate results and extensions for BSB are as follows: (1) Number of stages depends on the number of sectors and equals to $\log_2(N/2)$. For example, for $N = 32$ sectors, Stage 4 is the last part and initiator skips directly into the ACK stage. Also we note that for $N = 4$, it turns into conventional 802.11ad BF. (2) Because of elimination of a number of sectors, BF setup time is expected to be reduced compared to 802.11ad BF algorithm. (3) Adaptation for IEEE 802.15.3c can be as following. In Stage 1, initiator (or DEV1) sends as many sequences as responder's receive sectors from specified four transmit sectors and responder (or DEV2) sends back the FB applying the same algorithm; that is, sends as many sequences as DEV1's receive sectors from its specified four transmit sectors. In Stage 2, there is no need to send several sequences from one sector anymore, because DEVs have already known their best receive sectors. Procedure continues exactly the same as described above.

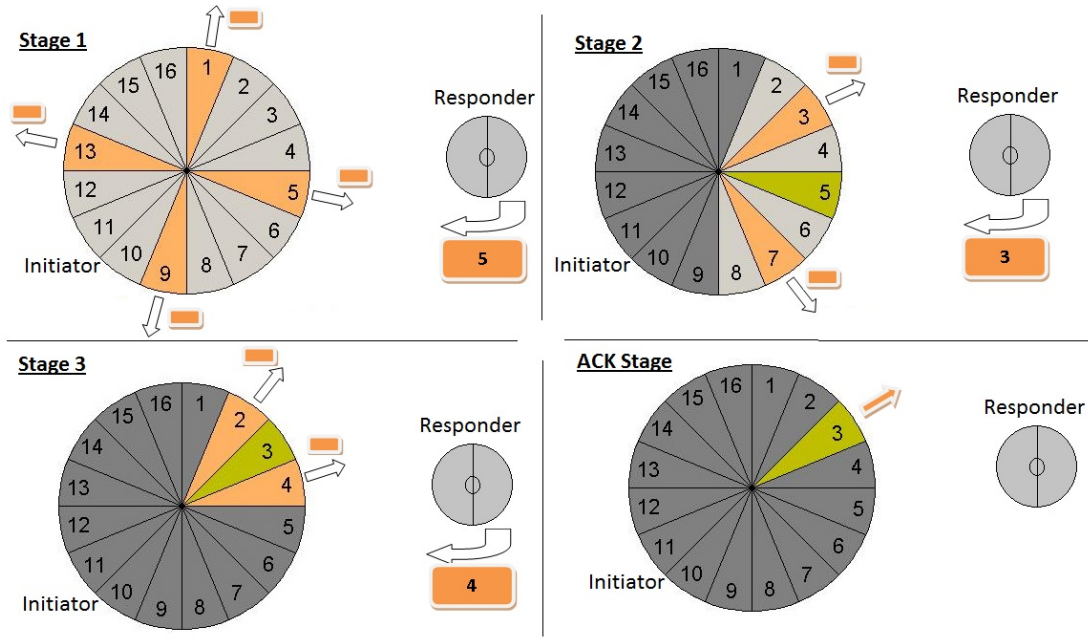


Figure 8.1: An example of BSB algorithm for $N=16$.

Stage 1 is the most critical part of the algorithm. If all frames are lost in Stage 1 which has very low probability, algorithm repeats Stage 1 as rotating each sector ID by 45 degrees. If still all packages are lost, then BSB algorithm is not able to select the best sector and should switch to isotropic antenna model. Otherwise, error would be higher and smart antenna wouldn't be useful at all.

An implementation example of proposed algorithm for $N = 16$ sectors is shown in Fig. 8.1. In Stage 1, initiator transmits frames from $ID = 1, 5, 9$ and 13 . Responder feedbacks that sector $ID = 5$ was the best. In Stage 2, initiator updates the best sector as 5 and transmits two frames from $ID = 3$ and 7 . Responder sends an FB of the best of two frames as sector 3. In stage 3, initiator compares SNR values of 5 and 3, updates the best sector as 3 and transmits two new frames from $ID = 2$ and 4 . Responder turns back that sector $ID = 4$ has been received with highest SNR. Initiator compares 4 and 3, and sends an announcement to responder that its best transmit sector is 3. This forms the ACK Stage and ends the algorithm.

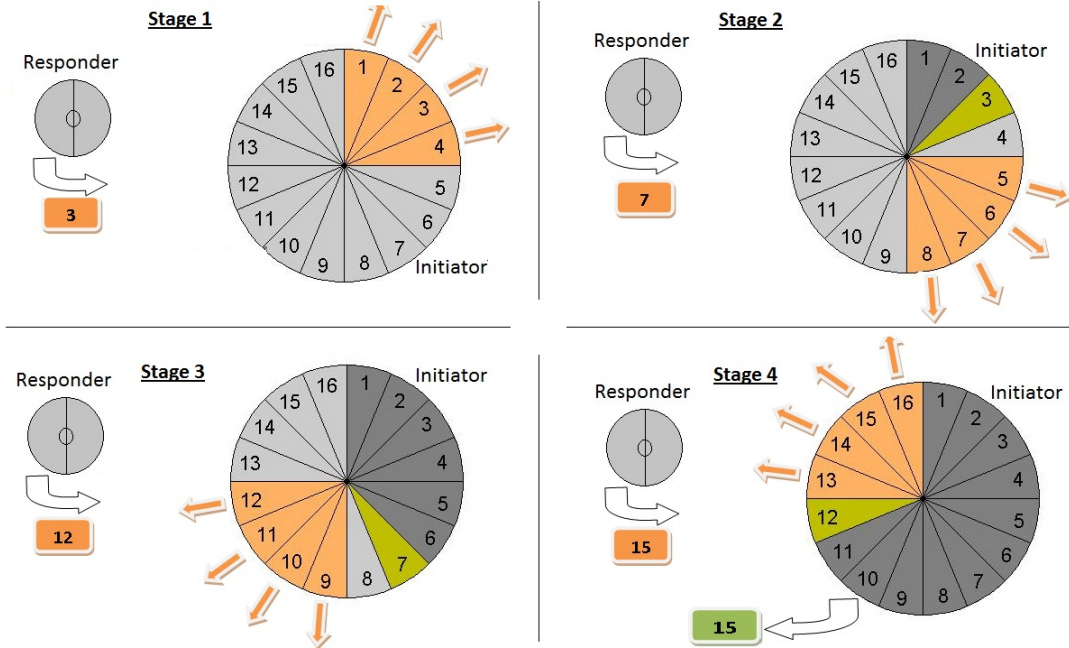


Figure 8.2: A worst case example of LSB algorithm for $N=16$.

8.3.2 Linear Searching

As seen in the previous subsection, the idea of eliminating some sectors reveals the way of constructing efficient searching methods. In this subsection, another searching method is proposed. Similar to the previous case, since elimination procedure looks similar to the linear searching in data structures, we call the process as *Linear Search Beamforming* (LSB) algorithm. Stages are given as followings.

Stage 1: Initiator transmits four frames from its one way of successive sectors, say from $ID = 1, 2, 3$ and 4 , then switches to quasi-omni listening mode. Responder listens in quasi-omni pattern during transmission. After the last frame received, it selects the frame with highest SNR value and transmits it as FB along with its SNR value. Again, as during every FB, responder transmits in the quasi-omni pattern.

Stage 2: Initiator keeps the sector ID and its SNR value in memory. In that point, Stage 2 depends on the selected sector and algorithm acts according to two different possibilities as described following: (1) If sector $ID = 1$ or 2 was selected, either it is the LOS ray (overall best sector) or searching is spinning in the wrong direction. Hence, to be sure, four new frames have to be transmitted from $ID = N$, $(N - 1)$,

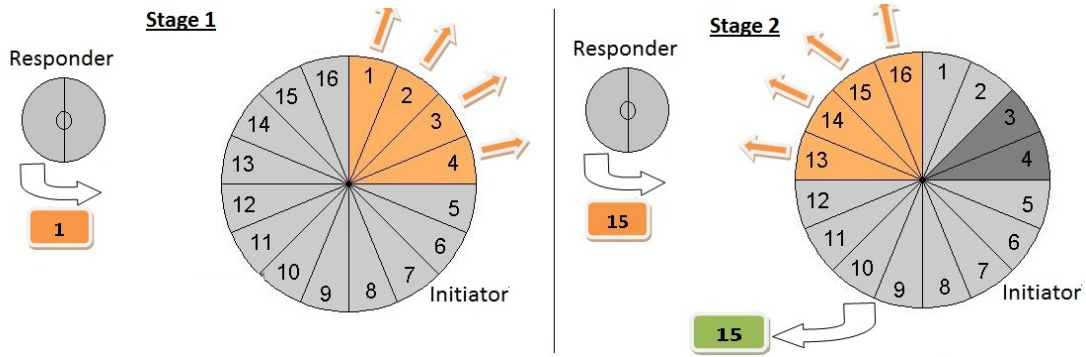


Figure 8.3: A best case example of LSB algorithm for $N=16$.

$(N - 2)$, $(N - 3)$, i.e. reverse spinning. (2) If sector $ID = 3$ or 4 was selected, at least spinning direction is correct or it is the overall best sector. However, again just in case, keeping the direction, four new frames from successive sectors are transmitted; that is, with $ID = 5, 6, 7$ and 8 . Right after transmission, initiator switches to listening mode in quasi-omni pattern. Responder listens during transmission, sends the highest SNR value sector as FB after received last frame.

Stage 3: Initiator keeps the new best sector ID and its SNR value in memory. Now, since two possibilities might occur in previous stage, we have two different output case for each probability, then four possibilities show up totally for this stage.

Assuming first probability has occurred in Stage 2, (1) Responder chooses $ID = N$ or $(N - 1)$. Then initiator compares SNR value in memory (of 1 or 2) with the new selected SNR and updates best. This ends the algorithm and initiator skips directly into the ACK Stage. (2) Responder chooses $ID = N - 2$ or $N - 3$. In that case, in case of further sectors in the current direction may be the best, initiator sends new four frames from sector $ID = N - 4, N - 5, N - 6$ and $N - 7$ and switches listening mode.

Assuming second probability has occurred in Stage 2, (3) Responder chooses $ID = 5$ or 6 . Similar to the case (1), initiator decides the best sector and ends the algorithm. (4) Responder chooses $ID = 7$ or 8 . Similar to the case (2), initiator transmits four successive frames from $ID = 9, 10, 11$ and 12 .

As noticed in so far stated stages, the procedure repeats itself according to a pattern with an increasing number of probable outcomes. Indeed, we may generalize it using best and worst cases for different numbers of sectors. For the worst case, the number

of stages equals to $N/4$. Fig. 8.2 shows an example of such a case for $N = 16$. In Stage 1, spinning is in the wrong direction, but we assume that responder missed that and decided $ID = 3$ was the best. Algorithm proceeds spinning and initiator sends four new frames in Stage 2. Responder gives an intuitively expected result that 7 was the best. Similarly, in Stage 3, responder chooses 12 and in the last stage, the best sector is decided as 15. We should emphasize that the word "worst" or "best" is regarding setup time, not terms of choosing the right sector.

For the best case, algorithm ends in the second stage for all N . This case is also illustrated in Fig. 8.3 for the same situation discussed for the worst case. As seen in Fig. 8.3, we ignored the half of sectors and reduced the training time 50% with respect to exhaustive search BF algorithm.

Customization for 802.15.3c is similar to BSB algorithm except that appropriate increase of the number of sequences in Stage 1 won't be enough for DEV2 receive sector training due to the narrow transmit coverage of DEV1 in the first stage. So, we propose to send multiple sequences in Stage 2 too. Algorithm proceeds same in remained stages.

Both algorithms completely fit for RSS sub-phase as well. The same procedures can be applied with replacing every N with M .

8.3.3 Step Analysis

We calculate the number of steps required in sector training process for both current BF algorithms of two standards and proposed methods. Table 8.1 shows step analysis of each method for four different $N = M$. Calculation is done as following for each method. For convenience, each analysis is described for $N = M = 16$.

IEEE 802.11ad

For comparison of the methods, only SLS phase steps are considered. Initiator transmits $N = 16$ frames in ISS and responder transmits $M = 16$ frames in RSS. Adding 2 frames for SSW-F and SSW-ACK, we have 34 steps to train transmit sectors of both stations.

Table 8.1: Step Analyses of BF Algorithms

Methods/ $N = M$	8 Sectors	16 Sectors	32 Sectors	64 Sectors
802.11ad	18	34	66	130
BSB WLAN	18	24	30	36
LSB WLAN	22	32	52	92
802.15.3c	140	532	2084	8260
BSB WPAN	37	144	278	540
LSB WPAN	134	272	548	1100

BSB Method for IEEE 802.11ad: In the first stage, initiator transmits 4 frames, and receives 1 FB. Following two stages, initiator sends 2 frames, gets 1 FB. Adding ACK frame, totally 12 frames are needed to perform ISS sub-phase. Similarly, 12 frames are exchanged during RSS. Hence, 24 frames are enough to train transmit sectors of stations. This method is stated as BSB WLAN in Table 8.1.

LSB Method for IEEE 802.11ad: To be able to compare with the other methods, we analyze LSB algorithm as considering the number of average steps, i.e. $(\text{worst case steps} + \text{best case steps})/2$. We have already analyzed worst and best case scenarios for $N = 16$. While 42 frames are needed for the worst case, 22 frames is enough for the best case to complete SLS phase. So average is 32 frames. This method is stated as LSB WLAN in Table 8.1.

IEEE 802.15.3c

As described in Section 8.2, during sector training, for the DEV1 to DEV2 part, there are 16 cycles for each transmit sector of DEV1. That counts $16 \times 16 = 256$ training sequences for DEV1 training. Similarly, 256 sequences are needed for DEV2 training. Adding the $16 + 1 = 17$ FB and three mapping, acknowledgement commands, sector training is completed in totally 532 steps. This may seem too high compared to WLAN standard, but two main differences should be emphasized here: (1) At the end of this section, both transmit and receive sectors are trained for both DEVs. (2) Instead of packets or frames, preambles are used as training sequences during sector training stage. Although the number of steps is extremely high, training time is relatively same

length with WLAN standard due to shorter preamble sequences. Codebooks are used to convey sector IDs [75].

BSB Method for IEEE 802.15.3c: Customization of BSB algorithm for WPAN is performed in the first stage. During the DEV1 to DEV2 part of sector training, for each transmit sector of DEV1, there is a cycle consisting of 16 sequences for DEV2 receive sectors. At the end of the first stage, DEV1 will have sent $4 \times 16 = 64$ sequences and DEV2 has already determined its best receive sector by looking average of four frames. It is important to note here that FB command frame is transmitted from the best sector of DEV2. So, remained two stages proceed identical to BSB WLAN. Then DEV1 to DEV2 part needs $(64 + 1) + (2 + 1) \times 2 + 1 = 72$ steps. Multiplying two for DEV2 to DEV1 part, training is completed in 144 steps. It should be noticed that feedback training, mapping and acknowledgement stages are ignored, since all are already completed during sector training. This method is stated as BSB WPAN in Table 8.1.

LSB Method for IEEE 802.15.3c: As discussed earlier, different from BSB method, number of frames will multiply by 16 due to DEV2 receive training in the first *and* second stages. For the worst case, DEV1 transmits 128 sequences in Stage 1 and Stage 2, eight sequences in Stage 3 and 4. Adding 4 FB, 1 ACK and multiplying by two (DEV2 to DEV1), we need 282 steps. For the best case, this reduces to 262. So, the average is 272 steps.

As seen in Table 8.1, BSB algorithm is more efficient than LSB in terms of required steps. Both proposed methods perform better than standards except the case when $N = M = 8$ for WLAN.

8.4 Simulation Results

In this part, we simulate the performances of proposed methods using MATLAB. We follow IEEE 802.11ad specifications to simulate proposed methods and compare with the current exhaustive search BF algorithm. Three criteria is discussed: BF setup time, error performance and power analysis. We use the conference room channel

Table 8.2: Simulation Parameters

Parameter	Description
Channel Model	TGad Model Conference Room [10]
Subscenario	STA-STA
Number of Antennas	1 for each STA (SISO)
Distance	1-11 meters
Frequency	60 GHz
Modulation and Coding Scheme	Control PHY (MCS-0)
Number of Chips	3 (for each SNR)
Cluster/Case	LOS
Noise/Loss Model	AWGN and Path Loss
Shadowing Effect	Disabled
Antenna Model	Basic Steerable Antenna
Polarization Support	Disabled
Number of Experiments	40 (for each number of sector)

model described in [10] considering the communication link is between station to station (STA-STA). Parameters used in simulations are given in Table 8.2.

8.4.1 Beamforming Setup Time

In Fig. 8.4, BF setup time performances of BF methods are presented as time axis is displayed in log domain. Exhaustive search (ES) algorithm setup time increases exponentially as the number of sectors increases from 12 to 60. On the other hand, proposed methods' required time increase very slightly for the same number of sectors. While approximately 9 seconds are required for scanning 60 sectors in ES, it is only 0.2 and 0.1 seconds in BSB and LSB, respectively. These correspond only 2.2% and 1.1% of ES. Those values go up around 5% for 36 sectors and increase as the number of sectors decreases.

8.4.2 BER Performance

Fig. 8.5 shows error performances of BSB, LSB and ES for 12, 36 and 60 sectors. *Ech* stands for "average chip power" where chip is in 18688 samples length, 32 times spread

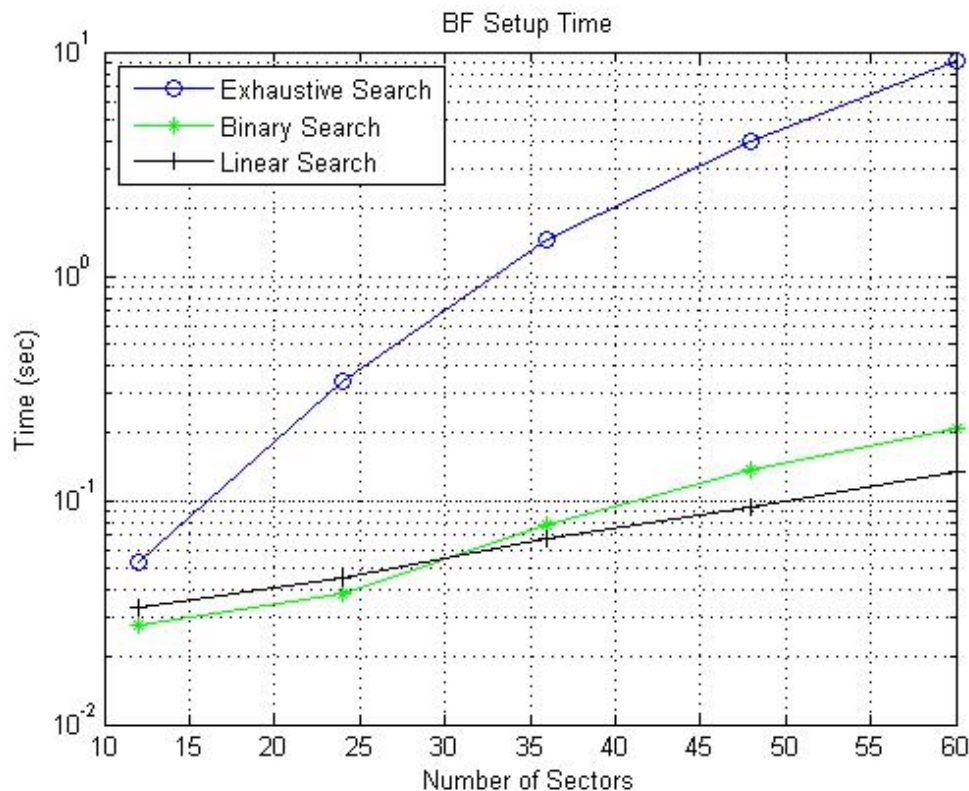


Figure 8.4: BF setup time performances of proposed methods

Control physical layer (PHY) frame. Isotropic antenna error performance is also shown in Fig. 8.5. As LSB presents same performance with ES for any number of sectors, BSB gets worse with increasing number of sectors although it is efficient for 12 sectors. To get 10^{-4} BER for 60 sectors, BSB needs 10 dB more SNR compared to ES. That reduces to 0 dB when 36 sectors antenna is used. For ES and LSB, as the number of sectors increases, BER decreases while this is conditionally true for BSB.

8.4.3 Power Saving Performance

Power consumption of ES, LSB and BSB during transmit sector training is shown in Fig. 8.6. BSB has clear advantage in terms of power saving as it ignores several sectors with not sending frames from these sectors. The required power gap between ES and BSB is approximately 6 dB for 60 sectors, 5 dB for 36 sectors, while they are 2 dB and 1.5 dB between LSB and ES, respectively.

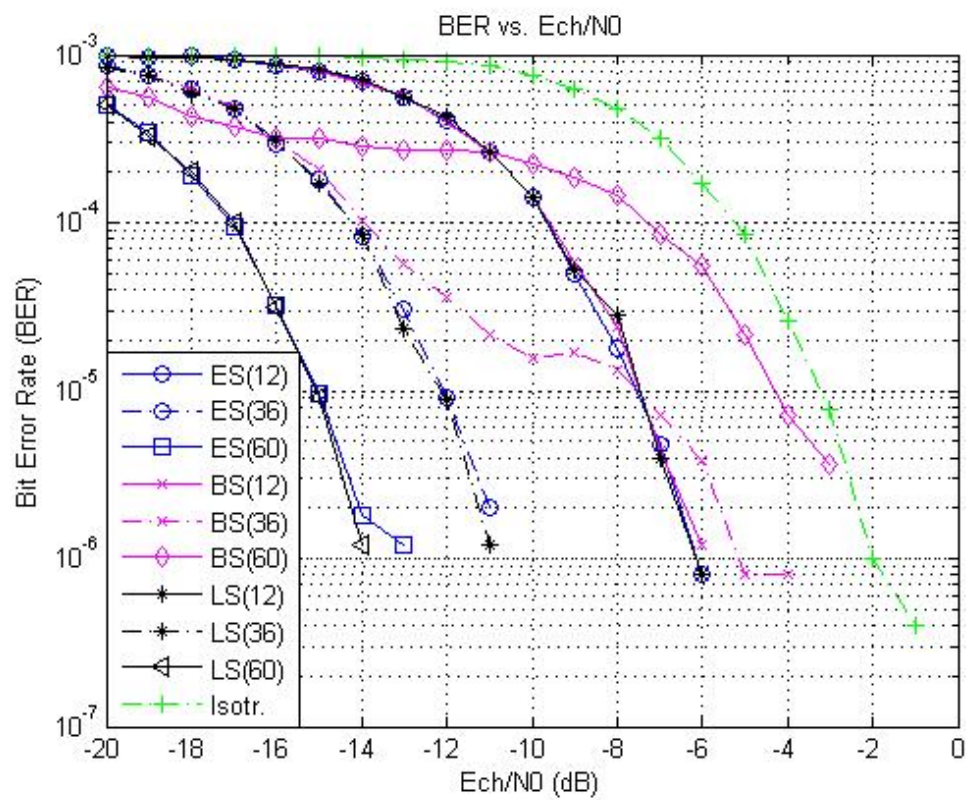


Figure 8.5: Error performances of proposed methods for $N=\{12, 36, 60\}$

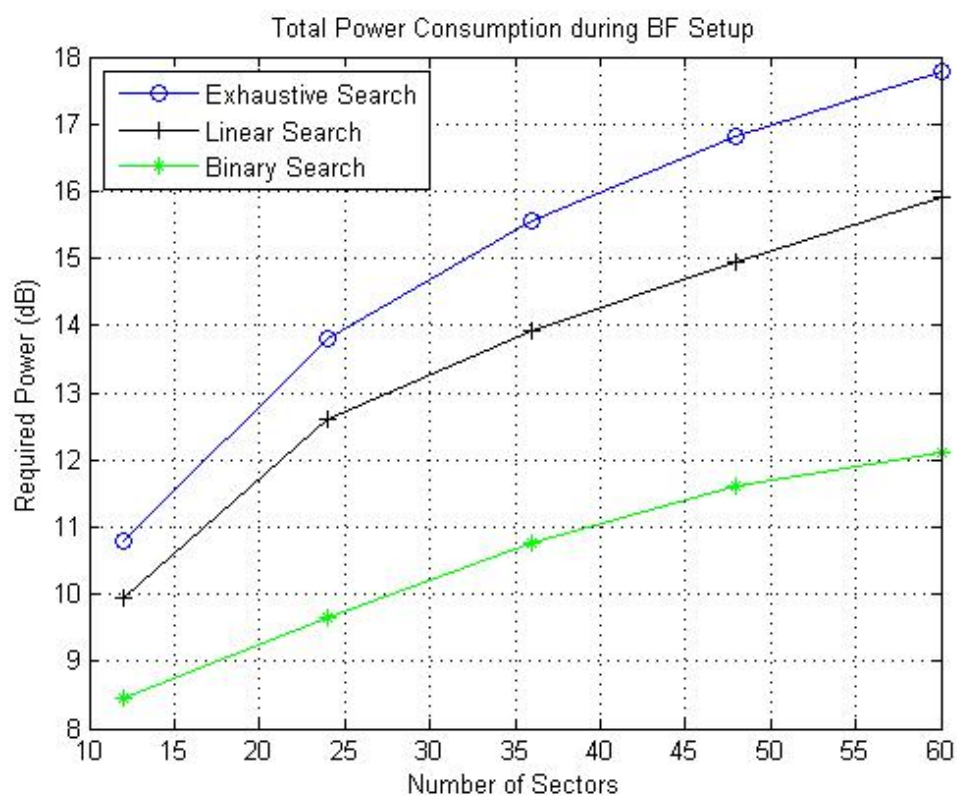


Figure 8.6: Power consumption of BF algorithms during transmit sector training

Chapter 9

Enhanced Binary Search for NLOS Environments

Exhaustive search beamforming (BF) protocol of IEEE 802.11ad and IEEE 802.15.3c mm-wave communication standards consume time and power. A time-efficient iteration-based Binary Search Beamforming (BSB) protocol was introduced as a replacement for the BF clauses in the standards. In this chapter, we propose an improved method, Enhanced BSB (EBSB), to support NLOS environments in which BSB doesn't work efficiently [3]. We also define a new "single-side approach" to remove the local maxima from which earlier solution methods suffer. Our proposed method aims to select the best beam pair in fewer steps using an iteration-based algorithm which reduces the BF setup time. We provide performance comparison of exhaustive search, BSB and EBSB in terms of step analysis, success probability, BF setup time and power loss performances. In NLOS case, for smaller than 100 sectors at both devices' antennas, EBSB reaches higher than 0.9 probability of successfully pairing the best beams. On the other hand, training time reduces to around 34% for 330 sectors at both antennas. For the cases when EBSB fails, power loss analysis shows that the average gain loss is less than 1 dB.

9.1 Motivation

Mm-wave communication has reached a significant level of research interest due to the high-speed data rate opportunity and increased available bandwidth for short-range applications. As defining the standards of communication in that band, IEEE 802.11ad [71] and IEEE 802.15.3c [72] have been published. The most important challenge in mm-wave communications is the considerably high signal path loss. To overcome this problem, directional communication has been proposed using antenna arrays or steering

antennas in order to increase antenna gains both at the transmitter and the receiver. To setup a directional link between stations (STAs), beamforming (BF) is used to identify the communication direction before high-speed data sharing.

A sector-based approach to BF is taken by both 802.11ad and 802.15.3c. Authors in [73] describe the BF algorithm adopted by the IEEE 802.11ad standard. With some modifications, some other improvements for current version of the standards' BF algorithm are already present in the literature [76], [77]. However, their works still perform an exhaustive search which requires considerable time to setup a beamformed link. On the other hand, some advanced methods using optimization techniques are studied in recent years [78], [79]. Nevertheless, these optimization techniques suffer from several local maxima in the objective function map even in the LOS environment due to the noisy and multipath nature of the channel.

Our earlier algorithm, called Binary Searching Beamforming (BSB) [2], reduces BF setup time by neglecting some sectors relying on the fact that the line-of-sight (LOS) ray is the most dominant cluster whenever available [10]. In other words, BSB is an iterative method that aims towards getting closer the LOS ray while ignoring a number of sectors in every iteration stage.

In this chapter, we extend our work for BSB algorithm by primarily add support for NLOS environments. In addition, while we improve the BSB algorithm in terms of reliability, a novel single-sided approach is described as well. Our enhanced procedure can be integrated into the sector level sweep (SLS) and sector-level training parts of the IEEE 802.11ad and IEEE 802.15.3c beamforming clauses, respectively.

9.2 System Model

Although we use the Basic Steerable Antenna Model [10] in the simulations, this chapter doesn't stick to a certain type of antenna, hence a type of beamforming. So, instead of giving details about the antenna structure, we rather focus on the algorithm relies on beams as an abstraction. Details about the antenna model that we use in the simulations are given in the Simulation Results Section.

Codebook-based beamforming exploits optimization techniques which try to choose the best beam pair (p, q) (p and q are beam IDs of STA1 and STA2, respectively) that maximizes the received power function shown in Eq. (9.1) [78], [79].

$$S(p, q) = \sum_m \sum_n |[E_t^V E_t^H][\mathbf{H}^{(m)} \alpha^{(m,n)} AF_p(\Phi_t^{(m)} + \phi_t^{(m,n)}) AF_q(\Phi_r^{(m)} + \phi_r^{(m,n)})][E_r^V E_r^H]^T|^2, \quad (9.1)$$

where $[E_t^V E_t^H]$ and $[E_r^V E_r^H]$ are polarization vectors for STA1 and STA2 antenna respectively; $\mathbf{H}^{(m)}$ and $\Phi_t^{(m)}, \Phi_r^{(m)}$ represent the m -th cluster gain matrix and the corresponding angular coordinates respectively; $\alpha^{(m,n)}$ and $\phi_t^{(m,n)}, \phi_r^{(m,n)}$ denote the n -th ray amplitude and the relative angular coordinates within the m -th cluster respectively; $AF_p(\Phi)$ is the array factor for the p -th beam.

An example of the reward function (i.e. received gain) versus feasible solutions experiment set is shown in Fig. 9.1 for LOS environment while N shows the number of beams in STAs. For convenience, we assume that STA1 and STA2 have an equal number of beams and transmitting power is 1mW in this chapter. As seen in Fig. 9.1, although the global maximum (maximum received power) is obvious, there are several local maxima in the energy map as well. That makes sense when we look at Eq. (9.1), because array factors are calculated for STA1 and STA2 separately. For example, when the current beam of STA1 has lower array factor as STA2 beam has higher, resulted received power seems relatively high too which causes local maxima. That makes the optimization methods impractical since algorithms suppose that the local maximum reached in a few steps is the best solution and end the algorithm. This problem gets worse in NLOS environments as even the global maximum is not obvious at all due to the multipath effect.

In fact, local maxima are the problem that any kind of optimization (including ours) suffer from. In this spot, instead of changing the method, we propose improving the model that we work on with some practical assumptions.

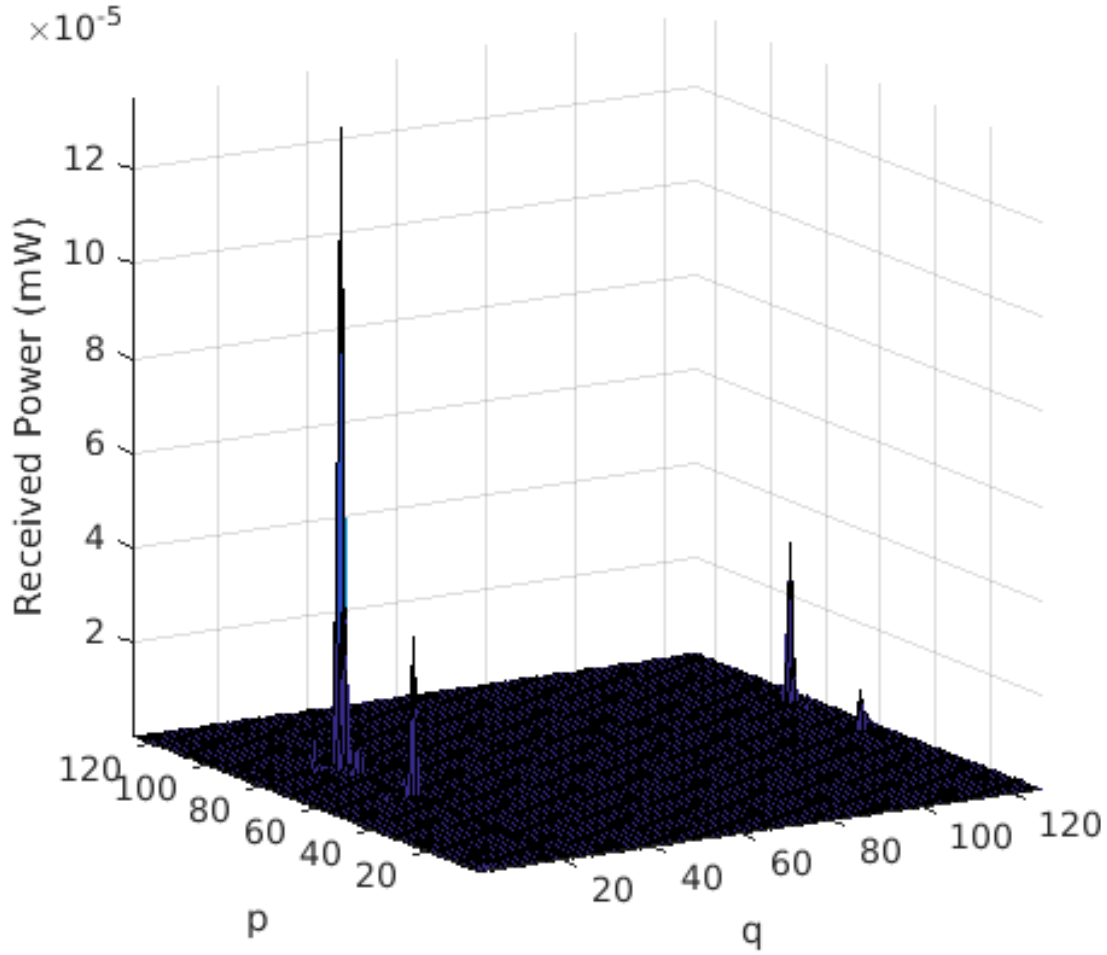


Figure 9.1: Received power for each pair for $N = 120$.

9.2.1 Single-Side Approach

Assuming G_{p_i} and G_{q_j} represent the STA1 and STA2 transmitter (TX) and receiver (RX) antenna gains respectively, consider $N \times N$ received gain matrix \mathbf{G} with the elements $G_{p_i q_j}(dB) = G_{p_i}(dB) + G_{q_j}(dB)$ as shown in Eq. (9.2). In fact, this matrix is the algebraic version of Fig. 9.1.

$$\mathbf{G} = \begin{bmatrix} G_{11} & G_{12} & G_{13} & \dots & G_{1N} \\ G_{21} & G_{22} & G_{23} & \dots & G_{2N} \\ \vdots & \vdots & \vdots & \ddots & \vdots \\ G_{N1} & G_{N2} & G_{N3} & \dots & G_{NN} \end{bmatrix} \quad (9.2)$$

Note that every element of \mathbf{G} is actually a result of one-step experiment; i.e. one packet from STA1 to STA2. Hence, the maximum-valued element of \mathbf{G} reveals the best communication link from-STA1-to-STA2. Same training procedure has to be applied for the link from-STA2-to-STA1 additionally, if needed. For example, for $N = 8$, there are 64 elements in the matrix, but 128 steps are required to train both way communication links. This search is adopted by IEEE 802.15.3c and called "exhaustive search".

Indeed, without loss of generality, if we assume that the best receiving beam of STA2 is already known, the problem reduces to train only STA1 transmitting beams. This corresponds to search for an element over a specific column vector of \mathbf{G} , say $\mathbf{g}_t = [G_{1q_k} \ G_{2q_k} \ G_{3q_k} \ \dots \ G_{Nq_k}]^T$ where q_k is a number from $1 \leq q_k \leq N$ and T is for transpose.

The assumption of q_k knowledge can be realized by performing an exhaustive search in the STA2 side. Now that we know q_k , the goal is to find the best transmitting beam of STA1. Since we propose sampling only the rows of \mathbf{G} , we call it "single-side approach". The resulting energy density map of \mathbf{g}_t vector is described in the next subsection.

9.2.2 Energy Density Map of Antenna Beams

To be able to see how the searching algorithm can be applied to the system, it is a good idea to see some samples of the dataset in order to grasp its usual behavior under different channel conditions. At first glance, it can be seen from Fig. 9.1 that the vector \mathbf{g}_t is, in fact, the result of the straight line along the best q . However, we propose to use another model to show the energy density map of \mathbf{g}_t in order to stay in the 3- D domain. Note that \mathbf{g}_t is the gain vector of STA1 transmitting sectors when the best receiving beam of STA2 is fixed. That is, every element of \mathbf{g}_t represents the result of total antenna gain in the link when the corresponding STA1 beam is used in the communication trial. Hence, it can be visualized in a design of using only STA1 sectors as two examples are shown in Fig. 9.2 in LOS case for $N = 61, 127$.

Circles in Fig. 9.2 represent the beams of the STA1 transmitting antenna in which their area are made smaller for ease of observation. This is the 3-D design proposed in [10] and we capture the antenna propagation from aerial viewpoint here. Since

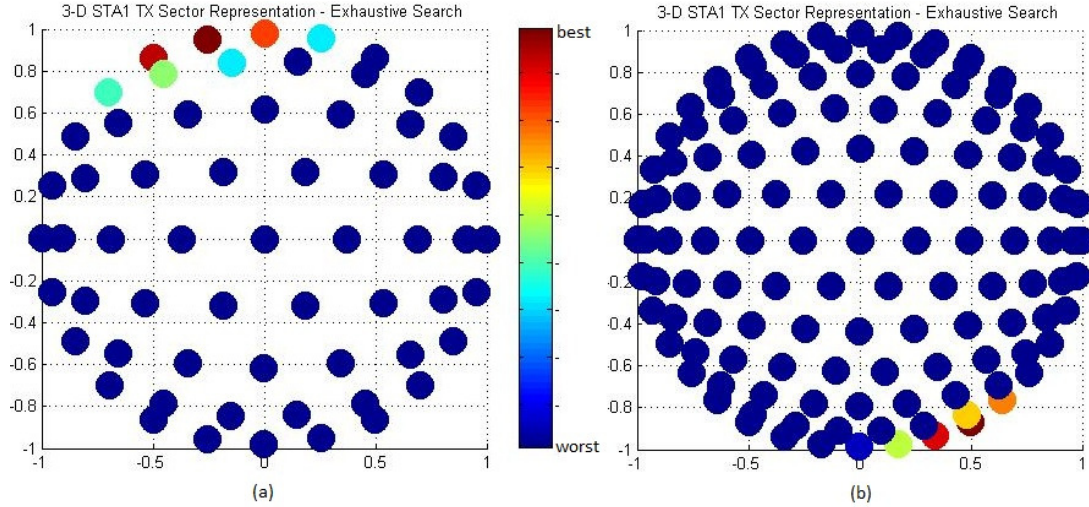


Figure 9.2: Energy density map of STA1 transmit sectors in LOS case for (a) $N = 61$, (b) $N = 127$.

STAs are both on the table and see each other at the same level, the elevation angle of the best beam is almost always zero. More importantly, there are no local maxima anymore in the solution set. This is also intuitive from Fig. 9.1 when the straight line is crossed along the best q and observed from the p side. Then, for LOS case, one can use convex optimization methods without suffering from picking the best initialization points problem [78], [79].

On the other hand, Fig. 9.3 simulates the results of two trials in NLOS conditions for $N = 61, 127$. As it can be seen, we still encounter local maxima due to multipath channel conditions, as expected. However, as we propose in this chapter, they can be avoided by applying BSB algorithm [2] with performing some additional modifications.

9.3 Proposed Enhanced-BSB

First, we describe BSB algorithm briefly and then explain the proposed method.

9.3.1 BSB Algorithm

BSB aims to find the sector covers the LOS ray (it is believed to be the best) in an iterating way. As stated above, since the elevation angle of the best beam is almost always zero in LOS, BSB algorithm focuses only on azimuth scanning; i.e. 2-D scanning.

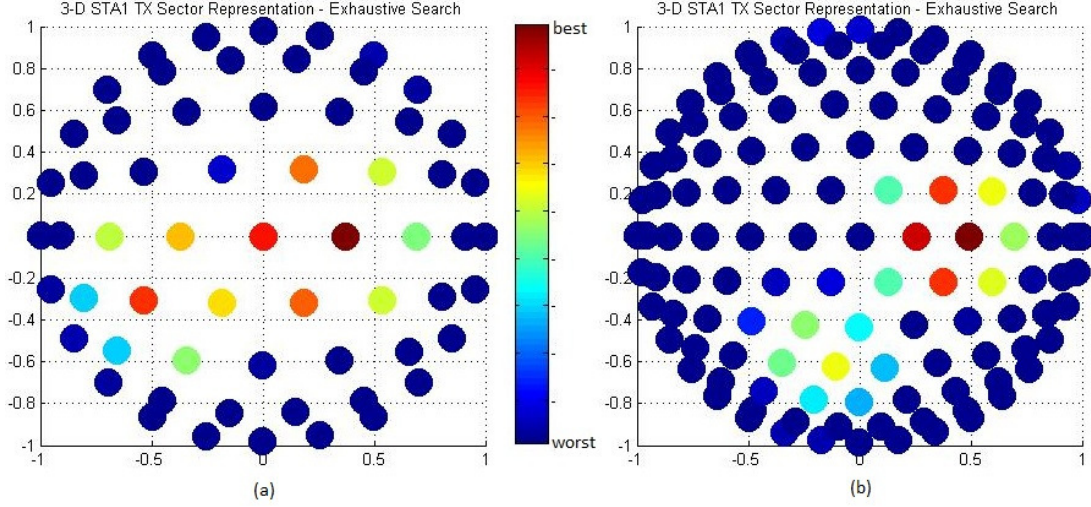


Figure 9.3: Energy density map of STA1 transmit sectors in NLOS case for (a) $N = 61$, (b) $N = 127$.

System is introduced as following.

Stage 1: STA1 transmits four packets (frame or preamble sequences) from its four sectors which are selected according to Eq. (9.3) where $ID(i)$ represents the ID of the i -th packet. The variable i is reset at the beginning of every stage. Here N_{tx} shows the number of beams in the current azimuth direction.

$$ID(i) = 1 + (i - 1)N_{tx}/4 \quad i = 1, 2, 3, 4 \quad (9.3)$$

Stage 2: STA1 updates the the best beam $ID(b)$ according to the feedback from STA2 and transmits 2 packets from the sectors calculated by Eq. (9.4).

$$ID(i) = \begin{cases} ID(b) + \lceil N_{tx}/(4 \times 2^{(M-1)}) \rceil, & \text{when } i = 1 \\ ID(b) - \lceil N_{tx}/(4 \times 2^{(M-1)}) \rceil, & \text{when } i = 2 \end{cases} \quad (9.4)$$

Whenever the condition $\lceil N_{tx}/(4 \times 2^{(M-1)}) \rceil = 1$ is met, algorithm ends the azimuth scanning after completing the current stage. In our simulations, we added a "check-up stage" which tests the sectors in the elevation direction as fixing the best azimuth angle.

It basically tries to narrow its coverage area hierarchically and eliminates the sectors outside the focused area. Since this elimination process resembles binary searching in

data structure algorithms, we called the whole procedure as Binary Search Beamforming (BSB) algorithm. More details about BSB can be found in [2].

9.3.2 Proposed Method EBSB

BSB algorithm [2] is designed for LOS environments and primarily focuses on power-limited small devices which have relatively low number of sectors. However, our simulation results show that success rate of BSB algorithm reduces to even below 40% in NLOS conditions. As a result, regardless of the number of sectors antenna has, BSB algorithm is not practical for NLOS environments. Although we propose an almost new algorithm compared with BSB in this section, we still keep the binary search approach used in data structures. For that reason, we prefer calling it "Enhanced BSB (EBSB)". Similar to BSB, EBSB works on the designed platform shown in Fig. 9.2 and Fig. 9.3 which distinguishes the proposed algorithms from the well-known original binary search that uses sorted arrays.

Basically, EBSB scans over the azimuth direction ($\varphi = [0, 360]$) for each discretized elevation angle ($\theta = [0, 90]$) which can be also interpreted as layer scanning; i.e. the first layer corresponds to $\theta = 0$, and the last does $\theta = 90$. L shows the number of layers; i.e. the number of quantized elevation angles and depends on N . N_l is the number of sectors in the l -th layer where $1 \leq l \leq L$. For convenience, we describe the algorithm only for one layer, because it works exactly same for other layers.

Stage 1: Algorithm divides the layer into 6 pieces of equal size. STA1 transmits a packet from each piece, totally six packets which are also from equally spaced six sectors according to Eq. (9.5) where $ID(i)$ represents the ID of the i -th packet. The variable i is reset at the beginning of every stage.

$$ID(i) = 1 + (i - 1)N_l/6 \quad i = 1, 2, \dots, 6 \quad (9.5)$$

That is, it takes $N_l/6$ steps for each consecutive packet. After the sixth packet, STA2 selects the packet with the highest received SNR (or RSS) and returns the ID of that packet as an FB.

Stage 2: STA1 signs the best sector ($ID(b)$) and keeps its SNR value in memory.

It transmits two new packets using Eq. (9.6), that is, $\lceil N_l/12 \rceil$ steps back and forward of the best sector. STA2 compares the SNR value of two packets and transmits the ID of the packet whose value is higher as an FB.

$$ID(i) = \begin{cases} ID(b) + \lceil N_l/(6 \times 2^{(M-1)}) \rceil, & \text{when } i = 1 \\ ID(b) - \lceil N_l/(6 \times 2^{(M-1)}) \rceil, & \text{when } i = 2 \end{cases} \quad (9.6)$$

Stage 3: STA1 picks the incoming sector ID, compares its SNR value with the one in the memory and updates $ID(b)$. It transmits two new packets using Eq. (9.6), again. STA2 acts same as in previous stages.

Stage K: The same procedure in Stage 3 is performed in Stage K. When algorithm sees the value $\lceil N_l/(6 \times 2^{(K-1)}) \rceil = 1$, it jumps to upper layer after running Stage K. If current is the L -th layer, it skips to the Last Stage described below.

Last Stage: After scanning all L layers, STA1 updates the best sector and acknowledges it to STA2. Indeed, STA2 doesn't need to know the best transmit sector of STA1, but ACK frame would be a good reference for STA2 to begin the possible further beam refinement sub-phase.

An implementation example of proposed algorithm for $N_1 = 24$ is displayed in Fig. 9.4 that includes 4 sub-figures where each sub-figure represents a stage. Sub-figures show the antenna model of STA1 only in which the layering approach is also denoted with circles. The algorithm starts scanning from the first layer, that is, from the outermost. In Stage 1 for $l = 1$, using Eq. (9.5), STA1 transmits from $ID = 1, 5, 9, 13, 17$ and 21 which are stressed with bigger circles. Then FB of $ID = 1$ is received, which is also denoted by an arrow. In Stage 2, STA1 signs the $ID = 1$ as the best beam (denoted with the biggest circle) and transmits from $ID = 3$ and $ID = 23$ using Eq. (9.6). FB says $ID = 3$ is better. In Stage 3, STA1 updates the best sector and transmits two packets from $ID = 2$ and $ID = 4$, again using Eq. (9.6). FB is $ID = 2$. Since STA1 calculated the increment value equals to 1, it updates the best sector in $l = 1$ and in the next stage, it jumps to upper layer, starts from Stage 1 again and transmits six packets from $ID = 1, 4, 7, 10, 13$ and 16 using Eq. (9.5). This

is shown in the last sub-figure titled with Stage 1($l = 2$). That procedure goes up to $l = 5$ in the same manner while STA1 updates the best sector in every stage.

Stage 1 is the most critical part of the algorithm. If all packets are lost in Stage 1, algorithm repeats Stage 1 as rotating each sector ID by 30 degrees. If still no FB is received by STA1, it rotates 15 degrees and repeats the stage.

Note that, to obtain the knowledge of the best receiving sector of STA2, we can send several packets from each sector of STA1 to be tested by all receiving sectors of STA2; i.e. exhaustive search in STA2. Also, note that we state performing an exhaustive search for all stages. This is, indeed, required since we cannot be sure of the accuracy of the selected best STA2 sector until it pairs with the best STA1 sector. That is, the selected best STA2 sector in Stage 1, for instance, might not be the overall best STA2 sector. That phenomenon results from the fact that we seek the best communication link between STAs, instead of seeking the best sector of either STA1 or STA2 merely.

9.4 Step Analysis

We calculate the number of steps required in sector training process for BSB and the proposed method (EBSB) and compare with current BF algorithms of 802.15.3c and 802.11ad standards. Table 9.1 shows the step analysis of each method for four different N . We use the 2-D domain ($N = N_1$) in order to stay on the same line with the literature.

Although, the number of steps seems to get higher according to BSB method, it is still acceptable compared with exhaustive search adopted by the standards where the extreme number of steps is required. On the other hand, since there is an expected trade-off between the number of steps and the success probability, EBSB has relatively improved reliability compared with BSB algorithm which we will show in the next section.

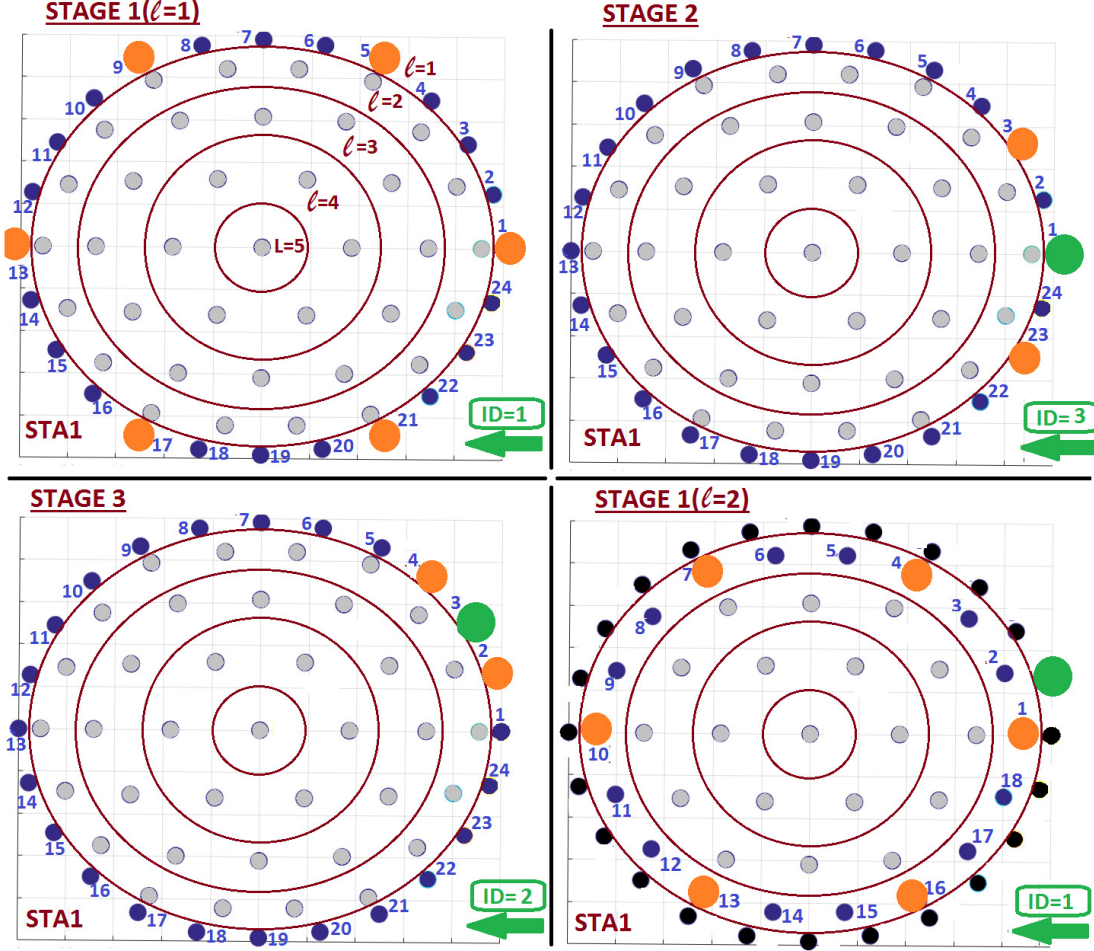


Figure 9.4: An example of EBSB algorithm for $N_1 = 24$

9.5 Simulation Results

In this part, we simulate the performances of proposed method using MATLAB. We follow IEEE 802.11ad specifications and compare the proposed method with the current exhaustive search BF and BSB algorithms. We use the conference room channel model described in [10] considering the communication link is 'station-to-station' (STA-STA). Success probability, BF setup time and power analysis results are compared. Parameters used in the simulations are given in Table 9.2.

9.5.1 Success Probability

Since the problem is to choose the best beam ID of the antenna, simulating the probability of successful detection of the correct beam will be a good idea to compare methods.

Table 9.1: Step Analyses of BF Algorithms

Methods/ N	8 Sectors	16 Sectors	32 Sectors	64 Sectors
802.11ad	18	34	66	130
BSB WLAN	18	24	30	36
EBSB WLAN	18	28	34	40
802.15.3c	140	532	2084	8260
BSB WPAN	37	144	278	540
EBSB WPAN	37	206	404	794

Table 9.2: Simulation Parameters

Parameter	Description
Channel Model	TGad Model Conference Room [10]
Subscenario	STA-STA
Number of Antennas	1 for each STA (SISO)
Distance	1-11 meters
Frequency	60 GHz
Cluster/Case	LOS and NLOS
Noise/Loss Model	Path Loss
Shadowing Effect	Disabled
Antenna Model	Basic Steerable Antenna [10]
Polarization Support	Disabled
Number of Experiments	100 (for each number of sector)

The best beam is believed to be the one that exhaustive search chooses. Fig. 9.5 and 9.6 demonstrate the success probability of two methods, BSB and EBSB, for LOS and NLOS cases, respectively. In order to see the threshold effect, we simulated the methods both with and without threshold setting. We set the value as 7 dB and 11 dB below the maximum gain for LOS and NLOS conditions, respectively. Also, to analyze the rotation effect in Stage 1, EBSB with 1 and 2 rotations are simulated in the same figure.

In Fig. 9.5, the effect of the threshold value is apparent. If we keep the probability value of 0.9 as a limit, for LOS environments, without applying a threshold, EBSB is efficient for N smaller than 75, clearly better than BSB in the same conditions which

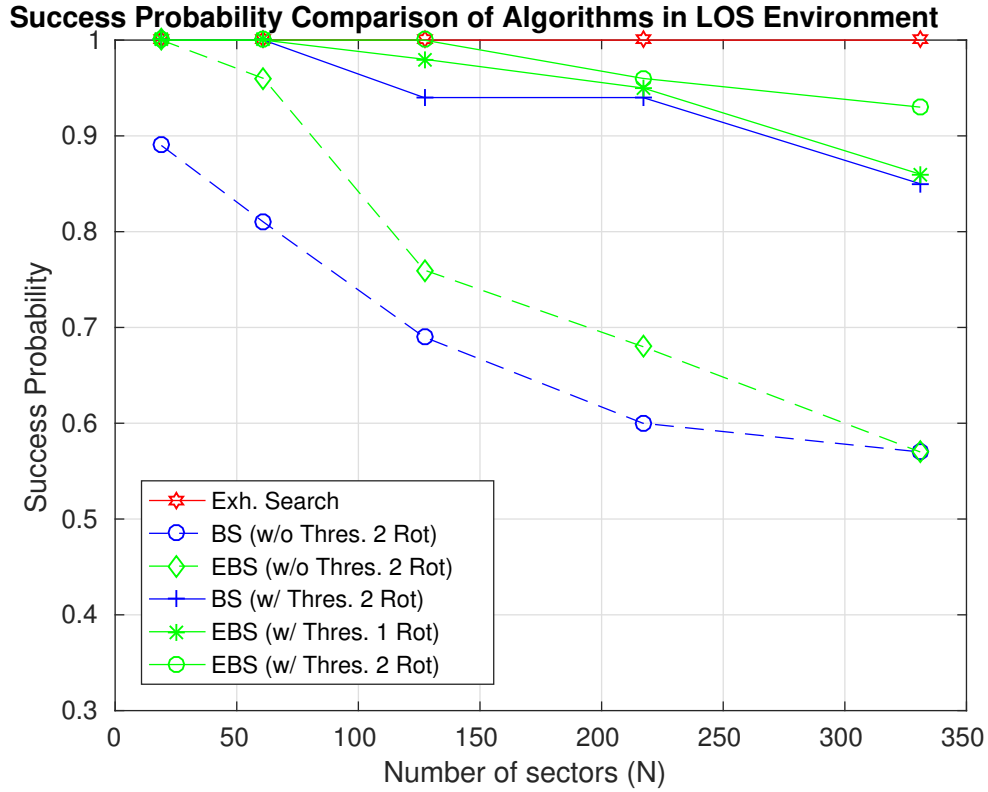


Figure 9.5: Success probability of the methods in LOS situations.

is effective for only small devices that have low number of antenna elements. However, once threshold is applied, for $N < 275$, both methods are appropriate for usage regardless of the additional precaution rotation in Stage 1. Even so, EBSB has slightly better accuracy performance than BSB.

As seen in Fig. 9.6, no matter a threshold is set or not, even for very small N , BSB is impractical in NLOS conditions. Increasing N severely deteriorates the accuracy performance of BSB. On the other hand, for a limit probability value of 0.85, EBSB without threshold is applicable for $N < 100$. This value goes up to 250 when a threshold value is applied. Although additional rotation doesn't provide remarkable improvements either in NLOS environments, it can be preferred for accuracy sensitive communications. The degradation reason in both figures as increasing number of sectors is the increasing sensitivity of the antenna.

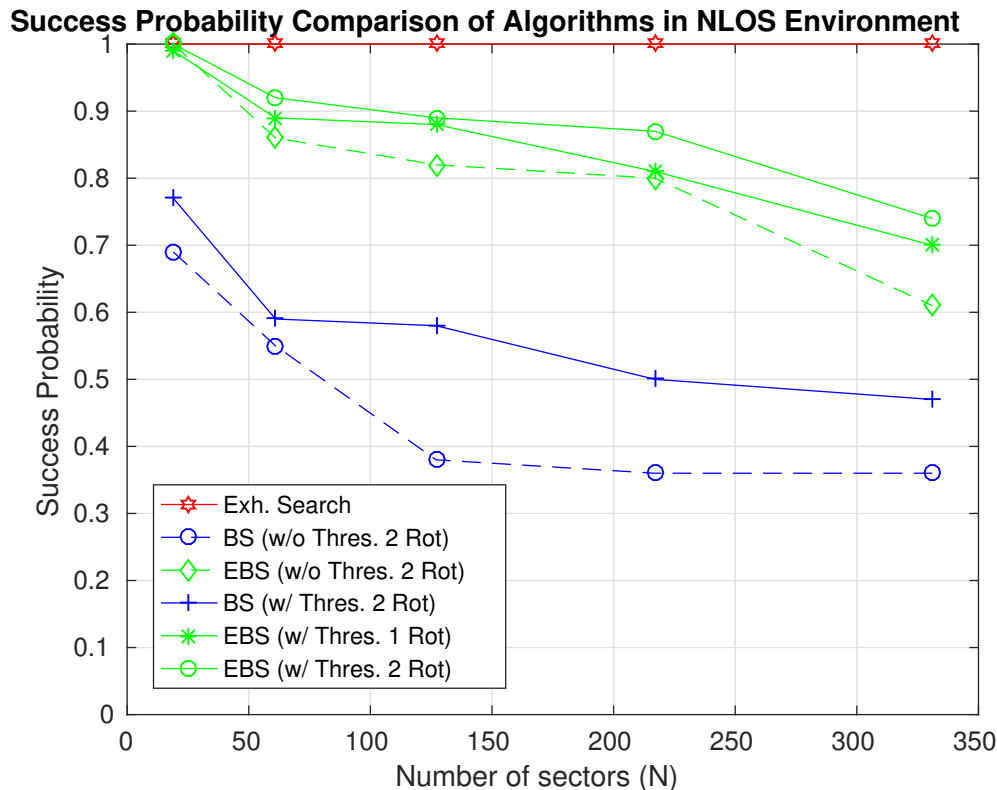


Figure 9.6: Success probability of the methods in NLOS situations.

9.5.2 Beamforming Setup Time

In Fig. 9.7, BF setup time performances of BF methods are presented. Here we didn't apply a threshold to the algorithms. And the setup time covers the training time of the link; i.e. both the transmitting beams of STA1 and the receiving beams of STA2. While exhaustive search BF setup time increases exponentially as the number of sectors increases, it is increasing almost linearly in BSB and EBSB algorithms. As expected, EBSB's training time is slightly worse than BSB's due to the scanning of the layers separately. However, it is still acceptable since the scanning time of over 330 sectors is just 34% of the exhaustive search BF time. On the other hand, additional rotation gives a subtle difference in terms of setup time.

Considering the trade-off between the accuracy and the time, EBSB is more reliable than BSB as it provides practical usage in NLOS conditions while spending little more time comparing with BSB.

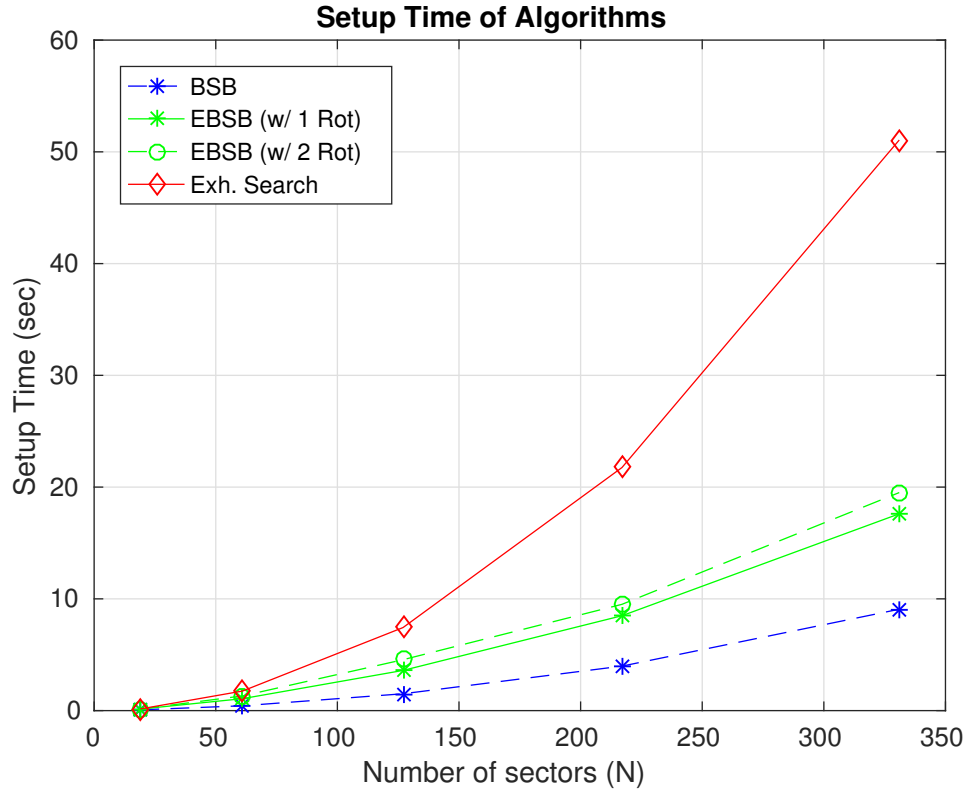


Figure 9.7: BF setup performance of methods.

It is also worthy to note that, although, Fig. 9.7 seems a direct consequence of Table 9.1, it compares the real-time cost of the proposed methods with exhaustive search approach while Table 9.1 calculates the number of exchanged packets for the proposed protocols and BF protocols adopted by standards, specifically.

9.5.3 Power Loss Analysis

Fig. 9.8 shows the received power loss of the algorithms due to the misalignment of the sectors during the setup. Average and maximum losses are denoted in the subplots. In LOS, maximum power loss for EBSB is around 4 dB while it reaches to 10 dB for BSB. In NLOS, EBSB has the maximum loss value of 5.5 dB as BSB losses 15 dB. Clearly, even if EBSB fails to select the best beam pair for any number of sectors, the maximum gain loss is only 5.5 dB which may be tolerable. The average power loss lines show that, for any number of sectors, (1) failure of the EBSB algorithm is very rare, (2) average loss is smaller than 1 dB, regardless of the environment conditions.

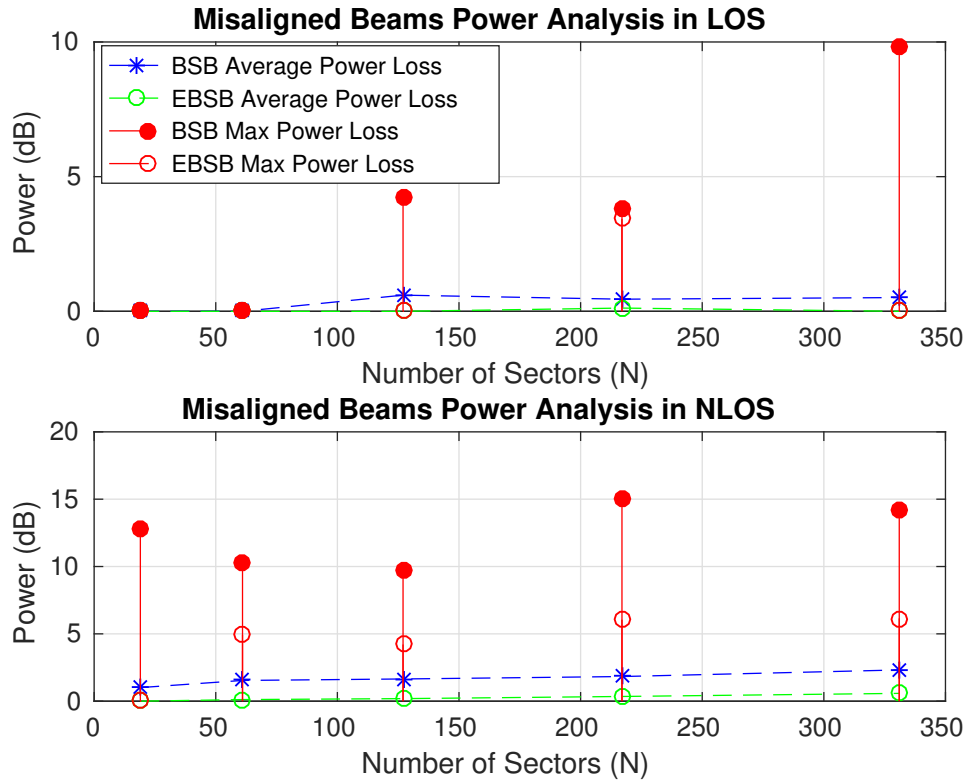


Figure 9.8: Power loss analysis due to the misalignment of the beams.

9.6 Conclusion

In this chapter, we proposed a searching algorithm, Enhanced Binary Searching Beamforming (EBSB), for beam training in 60GHz mm-wave communications. It is an improved version of Binary Searching Beamforming (BSB) algorithm for both LOS and NLOS cases and can be applied directly to the mm-wave WPAN and WLAN standards' beam training clauses. Simulation results show that, for smaller than 100 sectors in both devices' antennas, EBSB algorithm's accuracy rate is higher than 90% in NLOS conditions. It provides higher than 0.9 success probability for any number of sectors in LOS conditions. On the other hand, with EBSB, training time can be reduced to 34% of exhaustive search BF setup time for 330 sectors. Power loss analysis shows that in the cases of misalignment in EBSB, the average gain loss is below 1 dB.

Chapter 10

Conclusion

In this dissertation, we first create a ray-tracing based intra-cluster channel model (RT-ICM) for stationary mmWave communications (Part I) and then using RT-ICM, we inquire the optimum beamwidth values that maximizes the received power in the case of both perfect and imperfect alignments (Part II). Using the theoretical array antenna gain models for uniform linear array (ULA) and uniform planar array (UPA), we estimate the required number of antennas for the optimum beamwidth; thereby analyzing the cost at the receiver structure and study the trade-off curves for the reasonable optimum hardware complexity. We also discuss about the practical implementation of flexible beamwidth in a hybrid beamforming system. Finally, we propose two fast beam searching protocols that work at MAC layer to complete the beamforming efficiency analysis at mmWave communications (Part III). In the simulations sections of respective parts, we show that the proposed intra-cluster model, RT-ICM is in a perfect agreement with the measurements as well as a full-scan software results. For the beamwidth analysis, we demonstrate that the optimum beamwidth is a function of standard deviation of the channel power spectrum and the amount of misalignment. For a perfect alignment, we also show that the optimum beamwidth is zero, but to reach 95% of the maximum power for an indoor mmWave cluster, a practical beamwidth of $7^\circ - 10^\circ$ is enough, which can be created with 18 – 20 antenna elements for ULA. It is concluded that the antenna gain dominates the received power in the UPA case and intra-cluster power angular spectrum of the channel becomes less critical.

Appendix A

Derivations for RT-ICM

A.1 BGM Parameters

In this Appendix, we give the complete procedure of how the BGM parameters derived.

A.1.1 Derivation of ϕ_s and l_{dif}

From Fig. 2.2, $\phi_s = \cos^{-1}(h_r/d_1)$ where, $d_1 = (h_r l_s / (h_t + h_r))$. Plugging d_1 , we get ϕ_s .

From Fig. 2.2, $l_1 = h_r / \cos(\phi_s - \alpha)$ and $l_2 = \sqrt{h_t^2 + (s'_1)^2}$ where $s'_1 = s - s'_2$ and $s'_2 = l_1 \sin(\phi_s - \alpha)$. Plugging everything to Eq. (2.1), Eq. (2.2) is obtained.

A.1.2 Derivation of Support Region Limitations

Geometry Limitation

From Fig. 2.2, for $\alpha < 0$, the tilt angle doesn't increase the support region as any ray captured by the receiver with AoA of $\phi_s - \alpha \geq 90^\circ$ cannot be a reflection from that reflector. Hence, the lower bound for α is $\phi_s - 90^\circ$. On the other hand, upper bound is a little tricky. The line goes through the transmitter and receiver (LOS line) sets the new limit to the upper bound and the tilting reduces the upper bound by σ . Similarly, for the case $h_t < h_r$, σ limits α on the lower bound to be $\alpha > \phi_s - \sigma - 90^\circ$, while the upper bound remains unchanged.

Transmitter Beamwidth Limitation

In Fig. 2.5, from the right triangle similarity, the angle between the RNT and the departing specular ray is equal to ϕ_s . Hence, $s_t = h_t \tan(\phi_s - (\Theta/2))$. On the other hand, $s_1 = h_t \tan \phi_s$. Then $l_t = s_1 - s_t$. And for l_r , $s_1 + l_r = h_t \tan(\phi_s + (\Theta/2))$.

A.1.3 Formulation Validation of BGM

Path Length Calculation Check

For positive side reflection, $\phi_s - \alpha_p < 0$, but $\cos(\phi_s - \alpha_p) > 0$, hence $l_1 > 0$. However, since $\sin(\phi_s - \alpha_p) < 0$, $s'_{2,p} < 0$. Thus, $s'_{1,p}$ is larger than s but l_2 is accurately computed based on the geometry. As a result, resultant calculations of l_1 and l_2 are correct.

For negative side reflection, $\phi_s - \alpha_n > 0$, and l_1 is calculated as expected. However, since $s'_{2,n} > s$, $s'_{1,n}$ is negative. Note that, when calculating l_2 , $s'_{1,n}$ is squared. Hence, l_2 is resulted as expected too.

Reflector Length Calculation Check

For positive side reflection, since l_{pos} is larger than s_2 , s_{pos} turns out to be negative. That yields $\phi_s - \alpha^+ < 0$ which is, actually, correct as α^+ is larger than ϕ_s . For negative side reflection, nothing is unusual in the formulation.

Transmit Beamwidth Calculation Check

As seen from Fig. 2.5, $\phi_s - \Theta/2 < 0$ which yields $s_t < 0$. However, l_t is calculated correctly. For l_r , calculation is as expected.

A.2 Validation of the Directive Model for All Cases

We consider the cases, diffuse rays reflected from (1) the *receiver* side of the specular ray, (2) the back of the RNR, (3) the back of the RNT. For the case (1), the diffuse rays in Fig. 2.7 with θ_1 can be an example. In that case, α_k and ψ_k are positive. Eq. (2.9) holds as the variables don't change. Since we paid attention to the angle signs during the formulation setup, Eq. (2.10) holds too. For the case (2), the diffuse ray in Fig. 2.7 with θ_2 is an example. α_k and ψ_k are still positive. From Fig. 2.6, s'_1 is positive and grazing angle calculation in Eq. (2.9) is valid. Since $\alpha_k > \phi_s$, $(\phi_s - \alpha_k) < 0$. Hence, $\theta_k + \psi_k > 90$ which is the case as spread angle exceeds the reflector normal at reflection point. Hence, Eq. (2.10) is valid too. However, in the case of (3), for which the diffuse ray in Fig. 2.7 with θ_3 is an example, the specular reflection of the diffuse ray reflects towards the

opposite direction of the receiver. However, Eq. (2.10) computes ψ'_k as shown in Fig. 2.7 which is inaccurate. To correct it, additional $2(90 - \theta_k)$ should be added. That is, recalling that $\psi_k < 0$, $\psi_k = 90 - (\phi_s - \alpha_k) - \theta_k - 2(90 - \theta_k) = \theta_k - 90 - (\phi_s - \alpha_k)$.

Appendix B

Derivations for Beamwidth Analysis

B.1 Maximization of P_R in case of Misalignment

B.1.1 First Derivative

First derivative of Eq. (5.18) and equalize zero,

$$\frac{d\left(\frac{1}{\Delta\phi}\left(\operatorname{erf}\left(\frac{\Delta\phi+2\delta}{2\sqrt{2}\sigma}\right)+\operatorname{erf}\left(\frac{\Delta\phi-2\delta}{2\sqrt{2}\sigma}\right)\right)\right)}{d\Delta\phi}=\left(\frac{\operatorname{erf}\left(\frac{\Delta\phi+2\delta}{2\sqrt{2}\sigma}\right)}{\Delta\phi}\right)'+\left(\frac{\operatorname{erf}\left(\frac{\Delta\phi-2\delta}{2\sqrt{2}\sigma}\right)}{\Delta\phi}\right)'=0 \quad (\text{B.1})$$

where

$$\begin{aligned} \left(\frac{\operatorname{erf}\left(\frac{\Delta\phi+2\delta}{2\sqrt{2}\sigma}\right)}{\Delta\phi}\right)' &= \frac{\frac{e^{-(\Delta\phi+2\delta)^2/(8\sigma^2)}}{\sqrt{2\pi}\sigma}\Delta\phi - \operatorname{erf}\left(\frac{\Delta\phi+2\delta}{2\sqrt{2}\sigma}\right)}{(\Delta\phi)^2} \\ \left(\frac{\operatorname{erf}\left(\frac{\Delta\phi-2\delta}{2\sqrt{2}\sigma}\right)}{\Delta\phi}\right)' &= \frac{\frac{e^{-(\Delta\phi-2\delta)^2/(8\sigma^2)}}{\sqrt{2\pi}\sigma}\Delta\phi - \operatorname{erf}\left(\frac{\Delta\phi-2\delta}{2\sqrt{2}\sigma}\right)}{(\Delta\phi)^2} \end{aligned}$$

Summing up, Eq. (5.19) is obtained.

$$\frac{d^2\left(\frac{1}{\Delta\phi}\left(\operatorname{erf}\left(\frac{\Delta\phi+2\delta}{2\sqrt{2}\sigma}\right)+\operatorname{erf}\left(\frac{\Delta\phi-2\delta}{2\sqrt{2}\sigma}\right)\right)\right)}{d^2\Delta\phi}=\left(\frac{e^{-\frac{(\Delta\phi+2\delta)^2}{8\sigma^2}}}{8\sigma^2}+\frac{e^{-\frac{(\Delta\phi-2\delta)^2}{8\sigma^2}}}{8\sigma^2}\right)'\frac{1}{\sqrt{2\pi}\sigma\Delta\phi}-\left(\frac{\operatorname{erf}\left(\frac{\Delta\phi+2\delta}{2\sqrt{2}\sigma}\right)+\operatorname{erf}\left(\frac{\Delta\phi-2\delta}{2\sqrt{2}\sigma}\right)}{(\Delta\phi)^2}\right)'<0 \quad (\text{B.2})$$

$$\left(\frac{e^{-\frac{(\Delta\phi+2\delta)^2}{8\sigma^2}}}{8\sigma^2}+\frac{e^{-\frac{(\Delta\phi-2\delta)^2}{8\sigma^2}}}{8\sigma^2}\right)'=\frac{-\Delta\phi(\Delta\phi(\Delta\phi+2\delta)+4\sigma^2)e^{-\frac{(\Delta\phi+2\delta)^2}{8\sigma^2}}}{4\sigma^3\sqrt{2}(\Delta\phi)^2}-\frac{\Delta\phi(\Delta\phi(\Delta\phi-2\delta)+4\sigma^2)e^{-\frac{(\Delta\phi-2\delta)^2}{8\sigma^2}}}{4\sigma^3\sqrt{2}(\Delta\phi)^2} \quad (\text{B.3})$$

$$\left(\frac{\operatorname{erf}\left(\frac{\Delta\phi+2\delta}{2\sqrt{2}\sigma}\right)+\operatorname{erf}\left(\frac{\Delta\phi-2\delta}{2\sqrt{2}\sigma}\right)}{(\Delta\phi)^2}\right)'=\frac{\Delta\phi\left(e^{-\frac{(\Delta\phi+2\delta)^2}{8\sigma^2}}+e^{-\frac{(\Delta\phi-2\delta)^2}{8\sigma^2}}\right)-2\sqrt{2}\pi\sigma\left(\operatorname{erf}\left(\frac{\Delta\phi+2\delta}{2\sqrt{2}\sigma}\right)+\operatorname{erf}\left(\frac{\Delta\phi-2\delta}{2\sqrt{2}\sigma}\right)\right)}{\sigma\sqrt{2}\pi(\Delta\phi)^3} \quad (\text{B.4})$$

B.1.2 Second Derivative

Second derivative of Eq. (5.18) with setting smaller than zero is given in Eq. (B.2)

through (B.4). After subtraction and modification such that the denominator is $4\sigma^3\sqrt{2}\pi(\Delta\phi)^3$,

the denominator can be eliminated as it is positive and equation results in Eq. (5.20).

B.2 Maximization of P_R for Perfect Alignment

B.2.1 Maximum Received Power Derivation

Derivatives of the nominator and denominator of Eq. (5.24) are,

$$\frac{d\left(\operatorname{erf}\left(\frac{\Delta\phi}{2\sqrt{2}\sigma}\right)\right)}{d\Delta\phi} = \frac{e^{-\Delta\phi^2/8\sigma^2}}{\sigma\sqrt{2\pi}}$$

$$\frac{d\left(\frac{\Delta\phi \sin \phi_0}{101.5P_{tot}}\right)}{d\Delta\phi} = \frac{\sin \phi_0}{101.5P_{tot}}$$

Then, the maximum received power is

$$P_{max}^t = \lim_{\Delta\phi \rightarrow 0} P_R(\Delta\phi) = \frac{101.5P_{tot}}{\sin \phi_0} \frac{e^{-\Delta\phi^2/8\sigma^2}}{\sigma\sqrt{2\pi}} \Big|_{\Delta\phi=0}$$

$$= \frac{40.5P_{tot}}{\sigma \sin \phi_0}$$

B.2.2 Optimum Beamwidth Approximation

Using the first and second term of the error function Taylor expansion, Eq. (5.28) becomes

$$\frac{\Delta\phi_\eta}{\left(\frac{\Delta\phi_\eta}{2\sqrt{2}\sigma} - \frac{(\Delta\phi_\eta/2\sqrt{2}\sigma)^3}{3}\right)} = \frac{5\sigma}{\eta\sqrt{\pi}}$$

Further manipulation gives

$$(\Delta\phi_\eta)^3 - (24\sigma^2)\Delta\phi_\eta + \eta(24.06\sigma^2)\Delta\phi_\eta = 0$$

Ignoring the hundredths decimal and solving the equation for $\Delta\phi_\eta > 0$, Eq. (5.29) results.

References

- [1] Rangan, Sundeep, Theodore S. Rappaport, and Elza Erkip. "Millimeter-wave cellular wireless networks: Potentials and challenges." *Proceedings of the IEEE* 102.3 (2014): 366-385.
- [2] Yaman, Yavuz, and Predrag Spasojevic. "Reducing the LOS ray beamforming setup time for IEEE 802.11ad and IEEE 802.15.3c." *Military Communications Conference, MILCOM 2016-2016 IEEE*. IEEE, 2016.
- [3] Yaman, Yavuz, and Predrag Spasojevic. "Enhanced binary search time-efficient mmWave beamforming algorithm for NLOS environments." *2017 IEEE Wireless Communications and Networking Conference (WCNC)*. IEEE, 2017.
- [4] El Ayach, Omar, et al. "Spatially sparse precoding in millimeter wave MIMO systems." *IEEE transactions on wireless communications*, 13.3 (2014): 1499-1513.
- [5] Ertel, Richard Brian, et al. "Overview of spatial channel models for antenna array communication systems." *IEEE personal communications* 5.1 (1998): 10-22.
- [6] "Technical Specification Group Radio Access Network; Study on Channel Model for Frequencies from 0.5 to 100 GHz (Rel. 14)", *3GPP TR 38.901 V14.1.1 (201707)*, July 2017.
- [7] Maltsev, A. "D5. 1-Channel Modeling and Characterization." *MiWEBA Project (FP7-ICT-608637), Public Deliverable* (2014).
- [8] Liu, Lingfeng, et al. "The COST 2100 MIMO channel model." *IEEE Wireless Communications* 19.6 (2012): 92-99.
- [9] Gustafson, Carl. *60 GHz Wireless Propagation Channels: Characterization, Modeling and Evaluation*. Vol. 69. 2014.
- [10] Maltsev A., et al, Channel models for 60 GHz WLAN systems, *IEEE Document* 802.11-09/0334r6, January 2010.
- [11] <https://mentor.ieee.org/802.11/dcn/15/11-15-1150-09-00ay-channel-models-for-ieee-802-11ay.docx>
- [12] S-K. Yong, et al., TG3c channel modeling sub-committee final report, *IEEE Techn. Rep.*, 15-07-0584-01-003c, Mar. 2007.
- [13] Saleh, Adel AM, and Reinaldo Valenzuela. "A statistical model for indoor multipath propagation." *IEEE Journal on selected areas in communications* 5.2 (1987): 128-137.
- [14] Spencer, Quentin H., et al. "Modeling the statistical time and angle of arrival characteristics of an indoor multipath channel." *IEEE Journal on Selected areas in communications* 18.3 (2000): 347-360.
- [15] Steinbauer, Martin, Andreas F. Molisch, and Ernst Bonek. "The double-directional radio channel." *IEEE Antennas and propagation Magazine* 43.4 (2001): 51-63.
- [16] Xu, Hao, Vikas Kukshya, and Theodore S. Rappaport. "Spatial and temporal characteristics of 60-GHz indoor channels." *IEEE Journal on selected areas in communications* 20.3 (2002): 620-630.
- [17] Akdeniz, Mustafa Riza, et al. "Millimeter wave channel modeling and cellular capacity evaluation." *IEEE journal on selected areas in communications* 32.6 (2014): 1164-1179.

- [18] Maltsev, Alexander, et al. "Experimental investigations of 60 GHz WLAN systems in office environment." *IEEE Journal on Selected Areas in Communications* 27.8 (2009).
- [19] Smulders, Peter FM. "Statistical characterization of 60-GHz indoor radio channels." *IEEE Transactions on Antennas and Propagation* 57.10 (2009): 2820-2829.
- [20] Kyro, Mikko, et al. "Statistical channel models for 60 GHz radio propagation in hospital environments." *IEEE Transactions on Antennas and Propagation* 60.3 (2012): 1569-1577.
- [21] Samimi, Mathew K., and Theodore S. Rappaport. "3-D millimeter-wave statistical channel model for 5G wireless system design." *IEEE Transactions on Microwave Theory and Techniques* 64.7 (2016): 2207-2225.
- [22] Gustafson, Carl, et al. "On mm-wave multipath clustering and channel modeling." *IEEE Transactions on Antennas and Propagation* 62.3 (2014): 1445-1455.
- [23] Weiler, Richard J., et al. "Quasi-deterministic millimeter-wave channel models in MiWEBA." *EURASIP Journal on Wireless Communications and Networking* 2016.1 (2016): 84.
- [24] Gentile, Camillo, et al. "Quasi-Deterministic Channel Model Parameters for a Data Center at 60 GHz." *IEEE Antennas and Wireless Propagation Letters* 17.5 (2018): 808-812.
- [25] Rappaport, Theodore S. *Wireless communications: principles and practice*. Vol. 2. New Jersey: prentice hall PTR, 1996.
- [26] Rappaport, Theodore S., et al. *Millimeter wave wireless communications*. Pearson Education, 2015.
- [27] Orfanidis, Sophocles J. "Electromagnetic waves and antennas." (2002).
- [28] Balanis, Constantine A. *Antenna theory: analysis and design*. John wiley & sons, 2016.
- [29] Hansen, Robert C. *Phased array antennas*. Vol. 213. John Wiley & Sons, 2009.
- [30] Glassner, Andrew S., ed. *An introduction to ray tracing*. Elsevier, 1989.
- [31] Durgin, Greg, Neal Patwari, and Theodore S. Rappaport. "An advanced 3D ray launching method for wireless propagation prediction." *Vehicular Technology Conference, 1997, IEEE 47th*. Vol. 2. IEEE, 1997.
- [32] Schaubach, Kurt R., N. J. Davis, and Theodore S. Rappaport. "A ray tracing method for predicting path loss and delay spread in microcellular environments." *Vehicular Technology Conference, 1992, IEEE 42nd*. IEEE, 1992.
- [33] Maltsev, Alexander, et al. "Statistical channel model for 60 GHz WLAN systems in conference room environment." *Antennas and Propagation (EuCAP), 2010 Proceedings of the Fourth European Conference on*. IEEE, 2010.
- [34] Murdock, James N., et al. "A 38 GHz cellular outage study for an urban outdoor campus environment." *Wireless Communications and Networking Conference (WCNC), 2012 IEEE*. IEEE, 2012.
- [35] Rappaport, Theodore S., et al. "Cellular broadband millimeter wave propagation and angle of arrival for adaptive beam steering systems." *Radio and Wireless Symposium (RWS), 2012 IEEE*. IEEE, 2012.
- [36] Thomas, Timothy A., et al. "3D mmWave channel model proposal." *Vehicular Technology Conference (VTC Fall), 2014 IEEE 80th*. IEEE, 2014.
- [37] Maltsev, Alexander, et al. "Quasi-deterministic approach to mmwave channel modeling in a non-stationary environment." *Globecom Workshops (GC Wkshps), 2014*. IEEE, 2014.
- [38] Rajagopal, Sridhar, Shadi Abu-Surra, and Mehrzad Malmirchegini. "Channel feasibility for outdoor non-line-of-sight mmwave mobile communication." *Vehicular Technology Conference (VTC Fall), 2012 IEEE*. IEEE, 2012.

- [39] ITU Report 1008-1. "Reflection from the Surface of the Earth". 1986-1990.
- [40] ITU-R P.2040-1. "Effects of building materials and structures on radiowave propagation above about 100 MHz". (07/2015).
- [41] Degli-Esposti, Vittorio, et al. "Measurement and modelling of scattering from buildings." *IEEE Transactions on Antennas and Propagation* 55.1 (2007): 143-153.
- [42] Pascual-Garca, Juan, et al. "On the importance of diffuse scattering model parameterization in indoor wireless channels at mm-wave frequencies." *IEEE Access* 4 (2016): 688-701.
- [43] Jacob, Martin, et al. "A ray tracing based stochastic human blockage model for the IEEE 802.11 ad 60 GHz channel model." *Proceedings of the 5th European Conference on Antennas and Propagation (EUCAP)*. IEEE, 2011.
- [44] Jacob, Martin, et al. "Extension and validation of the IEEE 802.11 ad 60 GHz human blockage model." *2013 7th European Conference on Antennas and Propagation (EuCAP)*. IEEE, 2013.
- [45] Jacob, Martin, et al. "Fundamental analyses of 60 GHz human blockage." *2013 7th European Conference on Antennas and Propagation (EuCAP)*. IEEE, 2013.
- [46] Collonge, Sylvain, Gheorghe Zaharia, and Ghais El Zein. "Influence of the human activity on wide-band characteristics of the 60 GHz indoor radio channel." *IEEE Trans. on Wireless Commun.*, vol. 3, no. 6, pp. 2396-2406, Nov 2004.
- [47] Gustafson, Carl, and Fredrik Tufvesson. "Characterization of 60 GHz shadowing by human bodies and simple phantoms." *2012 6th European Conference on Antennas and Propagation (EUCAP)*. IEEE, 2012.
- [48] Zhao, Hang, et al. "28 GHz millimeter wave cellular communication measurements for reflection and penetration loss in and around buildings in New York city." *2013 IEEE International Conference on Communications (ICC)*. IEEE, 2013.
- [49] Mhaske, Swapnil, Predrag Spasojevic, and Ahsan Aziz. "A Blockage Model for the Open Area Mm-wave Device-to-Device Environment." arXiv preprint arXiv:1909.12992 (2019).
- [50] Haenggi, Martin. Stochastic geometry for wireless networks. Cambridge University Press, 2012.
- [51] P. A. W. Lewis and G. S. Shedler, Simulation of Non- homogenous Poisson Point Processes by Thinning, *Naval Postgraduate School Rep.*, Jun 1978.
- [52] Williamson, M. R., G. E. Athanasiadou, and A. R. Nix. "Investigating the effects of antenna directivity on wireless indoor communication at 60 GHz." *Proceedings of 8th International Symposium on Personal, Indoor and Mobile Radio Communications-PIMRC'97. Vol. 2*. IEEE, 1997.
- [53] Manabe, Takeshi, Yuko Miura, and Toshio Ihara. "Effects of antenna directivity and polarization on indoor multipath propagation characteristics at 60 GHz." *IEEE Journal on selected Areas in Communications* 14.3 (1996): 441-448.
- [54] Kim, Myung-Don, et al. "Investigating the effect of antenna beamwidth on millimeter-wave channel characterization." *2016 URSI Asia-Pacific Radio Science Conference (URSI AP-RASC)*. IEEE, 2016.
- [55] Yang, Haibing, et al. "Impact analysis of directional antennas and multiantenna beamformers on radio transmission." *IEEE Transactions on Vehicular Technology* 57.3 (2008): 1695-1707.
- [56] Vakilian, Vida, Jean-Francois Frigon, and Sebastien Roy. "Effects of angle-of-arrival estimation errors, angular spread and antenna beamwidth on the performance of reconfigurable SISO systems." *Proceedings of 2011 IEEE Pacific Rim Conference on Communications, Computers and Signal Processing*. IEEE, 2011.

- [57] Akoum, Salam, Omar El Ayach, and Robert W. Heath. "Coverage and capacity in mmWave cellular systems." *2012 conference record of the forty sixth Asilomar conference on signals, systems and computers (ASILOMAR)*. IEEE, 2012.
- [58] Va, Vutha, and Robert W. Heath. "Basic relationship between channel coherence time and beamwidth in vehicular channels." *2015 IEEE 82nd Vehicular Technology Conference (VTC2015-Fall)*. IEEE, 2015.
- [59] Lee, Juyul, et al. "FieldMeasurementBased Received Power Analysis for Directional Beamforming MillimeterWave Systems: Effects of Beamwidth and Beam Misalignment." *ETRI Journal* 40.1 (2018): 26-38.
- [60] Dogan, Seda, Murat Karabacak, and Huseyin Arslan. "Optimization of Antenna Beamwidth under Blockage Impact in Millimeter-Wave Bands." *2018 IEEE 29th Annual International Symposium on Personal, Indoor and Mobile Radio Communications (PIMRC)*. IEEE, 2018.
- [61] Guo, Hongwei. "A simple algorithm for fitting a Gaussian function [DSP tips and tricks]." *IEEE Signal Processing Magazine* 28.5 (2011): 134-137.
- [62] Papoulis, Athanasios, and S. Unnikrishna Pillai. *Probability, random variables, and stochastic processes*. Tata McGraw-Hill Education, 2002.
- [63] O. E. Ayach, R. W. Heath, S. Abu-Surra, S. Rajagopal and Z. Pi, "Low complexity precoding for large millimeter wave MIMO systems," *2012 IEEE International Conference on Communications (ICC)*, Ottawa, ON, 2012, pp. 3724-3729.
- [64] A. Alkhateeb, O. El Ayach, G. Leus and R. W. Heath, "Channel Estimation and Hybrid Precoding for Millimeter Wave Cellular Systems," in *IEEE Journal of Selected Topics in Signal Processing*, vol. 8, no. 5, pp. 831-846, Oct. 2014.
- [65] S. Hur, T. Kim, D. J. Love, J. V. Krogmeier, T. A. Thomas and A. Ghosh, "Millimeter Wave Beamforming for Wireless Backhaul and Access in Small Cell Networks," in *IEEE Transactions on Communications*, vol. 61, no. 10, pp. 4391-4403, October 2013.
- [66] Raghavan, Vasanthan, et al. "Beamforming tradeoffs for initial UE discovery in millimeter-wave MIMO systems." *IEEE Journal of Selected Topics in Signal Processing*, 10.3 (2016): 543-559.
- [67] C. Kerce, G. Brown, M. Mitchell, "Phase-Only Transmit Beam Broadening for Improved Radar Search Performance," *IEEE Radar Conference*, pg.451-456, Apr. 2007.
- [68] H. Lebrete, S. Boyd, "Antenna array pattern synthesis via convex optimization," *IEEE Transactions on Signal Processing*, vol.45, no.3, pg.526-532, Mar. 1997.
- [69] S. Rajagopal, "Beam broadening for phased antenna arrays using multi-beam subarrays," *IEEE International Conference on Communications (ICC)*, Ottawa, ON, 2012, pp. 3637-3642.
- [70] K. Venugopal, A. Alkhateeb, N. Gonzalez Prelcic and R. W. Heath, "Channel Estimation for Hybrid Architecture-Based Wideband Millimeter Wave Systems," in *IEEE Journal on Selected Areas in Communications*, vol. 35, no. 9, pp. 1996-2009, Sept. 2017.
- [71] "IEEE standard for Information Technology-Telecommunications and information exchange between systems-local and metropolitan area networks-specific requirements-part 11: Wireless LAN Medium Access Control (MAC) and Physical Layer (PHY) Specifications Amendment 3: Enhancements for very high throughput in the 60 GHz band," *IEEE Std 802.11ad-2012*, pp.1-628, Dec 2012.
- [72] "IEEE standard for Information Technology-local and metropolitan area networks-specific requirements-part 15.3: Amendment 2: Millimeterwave-based alternative physical layer extension," *IEEE Std 802.15.3c-2009 (Amendment to IEEE Std 802.15.3-2003)*, pp. 1-200, Oct 2009.
- [73] T. Nitsche, C. Cordeiro, A. B. Flores, E. W. Knightly, E. Perahia, and J. C. Widmer, "IEEE 802.11 ad: Directional 60 GHz communication for multigigabit-per-second Wi-Fi [Invited Paper]," *Communications Magazine*, IEEE, vol. 52, no. 12, pp. 132-141, 2014.

- [74] J. Wang, "Beam codebook based beamforming protocol for multi-Gbps millimeter-wave WPAN systems," *IEEE Journal on Selected Areas in Communications*, vol. 27, no. 8, pp. 1390-1399, October 2009.
- [75] J. Wang, Z. Lan, C.-S. Sum, C.-W. Pyo, J. Gao, T. Baykas, A. Rahman, R. Funada, F. Kojima, I. Lakkis et al., "Beamforming codebook design and performance evaluation for 60GHz wideband WPANs," in *Vehicular Technology Conference Fall (VTC 2009-Fall), 2009 IEEE 70th.* IEEE, 2009, pp. 1-6.
- [76] Chu, HongYun, et al. "Relay selection with feedback beamforming information through designed sector sweep report frame for mm-wave WPANs." *Science China Information Sciences* 57.8 (2014): 1-14.
- [77] Akhtar, Anique, and Sinem Coleri Ergen. "Efficient network level beamforming training for IEEE 802.11 ad WLANs." *Performance Evaluation of Computer and Telecommunication Systems (SPECTS), 2015 International Symposium on.* IEEE, 2015.
- [78] Li, Bin, et al. "Efficient beamforming training for 60-GHz millimeter-wave communications: A novel numerical optimization framework." *IEEE Transactions on Vehicular Technology* 63.2 (2014): 703-717.
- [79] Yuan, Wenfang, Simon MD Armour, and Angela Doufexi. "An efficient and low-complexity beam training technique for mmwave communication." *Personal, Indoor, and Mobile Radio Communications (PIMRC), 2015 IEEE 26th Annual International Symposium on.* IEEE, 2015.